Summer 2016

Modeling of lightning-induced thermal ablation damage in anisotropic composite materials and its application to wind turbine blades

Yeqing Wang
University of Iowa

MODELING OF LIGHTNING-INDUCED THERMAL ABLATION DAMAGE IN ANISOTROPIC COMPOSITE MATERIALS AND ITS APPLICATION TO WIND TURBINE BLADES

by

Yeqing Wang

A thesis submitted in partial fulfillment
of the requirements for the Doctor of
Philosophy degree in Mechanical Engineering
in the Graduate College of
The University of Iowa

August 2016

Thesis Supervisor: Professor Olesya I. Zhupanska

Graduate College
The University of Iowa
Iowa City, Iowa

CERTIFICATE OF APPROVAL

_____

PH.D. THESIS

_____

This is to certify that the Ph.D. thesis of

Yeqing Wang

has been approved by the Examining Committee
for the thesis requirement for the Doctor of Philosophy
degree in Mechanical Engineering at the August 2016 graduation.

Thesis Committee: _____
Olesya I. Zhupanska, Thesis Supervisor

_____
Hongtao Ding

_____
M. Asghar Bhatti

_____
Shaoping Xiao

_____
Kyung K. Choi

To My Parents

王巧生
倪彩芳

ACKNOWLEDGMENTS

I would like to thank Professor Olesya Zhupanska for her support and guidance through this research and my education in the Ph.D. program. The knowledge and skills I have developed will continue to benefit me throughout my future career. I also thank Professor Asghar Bhatti, Hongtao Ding, Shaoping Xiao, and Kyung K. Choi for serving on my thesis committee. In addition, I would like to thank Dr. Crystal Pasiliao (Munitions Directorate, Air Force Research Laboratory) for her support and invaluable advice on this research. Lastly, I would like to thank my family for their support during my education at The University of Iowa.

ABSTRACT

A primary motivation for this research comes from the need to improve the ability of polymer-matrix composites to withstand lightning strikes. In particular, we are concerned with lightning strike damage in composite wind turbine blades. The direct effects of lightning strike on polymer-matrix composites often include rapid temperature rise, melting or burning at the lightning attachment points, and mechanical damage due to lightning-induced magnetic force and acoustic shock wave. The lightning strike damage accumulation problem is essentially multiphysic. The lightning plasma channel discharges an electric current up to 200 kA, inducing a severe heat flux at the surface of the composite structure, as well as generating Joule heating through the composite structure. The resulting electro-thermo-mechanical response of the composite structure may include matrix degradation and decomposition, delamination, and fiber breakage and sublimation, thus leading to catastrophic failure.

The existing studies related to the lightning strike damage in composites ignored the lightning channel radius expansion during the initial lightning discharge and lacked adequate treatment of material phase transitions. These assumptions significantly simplify the mathematical treatment of the problem and affect the predictive capabilities of the models. Another common feature of these limited studies is that they all focused on carbon-fiber-reinforced polymer-matrix (CFRP) composites, which are electrically conductive.

In the present thesis, the thermal responses and thermal ablations in both non-conductive glass-fiber-reinforced polymer-matrix (GFRP) composite wind turbine blade and conductive CFRP composite wind turbine blade are studied. In the case of non-conductive GFRP composite wind turbine blade, prior to the thermal response and thermal ablation analysis, a finite element analysis is performed to calculate the electric field due to lightning stepped leader to estimate the dielectric breakdown of the non-

conductive composite wind turbine blade. The estimation of dielectric breakdown is used to determine whether Joule heating needs to be included in the problem formulation. To predict the thermal response and thermal ablation in the composite structure due to lightning strike, a physics-based model describing surface interaction between the lightning channel and the composite structure has been developed. The model consists of: (i) spatial and temporal evolution of the lightning channel as a function of the electric current waveform; (ii) temporary and spatially non-uniform heat flux and current density (in the case of electrically conductive CFRP composite or if dielectric breakdown occurs in the case of non-conductive GFRP composite) generated at the composite structure; and (iii) nonlinear transient heat transfer problem formulation for layered anisotropic composites that includes the moving boundary of the expanding lightning channel and the phase transition moving boundary associated with instantaneous material removal due to sublimation. The model has been employed to investigate the thermal responses and thermal ablations in a GFRP composite laminated panel used in a Sandia 100-meter all-glass baseline wind turbine blade (SNL 100-00) and a typical CFRP composite laminated panel subjected to lightning strike. The temperature-dependent directional material properties for both the GFRP and CFRP composites have been determined in this thesis using a micromechanics approach based on the experimental data for fibers and resin. An integrated Matlab-ABAQUS numerical procedure features the aforementioned aspects (i), (ii), and (iii) of the developed model. The obtained results include the evolution of temperature fields in the composite laminated panel and the progressive shape change of the composite laminated panel due to thermal ablation. The predictions of thermal ablation in the CFRP composite laminated panel are validated by reported experimental results.

PUBLIC ABSTRACT

Lightning strike causes significant damage in fiber-reinforced polymer-matrix (PMC) composite structures such as wind turbine blades. Complicated lightning-strike-induced thermal and mechanical loads result in thermal ablation, delamination, and fiber rupture in composite laminates. The extensive use of PMC composite materials in the wind energy industry presents significant challenges in the development of lightning strike protection systems for composite wind turbine blades, and a better understanding of the response of PMC composites to lightning strike is essential for such developments.

In this work, a numerical model is developed with finite element analysis (FEA) to predict the lightning-strike-induced electric fields along wind turbine blades. The model is applied to the non-conductive Sandia 100-meter All-glass Baseline Wind Turbine Blade and the predicted electric fields are compared to the dielectric breakdown strength of the blades to assess the possibility of the breakdown and associated damage. In addition, a physics-based model describing the thermal interaction between a lightning channel and a composite structure is developed. The model features the lightning channel radius expansion, the non-uniform spatial distributions of current density and heat flux within the lightning channel, and the temperature-dependent material properties of the composite materials. A corresponding computational procedure is developed and implemented to predict the lightning-strike-induced thermal ablation damage in a laminated glass-fiber-reinforced polymer-matrix (GFRP) and carbon-fiber-reinforced polymer-matrix (CFRP) composite wind blade. The predicted thermal ablation damage in the CFRP composite wind blade is validated by comparisons with existing experimental results.

TABLE OF CONTENTS

LIST OF TABLES

LIST OF FIGURES

CHAPTER 1
INTRODUCTION

1.1 Background Information

Composite materials are designed to achieve desirable mechanical and functional responses via a combination of at least two constituent phases. In general, matrix phase (e.g. epoxy, polyester, etc.) and reinforcement phase (e.g. carbon fibers, aramid fibers, carbon nanotube, etc.). The matrix phase serves as a basis for the composites by surrounding and supporting the reinforcement to maintain the relative positions of the reinforcement and meanwhile transfer loads. The reinforcement phase enhances the matrix properties by imparting their special physical or chemical properties. By adjusting the volume fractions of matrix phase or reinforcement phase, desired properties can be customized include stiffness, thermal behavior, electrical behavior, and strength to weight ratios among many others. Composite materials are not merely designed for structural support, they can also be multifunctional, such as energy storage, actuation, damage self-sensing, etc.

Due to the superior properties, composite materials are showing promise applications in aerospace structures, wind turbine structures, etc.

The composite materials used on wind turbine blades are typically glass-fiber-reinforced polymer-matrix (GFRP) composite prepregs. The advantages that make GFRP composites so widely used for wind turbine blades include their superior strength-to-weight ratio, cost effectiveness, design flexibility, durability, corrosion resistance, and electrical non-conductivity. Another type of composite material that has intrigued the interest of wind turbine blade manufacturer is the carbon-fiber-reinforced polymer-matrix (CFRP) composite. It is known to be much lighter and stronger than GFRP composite.

However, in most cases CFRP composite is much more expensive than GFRP composite which prevents it from being widely adopted in the wind energy industry.

Figure 1. 1: Glass-fiber-reinforced polymer-matrix composite prepreg layup in wind turbine blade mold.

Source: Berry, D., & Ashwill, T. (2007). Sandia National Laboratories, SAND2007-6065.

1.2 Motivation

A primary motivation for this study comes from the need to improve the ability of polymer-matrix composites to withstand lightning strikes. In particular, we are concerned with lightning strike damage in composite wind turbine blades. It is reported that blade damage accounts for the greatest number of losses for wind turbines, while lightning strikes are among the top two most frequently reported causes of loss in wind energy insurance claims in the United States (See Figure 1. 2). Figure 1. 3 shows that the Midwest and Texas, where the most wind power is produced (Figure 1. 4), are subjected

to high lightning flash activity. Also, since larger rated wind turbines are pursued in the recent years, the corresponding wind turbine blades are becoming longer. However, the longer the blade, the greater its risk of being hit by lightning (see Figure 1. 5). An increase in the blade size and extensive use of composite materials represent significant challenges in the development of lightning strike protection systems for wind turbine blades, and a better understanding of the response of polymer-matrix composites to a lightning strike is essential for such developments.

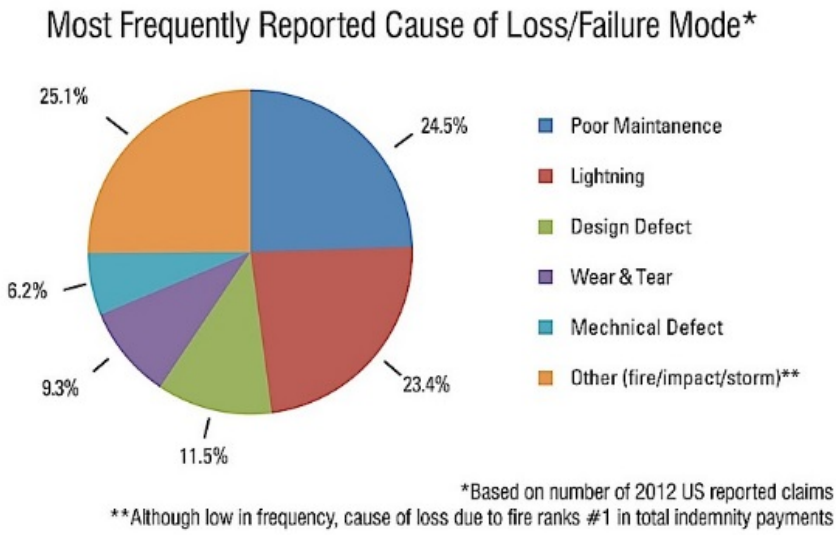

Figure 1. 2: Most frequently reported component damage for wind turbines.

Source: GCube Top 5 U.S. wind energy insurance claims report. Retrieved from: http://www.gcube-insurance.com/en/press/gcube-top-5-us-wind-energy-insurance-claims-report/.

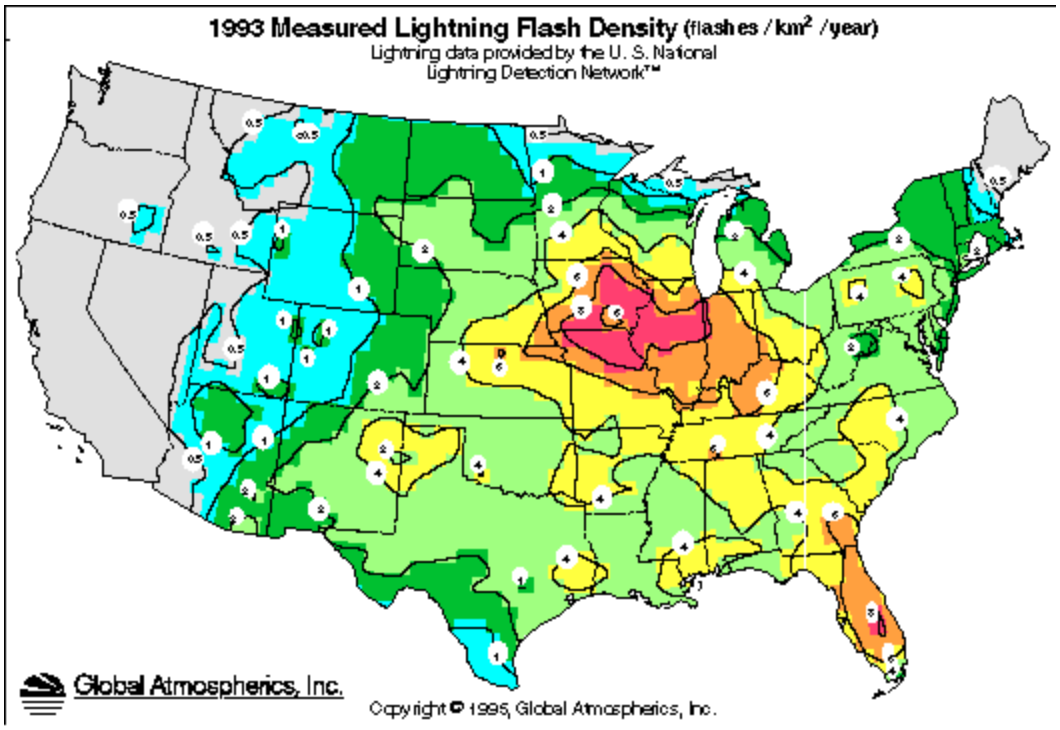

Figure 1. 3: Typical measured lightning flash density in the U.S.

Source: McCoy, Rhoads, Lisman, McNiff, & Smith, (2000). National Renewable Energy Laboratory.

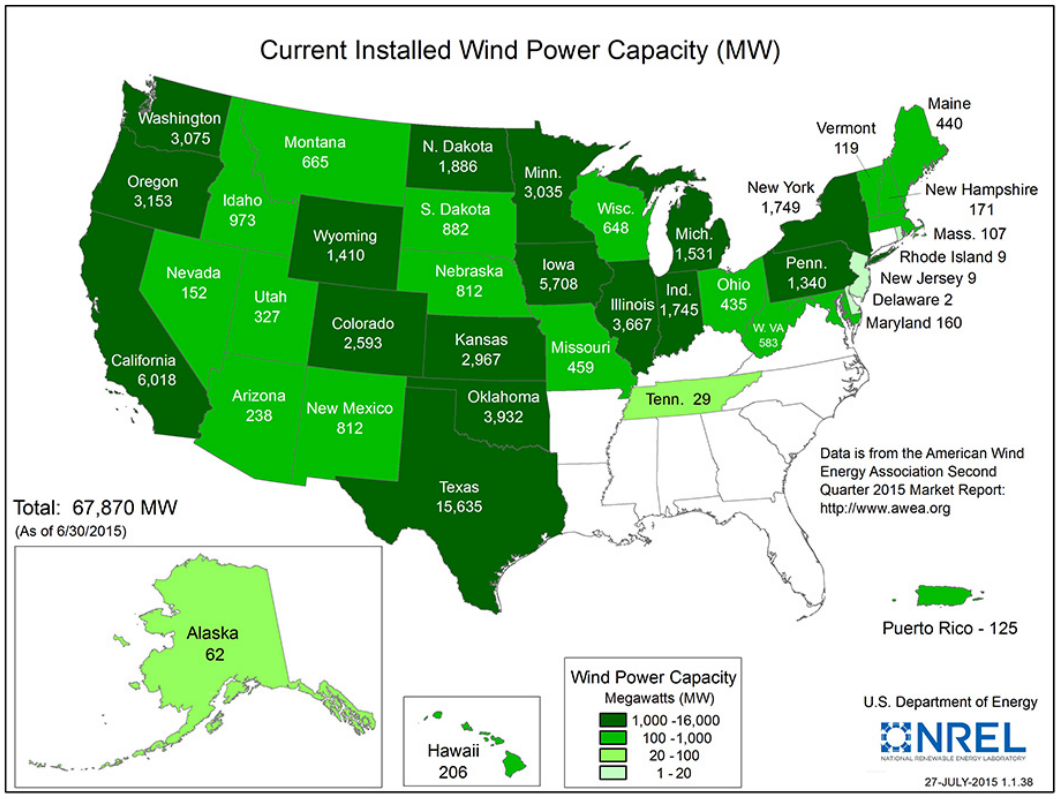

Figure 1. 4: Current installed wind power capacity (MV) in the U.S.

Source: U.S. Department of Energy, WINDExchange. Retrieved from: http://apps2.eere.energy.gov/wind/windexchange/wind_installed_capacity.asp.

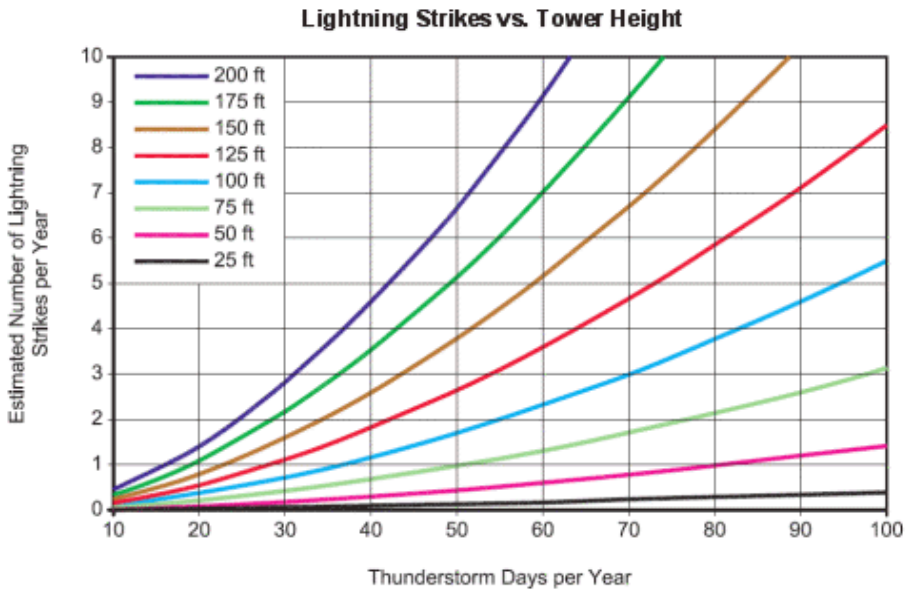

Figure 1. 5: Lightning strikes vs. wind turbine tower height.

Source: Lightning protection, Solacity Inc. Retrieved from: http://www.solacity.com/lightning.htm.

1.3 Thesis Objective

The main goal of this thesis is to develop models and computational procedures for predicting lightning-induced thermal response and thermal ablation damage in laminated fiber-reinforced polymer-matrix composites with application to wind turbine blades.

Specific research objectives are:

1. To develop a finite element analysis (FEA) procedure for calculating the electric field in the wind turbine blades due to a lightning stepped leader. The electric field is necessary in order to assess whether or not the dielectric breakdown of a

non-conductive structure (e.g. a glass-fiber-reinforced polymer-matrix composite blade) occurs.

2. To develop a physics-based model describing thermal interaction between the lightning channel and the composite structure. The model has to account for: (i) spatial and temporal evolution of the lightning channel as a function of the electric current waveform; (ii) temporary and spatially non-uniform heat flux and current density at the composite structure (the heat flux has to be an explicit function of the electric current waveform and the instant lightning channel radius); and (iii) nonlinear transient heat transfer in anisotropic composites capturing moving boundary of the expanding lightning channel and phase transition moving boundary associated with instantaneous material removal due to sublimation.
3. To develop a physics-based model describing electrical and thermal interactions between the lightning channel and the electrically conductive carbon-fiber-reinforced polymer-matrix (CFRP) composite structure. The model has to account for the nonlinear heat transfer due to the surface heat flux (objective 2), as well as Joule heating generated by an electric current passing through the structure.
3. To develop micromechanics-based models enabling determination of temperature-dependent thermal and electrical properties in the glass-fiber- and carbon-fiber-reinforced polymer-matrix composites with application to a lightning strike problem.
4. To implement the developed models into a finite element code and to apply the models for evaluation of thermal response and thermal ablation damage in the non-conductive All-glass Baseline Wind Turbine Blade (SNL 100-00) subjected to the lightning strike.

5. To apply the developed models for evaluation of thermal response and thermal ablation damage in the conductive CFRP composite and to validate the models through comparisons with existing experimental data.

CHAPTER 2

LITERATURE REVIEW

2.1 Physics of Lightning Strikes

Lightning discharge is essentially dielectric breakdown of the air (~3 MV/m), which is initiated by a large electric field established between the cloud and the earth or between two clouds. Air molecules are ripped apart, leaving free electrons and positive ions due to the large electric field. The electric field between the cloud and the earth or between two clouds accelerates these charges, causing a rapid charge motion, which heats the nearby air molecules and leads to a rapid air volume expansion emanating sound waves (thunder). As the lightning channel briefly becomes a plasma, the surrounding air temperature can be heated up to 50,000 °F, which is almost five times the temperature of the Sun's surface. The lightning plasma channel can discharge an electricity current up to 200 kA. In the process of the lightning discharge, the plasma channel also emits light, radio waves, x-rays, and even gamma rays (Rupke, 2002). Lightning discharge includes one or more intermittent partial discharges; each component discharge is called a stroke. Typically, lightning strike consists of four strokes: initial stroke, intermediate stroke, continuing stroke, and restrike stroke (see Figure 2. 1).

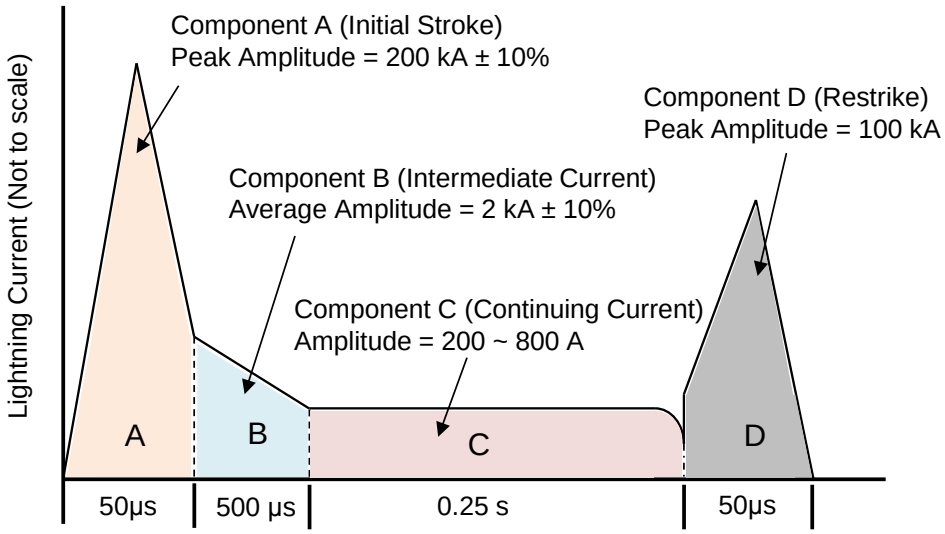

Figure 2. 1: Lightning discharge strokes MIL-STD-464.

Source: MIL-464-A. (1997). US Department of Defense.

Prior to the first lightning return stroke, a weakly luminous lightning stepped leader travels through the air towards the ground attempting to arrest the answering leaders emitted from the grounded structures. Once the lightning stepped leader connects with the answering leader, the first luminous lightning return stroke is formed. The distance between the lightning stepped leader and the grounded structure prior to the connection with the answering leader is called the lightning striking distance. Common structures that can emit answering leaders are electrically conductive such as transmission towers, TV towers, etc. However, electrically non-conductive structures (e.g., GFRP composite wind turbine blade) are also able to emit answering leaders if conductive components or conductive contamination (salt, dirt, moisture, etc.) are included (Madsen, Holbøll, Henriksen, & Sørensen, 2006).

The leader prior to the first return stroke is called a stepped leader and is different from the subsequent strokes as it develops in virgin air. The first return-stroke current has

a pulsed profile with a peak reaching up to hundreds kiloamperes. The electric current return-stroke wave heats and pressurizes the stroke channel leading to the rapid channel expansion, optical radiation, and shock wave propagation in the outward direction. A short-duration pulsed current in a return stroke is typically followed by a continuous current, whose magnitude is about two orders of magnitude lower and three orders of magnitude longer than that of the initial pulsed current.

Most of the early lightning strike studies were focused on the physics of the lightning return stroke and the prediction of the electric and magnetic fields observed at remote distances (Rakov & Uman, 1998). Gas dynamics models were developed to determine evolution of the lightning channel, its temperature and pressure, and associated shock wave (Borovsky, 1998; Braginskii, 1958; Dubovoy, Mikhailov, Ogonkov, & Pryazhinsky, 1995; Hill, 1971, 1977, 1990; Paxton, Gardner, & Baker, 1986; Plooster, 1971a, 1971b; Rakov & Uman, 1998).

2.2 Direct Effects of Lightning Strike on Composite Materials

Lightning strike poses a serious safety hazard for composite structures (e.g., aircrafts and wind turbine blades). The direct effects often include rapid temperature rise, melting or burning on the lightning attachment points, and mechanical damage due to magnetic force and acoustic shock wave (Rupke, 2002). In particular, the non-steady lightning plasma channel is expanding in both space and time during a short-duration pulsed current and is discharging an electric current up to 200 kA (MIL-464-A, 1997). This leads to the direct heat flux injection at the surface of the composite structure as well as the production of Joule heating (if the structure is electrically conductive) through the

composite structure. Both direct heat injection and Joule heating lead to a rapid temperature increase in the composite structure, which often results in severe surface damage and even catastrophic structural failure. The material properties of the composite materials are temperature-dependent and quickly deteriorate above the glass transition temperature. A rapid degradation of the polymer matrix occurring at a temperature above the glass transition temperature leads to deterioration in composite strength and elastic moduli. Extreme heating generates an extreme temperature in the structure and results in material phase transitions (i.e., fiber sublimation).

In addition to thermal damage, lightning strike also induces mechanical damage. The accumulation of Joule heating due to the lightning current conduction through the composite structure decomposes the polymer matrix and releases pyrolysis gases. Delamination occurs when the explosive pyrolysis gases are trapped in a substrate or between the layers of the laminated plies. If the stress caused by the internal pressure of the pyrolysis gases exceeds the rupture strength of the fibers, fiber breakage develops and results in surface cracks (see Figure 2. 2). Inoue et al. (2004) studied the relationship between the pressure rise inside the composite wind turbine blade and the energy of a spark arc. They reported that the internal pressure between the laminate layers of the composite wind turbine blade is proportional to the arc energy that is enforced on the composite blade surface. Furthermore, the lightning plasma channel also produces a magnetic force and an acoustic shock wave, which also lead to mechanical impact damage on the composite structures (Chemartin, Lalande, Delalondre, Cheron, & Lago, 2011; Muñoz et al., 2014). An overview of the lightning strike's direct effects on polymer-matrix composite structures is shown in Figure 2. 3.

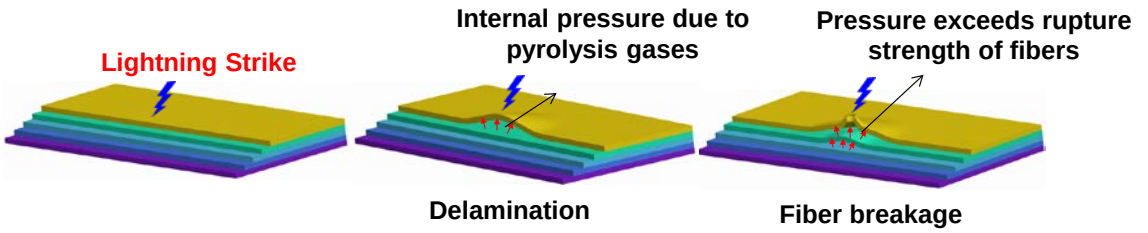

Figure 2. 2: Lightning-induced delamination and fiber breakage in polymer-matrix composite structures.

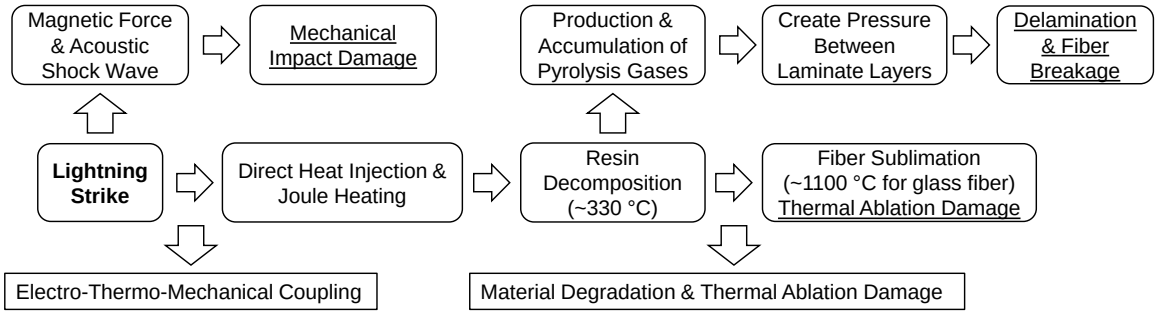

Figure 2. 3: Lightning strike electro-thermo-mechanical coupling in composite structures.

2.2.1 Lightning-Induced Dielectric Breakdown on Non-conductive Composite Structures

The direct effects of lightning strikes on non-conductive composite structures such as glass-fiber-reinforced polymer-matrix (GFRP) composite wind turbine blades may also include dielectric breakdown (Rupke, 2002). When lightning hits a non-conductive composite structure, the electric field on the attached spot will be significantly enhanced corresponding to the lightning discharge. Once the strength of the lightning-induced electric field exceeds the dielectric breakdown strength of the composite

structure, dielectric breakdown happens. In the situation of dielectric breakdown, the non-conductive composite structure becomes instantaneously conductive, thereby generates extensive Joule heating through the composite structure and even leads to puncture through the structure. It has been reported that the electrical field required to puncture a given thickness of glass fiber or aramid fiber composite is slightly greater than that required to ionize a similar thickness of air due to the high porosity and inhomogeneity of the composite structure (Rupke, 2002).

2.2.2 Lightning Surface Flashover on Non-conductive Composite Structures

When a lightning plasma arc attaches to the surface of the non-conductive composite structure (e.g., wind turbine blades), it automatically searches for the weakest spots (i.e., least resistant) to conduct the lightning electric current. Flashover occurs on the surface of the structure when the strength of the electric field induced by the lightning strike reaches the surface flashover field strength. The surface flashover field strength is typically lower than dielectric breakdown strength.

Flashover is usually inevitable prior to the dielectric breakdown in the non-conductive composite structures. The surface flashover is also known as streamers. Figure 2. 4 shows the electric arc streamers on a tested glass-fiber-reinforced polymer-matrix (GFRP) composite sample (Madsen et al., 2006). The streamers emitted from the high voltage electrode above the center of the plates move toward the edges, and connect with the ground electrodes (Madsen et al., 2006).

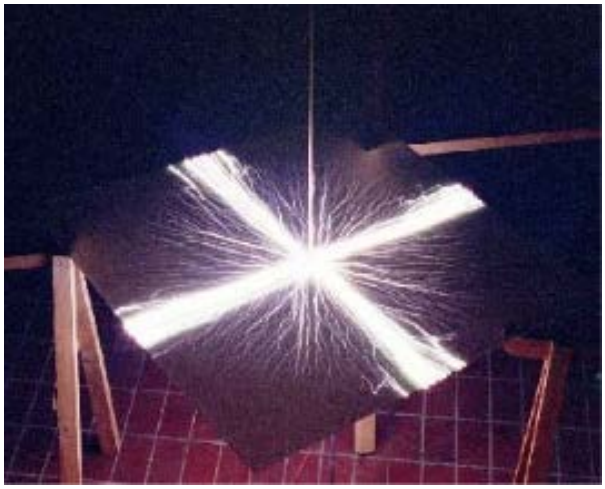

Figure 2. 4: Surface flashover on the surface of a glass-fiber-reinforced polymer-matrix composite sample.

Source: Madsen et al. *IEEE International Symposium on Electrical Insulation*, 19-22 September 2004, Indianapolis, IN, USA.

2.3 Recent Studies on Lightning Strike Damages in Composite Materials

As described previously, lightning strike raises a significant concern for composite structures. Many researchers have carried out studies to investigate the lightning strike damage mechanism, and have attempted to develop solutions to mitigate lightning strike damage for composite structures.

2.3.1 Experimental Studies

Electrical conductivity of the composite structures can have a great impact on the lightning-induced thermal damage. Composite structures with higher electrical

conductivity generate less Joule heating. Gou et al. (2010) studied the effect of electrical conductivity on the lightning-induced damage in carbon-fiber-reinforced polymer-matrix (CFRP) composite materials. They found that adding a layer of carbon nanofibers and nickel nanostrands on the surface of the composite panels can greatly increase the surface electrical conductivity of the composite panel. The highly conductive surface provides a relatively safer conduction of lightning current, thus protecting the composite itself. Figure 2. 5 shows an example of surface damage on the composite panels due to artificial lightning tests (Gou et al., 2010).

Figure 2. 5: Lightning-induced surface damage in composite panels.

Source: Gou et al. (2010). *Composites Part B: Engineering*, *41*(2), 192-198.

As discussed earlier, lightning damage in composite materials includes resin decomposition, delamination, and fiber breakage. Previous research showed that each damage mode in a laminated CFRP composite correlates with a particular lightning strike parameter (Hirano, Katsumata, Iwahori, & Todoroki, 2010). For example, the area and depth of the damaged fibers correlate with the peak current of the lightning pulsed current, while the area of resin deterioration and delamination are governed by the

electrical charge and the action integral of the lightning current waveform. However, changing both the size and thickness of the laminated composite had insignificant impact on the damage response under the experimental conditions in their study. Figure 2. 6 shows the section view of lightning-induced delamination and fiber breakage in a laminated CFRP composite.

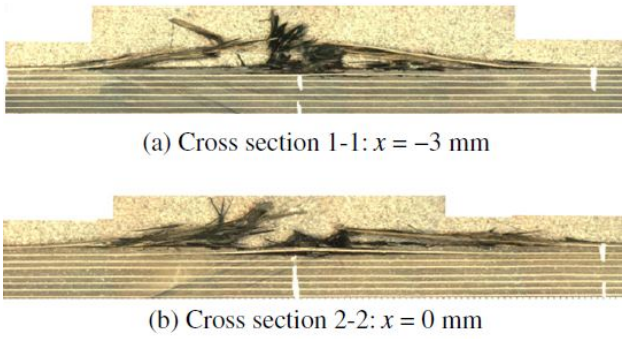

Figure 2. 6: Section view of lightning-induced delamination and fiber breakage in laminated CFRP composite.

Source: Hirano et al. (2010). *Composites Part A: Applied Science and Manufacturing, 41*(10), 1461-1470.

Lightning strike not only induces instant localized damage on the attached spot of composite structures, but also leads to mechanical strength degradation in the overall composite structure. It was found that the ultimate compressive strength of the laminated nanocomposite underwent a reduction of 30%~75% after lightning strike (Mall, Ouper, & Fielding, 2009). Another study on lightning-induced damage in CFRP composites reported that both the tensile and compression strength decreased in a relatively linear fashion with the current intensity of the lightning strike (Feraboli & Miller, 2009).

2.3.2 Computational Studies

The experimental studies on lightning strike damage in composite materials qualitatively revealed the damage mechanism. However, to quantitatively understand the lightning-induced damage in composite structures, a physics-based mathematical formulation needs to be developed. Ogasawara et al. (2010) performed a coupled thermal-electrical analysis with finite element analysis (FEA) to simulate the lightning strike in laminated carbon-fiber-reinforced polymer-matrix (CFRP) composites. The lightning current was assumed to be a concentrated point current. The model setup in FEA is shown in Figure 2. 7. The lightning-induced delamination area in the laminated composites was estimated according to the obtained temperature distribution. Ogasawara et al. (2010) assumed the decomposition of the polymer-matrix starts at 300°C at a heating rate 1000 °C/min. The decomposition area where the temperature exceeds 300 °C is assumed to be the delamination area.

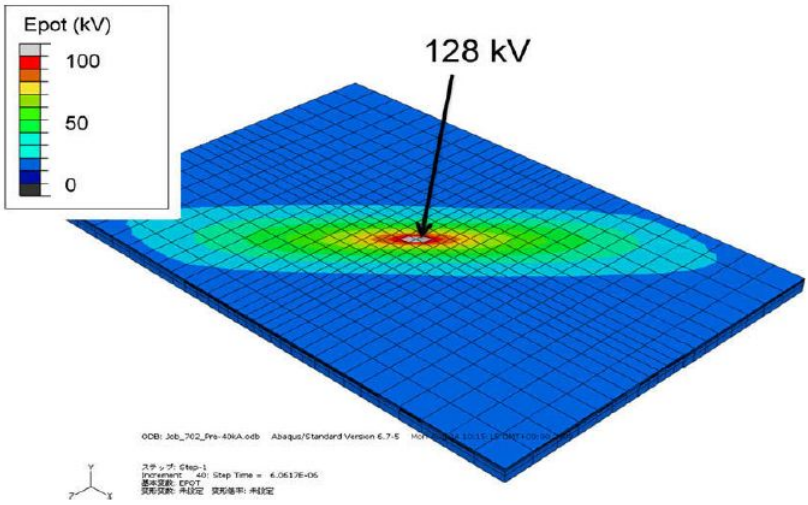

Figure 2. 7: Model setup of coupled thermal-electrical analyses with FEA to simulate the lightning strike in laminated carbon-fiber-reinforced polymer-matrix composites.

Source: Ogasawara et al. (2010). *Composites Part A: Applied Science and Manufacturing, 41*(8), 973-981.

F. S. Wang et al. (2014) carried out a computational analysis to investigate the residual strength of laminated carbon fiber/epoxy composites after lightning strike. It was found that the residual strength of the laminate composite decreases with the increasing peak value of lightning pulsed current. The tensile strength reduction of the carbon fiber/epoxy composite laminate is approximately 20% subjected to a pulsed lightning current with the peak value 50 kA. The tensile load and displacement curve for the lightning damaged and undamaged carbon fiber/epoxy composite laminates is shown in Figure 2. 8. The difference between the maximum load before the composite underwent severe failure is around 6% for lightning-damaged and undamaged composite laminates (F. S. Wang et al., 2014).

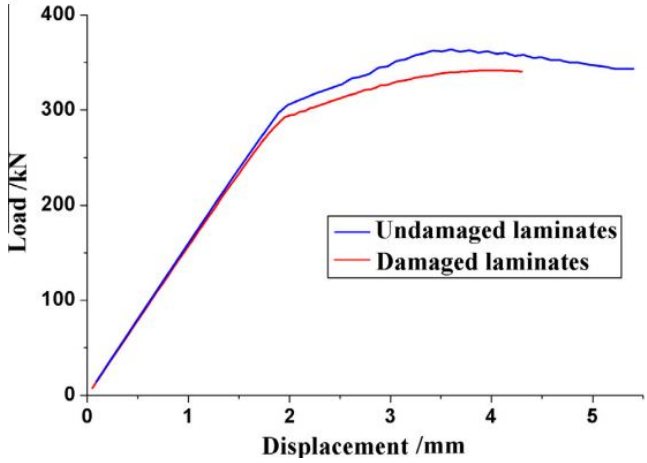

Figure 2. 8: Relationship between load and displacement for lightning-damaged and undamaged laminated composites.

Source: F. S. Wang et al. (2014). *Composite Structures, 117*, 222-233.

In order to mitigate lightning strike damage in composite materials, a thin metallic conductive mesh is often attached to the surface of the composite structure to serve as a protective layer. A computational analysis was carried out with FEA by Abdelal & Murphy (2014) to investigate the lightning-induced thermal ablation damage in unprotected and protected (with copper mesh) carbon fiber/epoxy composite laminates. It was reported that their simulation results agree well with the experimental data for unprotected composite laminates. As expected, the simulation results for protected composite laminates showed a reduction in thermal ablation damage through the thickness. However, their simulation also showed that the addition of copper mesh introduced undesirable damage due to heat conduction between the copper mesh layer and the adjacent composite lamina (Abdelal & Murphy, 2014).

In addition to the computational studies on lightning-induced thermal damage, mechanical damage due to lightning-induced electromagnetic and acoustic pressure has also been investigated in some studies. For example, Muñoz et al. (2014) formulated the

magnetic and acoustic pressure field distribution on the composite panel during the lightning impact (shown in Figure 2. 9) on a composite laminated panel. The response of the carbon composite panels due to the formulated lightning-induced magnetic and acoustic pressure was investigated using FEA. It was found that moderate stresses around the lightning impacted area had been developed which led to minor diffuse damage by matrix cracking/delamination in the composite panel. Muñoz et al. (2014) also performed a separate coupled electric-thermal simulation for investigating the thermal damage in a carbon composite panel due to the production of lightning-current-induced Joule heating. By comparing the predicted thermal damage with the predicted mechanical damage, it was found that the majority of the lightning-induced damage was attributed to thermal damage (Muñoz et al., 2014).

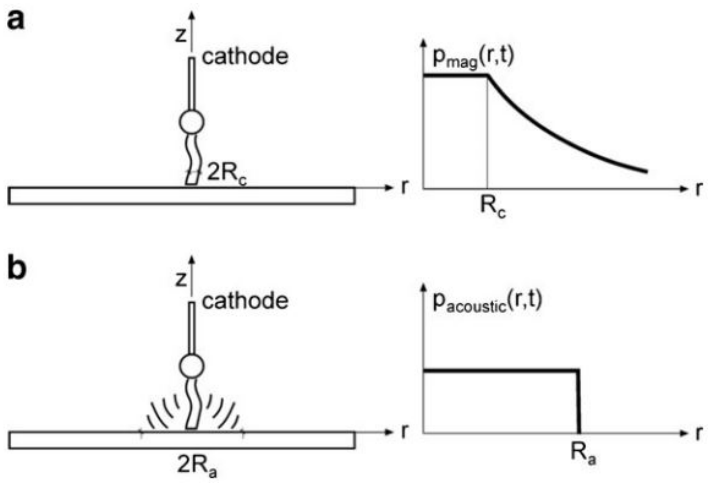

Figure 2. 9: Electromagnetic pressure distribution (a), Acoustic pressure distribution (b).

Source: Muñoz et al. (2014). *Applied Composite Materials*, *21*(1), 149-164.

2.3.3 Limitations of Current Computational Studies

The common feature of the current studies is the examination of carbon-fiber-reinforced polymer-matrix (CFRP) composites, which are widely used in the design of aerospace structures (Abdelal & Murphy, 2014; Muñoz et al., 2014; Ogasawara et al., 2010; F. S. Wang et al., 2014). Lightning-induced thermal damage is a major focus of these studies, as polymer-matrix composites are adversely affected by the heating. At temperatures above glass transition, a rapid degradation of the polymer matrix occurs, which leads to deterioration in composite strength and elastic moduli (Bai & Keller, 2007; Cao, Zhis, & Wang, 2009; Feih & Mouritz, 2012; Landel & Nielsen, 1993). Carbon fibers are electrically conductive, and polymer matrix is usually dielectric. Thus, overall carbon-fiber-reinforced polymer-matrix composites are electrically conductive, and interaction with lightning current induces direct heat injection at the surface of the composite as well as Joule heating produced by conducting through carbon fibers. Glass-fiber-reinforced polymer-matrix (GFRP) composites are also widely used in structural applications, including wind turbine blades (Ashwill & Paquette, 2008; Brøndsted, Lilholt, & Lystrup, 2005; Madsen et al., 2006). Lightning strikes are among the top two most frequently reported causes of loss in wind energy insurance claims in the United States (GCube, n.d.). A better understanding of the response of GFRP composites to a lightning strike is essential for the development of the lightning strike protection systems on non-conductive composite structures.

The models currently utilized to describe the interaction of the lightning channel with a structure (Abdelal & Murphy, 2014; Muñoz et al., 2014; Ogasawara et al., 2010; F. S. Wang et al., 2014) rely on a number of simplifying assumptions, including concentrated lightning electric current (Ogasawara et al., 2010; F. S. Wang et al., 2014) or surface lightning electric current with a constant (and fixed in advance) radius of the lightning channel (Abdelal & Murphy, 2014; Muñoz et al., 2014), uniform surface heat

flux, and inadequate treatment of material phase transitions (Abdelal & Murphy, 2014; Muñoz et al., 2014; Ogasawara et al., 2010; F. S. Wang et al., 2014). Expansion of the lightning channel radius during the initial pulsed current of the return stroke, which is described in all gas dynamic models (Borovsky, 1998; Braginskii, 1958; Dubovoy et al., 1995; Hill, 1971, 1977, 1990; Paxton, Baker, & Gardner, 1987; Paxton et al., 1986; Plooster, 1971a, 1971b) is ignored, and instead a concentrated lightning electric current or a fixed lightning channel radius is assumed based on some input from the experiments and analyses of the effects of a continuing current are presented. This significantly simplifies a mathematical treatment of the problem, as it fixes the lightning channel boundary and reduces the problem complexity to dealing with temperature-dependent material properties and material phase transitions. At the same time, such simplification affects the predictive capabilities of the models.

In addition, in the existing literature, no actual progressive thermal ablation was modeled within the FEM simulation. In the work by Ogasawara et al. (2010), the damage zones (i.e., delamination zone, surface recession zone) affected by the lightning-strike-induced heat were estimated from the temperature distribution obtained from the simulations. The same method of damage estimation has been adopted by Muñoz et al. (2014). Abdelal & Murphy (2014) assumed that the thermal ablation in the CFRP composite laminated panel comes from material surface vaporization and used the Hertz-Knudsen equation to track the ablation rate. In addition, to move the electric current boundary condition to the next laminate layer once the preceding laminate layer was ablated, the CFRP composite laminated panel was assumed to have a fictitious high electrical conductivity (1×10^6 S/mm) in the through-the-thickness direction when ablation occurs at 3316 °C (Abdelal & Murphy, 2014). However, none of these studies (Abdelal & Murphy, 2014; Muñoz et al., 2014; Ogasawara et al., 2010) predicted the progressive shape change (i.e., ablation profile) of the CFRP composite laminated panel.

CHAPTER 3
PHYSICS OF LIGHTNING INTERACTION WITH WIND TURBINE BLADES

3.1 Lightning Strike Protection of Wind Turbine Blades

The overwhelming majority (90% and more) of cloud-to-ground lightning is the so-called downward negative lightning discharge, where negative charge is transported from the cloud to the ground (Rakov, 2007, 2013). As opposed to downward lightning discharge, the upward lightning discharge extends from the ground to cloud. As a structure height increases, the fraction of upward lightning discharges increases. Structures with heights ranging from 100 m to 500 m experience both upward and downward lightning discharges. It is reported (Rakov, 2007) that upward lightning discharges constitute 50% in the 200-meter tall structures and 80% in the 300-meter tall structures. Therefore, both upward and downward lightning discharges are quite common in tall structures and are worth of consideration.

For a typical negative-polarity, downward-initiated, cloud-to-ground lightning discharge, the initial lightning stepped leaders are formed from the lower part of the cumulonimbus cloud (with negative charges) approaching the ground (Rakov & Uman, 2003). When the lightning stepped leader tip gets within a certain distance (striking distance) of a grounded structure, the answering leaders emitted from the grounded structures due to the lightning electric field attempt to capture the lightning stepped leaders. Once they are connected, the first lightning return stroke occurs (the situation works the same way with other types of cloud-to-ground lightning discharge). This indicates that the lightning attachment point on the ground structure is determined before any lightning current is conducted. Structures such as metallic conductors are able to emit

answering leaders (as conductors allow electric charges to move freely under lightning electric field). Non-conductive structures such as glass-fiber-reinforced polymer-matrix (GFRP) composite wind turbine blades are also able to emit answering leaders due to the presence of internal down conductors, receptors and surface contaminations (e.g., moisture, dirt).

Wind turbine blades are designed with lightning strike protections (LSP). The common way is to use receptors and down conductors (IEC-61400-24, 2002). The receptors are evenly embedded on each side of the wind turbine blade. The receptors are made of a special tungsten alloy with excellent conductive qualities and resistance to intense heat. They are connected to the down conductors inside the blade shell (shown in Figure 3. 1). The down conductors are unshielded high-voltage cables going from the wind blade tip region to the root of the blade. The answering leaders are expected to be emitted from one or more of the installed receptors, such that the lightning current can be safely conducted through the down conductor to the ground, possibly leaving a pit mark on the receptor (Madsen et al., 2006). The receptors undergo partial evaporation with repeated lightning strikes; they need to be replaced after several lightning strikes.

Figure 3. 2 and Figure 3. 3 show examples of the common lightning protection systems used on real wind turbine blades.

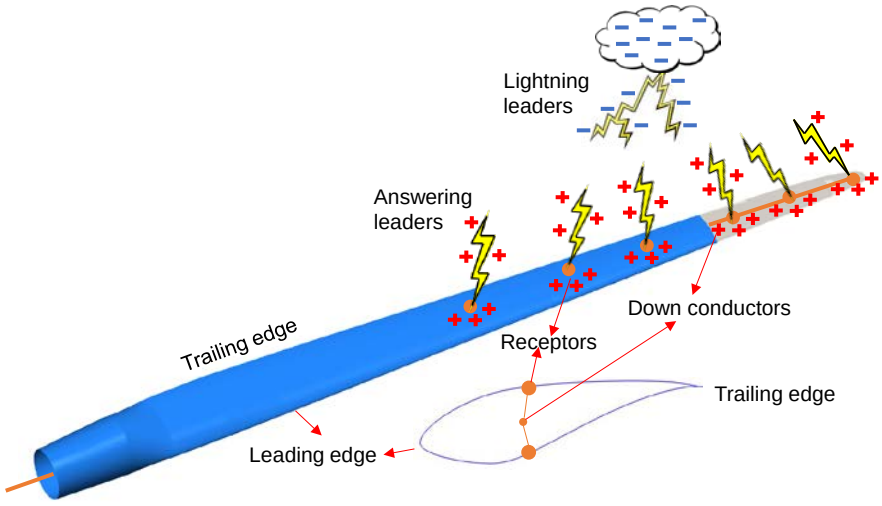

Figure 3. 1: Schematic of the formation of lightning leaders and answering leaders emitting from the receptors of the wind turbine blade.

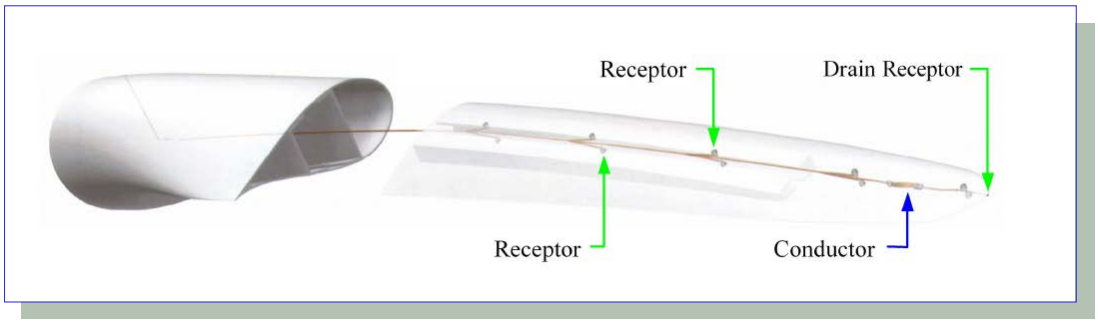

Figure 3. 2: Example 1 for common lightning protection system of wind turbine blades (LM Glassfiber, Denmark).

Source: Lewke et al. (2007). 2007 EWEC Europe's premier wind energy event. Retrieved from: http://www.ewea.org/ewec2007/allfiles/41_Ewec2007presentation.ppt.

Figure 3. 3: Example 2 for common lightning protection system of wind turbine blades. (LM Glassfiber, Denmark).

Source: Lewke et al. (2007). 2007 EWEC Europe's premier wind energy event. Retrieved from: http://www.ewea.org/ewec2007/allfiles/41_Ewec2007presentation.ppt.

3.2 Lightning Current Conduction on Wind Turbine Blade

Despite lightning strike protections are used on wind turbine blades, lightning strike damage is still not avoidable if the answering leader emitted from the non-conductive areas other than the receptors on the blade surface arrests the lightning stepped leader. It has been reported that many wind turbine blades with the receptor and down conductor system are still subjected to lightning strike damage (Madsen et al., 2006). This is because the large lightning electric field ionizes the molecules on the down conductor. It deposits the ionized positive charges on the interior surface of the blade and induces negative charges on the exterior surface (see Figure 3. 4 (a)). If the positive charges on the receptor search for and neutralize these negative charges, the searching

path (non-conductive area) can emit multiple answering leaders (see Figure 3. 4 (b)). If one of them arrests the approaching lightning stepped leader, the lightning arc channel is directly injected into the attachment surface (see Figure 3. 4 (c)), leading to a significant temperature increase and resulting in appreciable thermal damage. In addition, severe damage develops if the electric field at the lightning attachment point is sufficiently large to cause a dielectric breakdown of the GFRP composite (see Figure 3. 4 (d)) (Madsen et al., 2006).

In other words, prior to the dielectric breakdown of the GFRP composite wind turbine blade, the majority of the thermal damage is attributed to the direct heat conduction due to the lightning channel attachment on the surface of the structure. However, if the electric field induced by a lightning stepped leader is large enough to cause dielectric breakdown of the non-conductive structure, a considerable amount of Joule heating is produced through the composite wind turbine blade. In this case, Joule heating must be considered in the thermal damage model in addition to the direct heat conduction. Therefore, an estimation of dielectric breakdown in the GFRP composite wind turbine blade subjected to a lightning stepped leader is essential and inevitable prior to any modeling of thermal damage in non-conductive structures (i.e., GFRP wind turbine blades) subjected to lightning strike. Sections 3.3 to 3.7 describe the formulation and computational procedures that we carried out to estimate the dielectric breakdown in the GFRP composite wind turbine blade subjected to a lightning stepped leader.

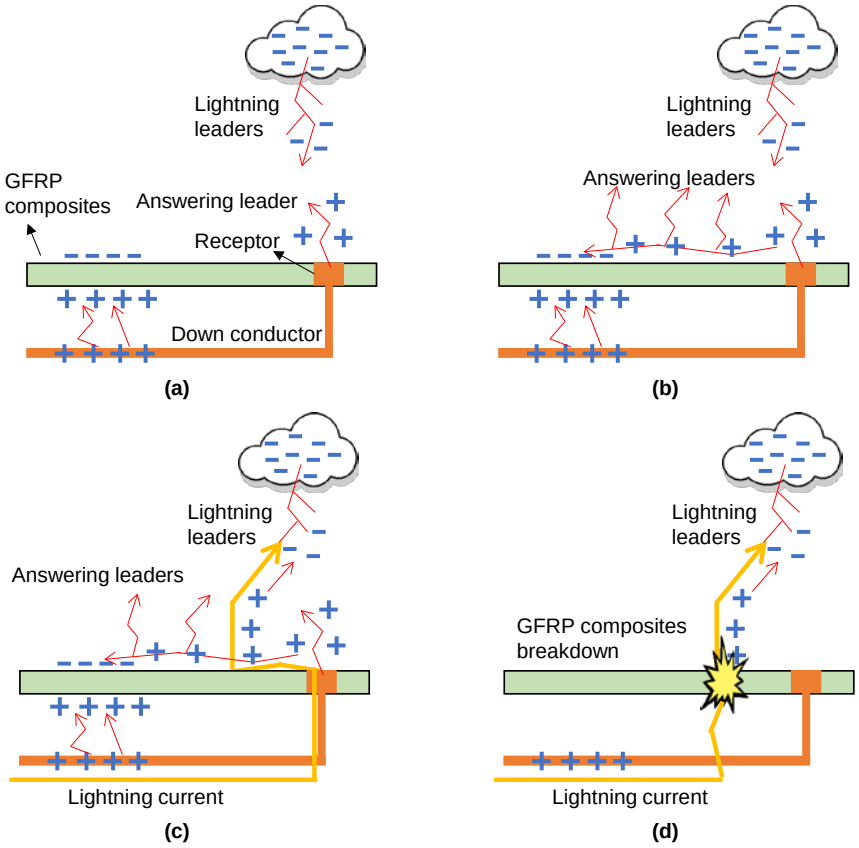

Figure 3. 4: Lightning attachment on a non-conductive surface.

3.3 Literature Review on Lightning Stepped Leader Models

There have been a number of studies on the lightning stepped leaders conducted in the past. Larigaldie et al. (1981), and Larigaldie (1987) experimentally studied the propagation and electric current intensity of a typical lightning stepped leader. Larigaldie et al. (1992) performed experimental and numerical investigation of the mechanisms of high-current pulses in lightning and long spark stepped leaders. Golde (1945, 1973) developed a vertical lightning stepped leader model and was the first to introduce the

non-uniform charge density of the leader into the analysis. Recently, Cooray et al. (2007) derived a different non-uniform charge density distribution along the lightning stepped leader using the charge simulation method. The distribution has been validated using measurements of the in-field lightning incidents and was used to obtain a new expression for calculating the lightning striking distance (see equation (3-2) in Section 3.4 below), which was also found in better agreement with the physical measurements than the expression previously proposed by Uman (2001) (see equation (3-1) in Section 3.4 below). All these leader models are for downward lightning flashes, the upward leader models have barely been reported (Zhou et al., 2012). The models developed by Uman (2001) and Cooray et al. (2007) are commonly used in the literature for the estimation of the electric fields due to the lightning stepped leaders. For instance, the Cooray et al. (2007) model was used by Becerra (2008) for calculation of the electric field distributions in complex ground structures. Lewke et al. (2007) used the same model to determine the electric field in a wind turbine tower. Both studies (Becerra, 2008; Lewke et al., 2007) were performed using finite element analysis (FEA). One of the limitations of the aforementioned studies is that a computational domain in FEA were limited to the bottom part of the lightning stepped leader (close to the ground structure) and the upper part (close to the cloud) was not taking into account. Such choice of the computational domain leads to underestimation of the electric field, and therefore, to under-prediction of the dielectric breakdown. The FEA conducted in the present study takes into account the full length of the lightning stepped leader (i.e., both the bottom and the upper parts), which enables accurate estimation of the electric field and occurrence of the dielectric breakdown.

3.4 Lightning Striking Distance

Prior to the first lightning return stroke, a lightning stepped leader originates from the cloud and travels through the air towards the ground. When the lightning stepped leader approaches the ground, the ground structure emits answering leaders (streamers) due to the intensified electric field. The answering leader propagates to meet the lightning stepped leader and forms the first lightning return stroke. The distance between the tip of the lightning stepped leader and the ground structure prior to the connection with the answering leader is called the lightning striking distance.

According to the IEC 61400-24 standard (IEC-61400-24, 2002) , in the wind turbine blades longer than 20 m, the lightning striking distance can be defined using the rolling sphere method, where the radius of the rolling sphere attached to the ground structure is considered to be equal to the lightning striking distance (see Figure 3. 5).

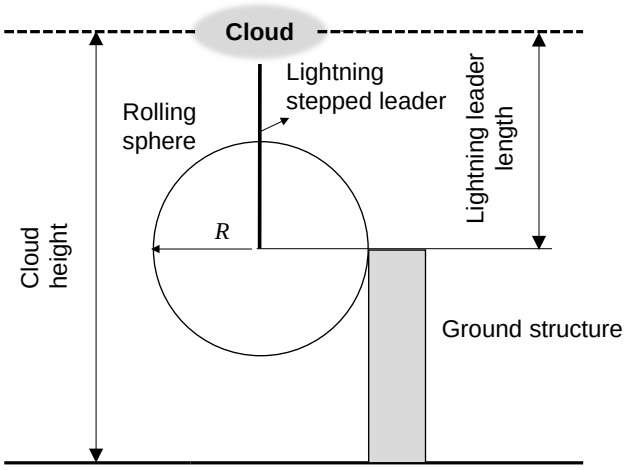

Figure 3. 5: Lightning striking distance from stepped leader tip to a ground structure characterized using the rolling sphere method.

The rolling sphere radius is a function of the peak current of the lightning return stroke. A traditional expression to calculate the sphere radius (and, therefore, the lightning striking distance) is given by Uman (2001)

$$R = 10 \cdot I_{\text{peak}}^{0.65}, \tag{3-1}$$

where I_{peak} is the peak current of the lightning return stroke (in kA), and R is the rolling sphere radius (in m).

More recently, Cooray et al. (2007) suggested another expression for the radius of the rolling sphere, which agrees better with the recorded physical measurement data on the lightning striking distances:

$$R = 1.9 \cdot I_{\text{peak}}^{0.90}, \tag{3-2}$$

where the rolling sphere radius R is in m; the unit of peak current I_{peak} is in kA.

Table 3. 1 shows the lightning striking distance calculated using equations (3-1) and (3-2) for three lightning protection levels (LPLs). The LPLs represent three different lightning severity levels as identified by the IEC 61400-24 (IEC-61400-24, 2002). Peak current I_{peak}=200 kA of the first short-duration stroke corresponds to LPL I, and I_{peak}=150 kA and I_{peak}=100 kA correspond to LPL II and LPL III, respectively. It can be seen in Table 3. 1 that the lightning striking distances calculated by equation (3-1) are around 1.5 times larger than those calculated by equation (3-2). Therefore, using equation (3-1) in a lightning stepped leader model will result in weaker electric field predictions at a ground structure compared to the predictions obtained when equation (3-2) is used. Since a more conservative estimate of the dielectric breakdown is obtained when a larger electric field

is considered, equation (3-2) is used in this work to calculate the lightning striking distances.

Table 3. 1: Lightning striking distance for the lightning stepped leader.

LPL	Peak Current, I_{peak} (kA)	Lightning Striking Distance (m)	
		From Eq. (3-1)	From Eq. (3-2)
I	200	313.09	223.71
II	150	259.69	172.68
III	100	199.53	119.88

It is worth mentioning that the lightning striking distance in conjunction with the rolling sphere method have been used in the previous studies of wind turbine blades (Lewke et al., 2007; Madsen et al., 2006). As a side note, below we discuss the difference between the striking distance and the attractive radius, which is also widely used in the modeling of lightning attachment to the structures.

The attractive radius can be calculated as (D'Alessandro & Petrov, 2006; Eriksson, 1979, 1987):

$$R_a = 0.84 \cdot I_{\text{peak}}^{0.74} h_a^{0.6}, \tag{3-3}$$

where R_a is the attractive radius (in m), I_{peak} is the peak current (in kA), and h_a is the structure height (in m). There is a significant difference between lightning strike distance, R, as defined by equations (3-1) and (3-2), and lightning attractive radius, R_a, as defined by equation (3-3). The first depends on the charge of the downward conductor only, whereas the later takes into account also the size of the structure. Figure 3. 6 shows the ratio R/R_a as a function of the structure height h_a for I_{peak}=100 kA. Depending on the

height of the structure, the striking distance magnitude can be larger or smaller than the attractive radius magnitude. For tall structures (i.e. h_a>20 m), the striking distance magnitude is smaller. Thus, using striking distance in a lightning stepped leader model will result in the prediction of a larger electric field at a ground structure, and, therefore, in a more conservative estimate for the dielectric breakdown.

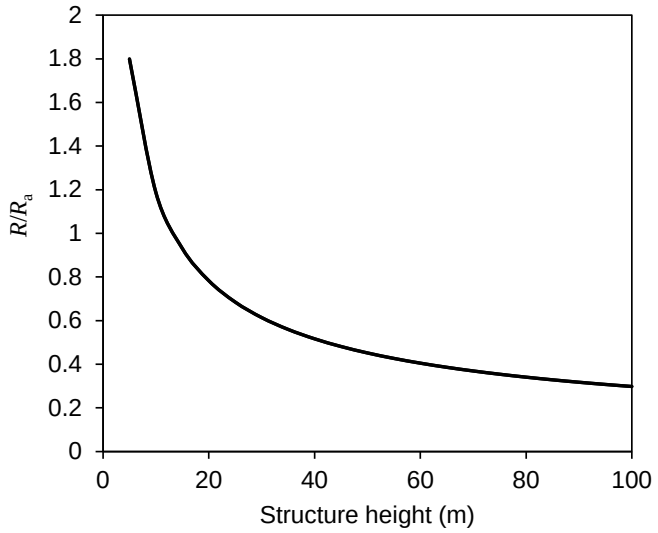

Figure 3. 6: Ratio of striking distance to the attractive radius as a function of the structure height (I_{peak}=100 kA).

3.5 Total Charge Associated with a Lightning Return Stroke

According to Cooray et al. (2007), when the lightning stepped leader approaches the ground, the charge density of the lightning stepped leader is determined by both the electric field due to the cloud charge and the electric field enhancement due to the presence of the ground. Figure 3. 7 shows a simple lightning stepped leader model

developed. A cloud is represented by a conductive plane at potential V, and the ground is represented by a perfect conductor. Figure 3. 7 (a) shows a real lightning stepped leader approaching the ground with branched channels; Figure 3. 7 (b) shows an idealized vertical lightning stepped leader; Figure 3. 7 (c) shows a negative charge Q_l along the lightning stepped leader before a return stroke; Figure 3. 7 (d) shows a positive charge Q_i flowing upward along the lightning channel after the return stroke was deposited on the fully-developed return stroke channel induced by the cloud voltage. The total positive charge, Q_t, entering from the ground to the fully-developed return stroke channel during the first 100 μs equals the sum of the positive charges that neutralize the negative charges Q_l stored along the lightning stepped leader and the positive charges Q_i due to the cloud voltage (Cooray et al., 2007):

$$Q_{t,100\,\mu s} = |Q_l| + Q_i = 0.61 \cdot I_{\text{peak}}, \tag{3-4}$$

where $Q_{t,100\,\mu s}$ is in C, I_{peak} is the peak current, in kA.

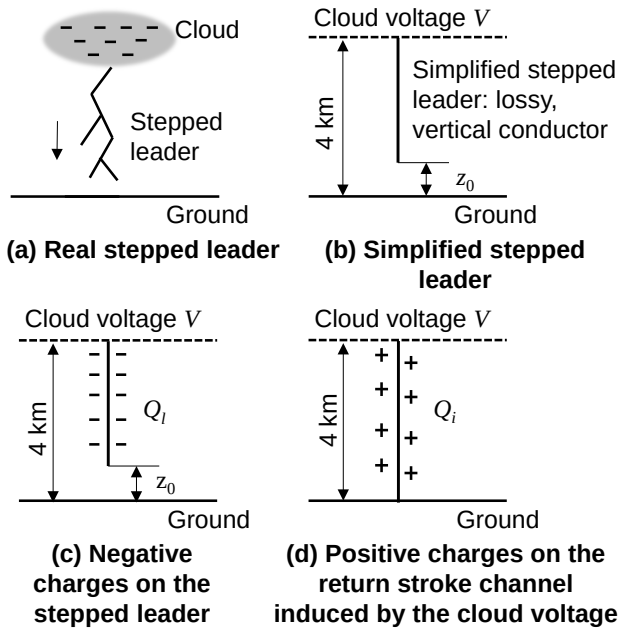

Figure 3. 7: Simplified lightning stepped leader model proposed by Cooray et al. (2007).

3.6 Charge Density of a Lightning Stepped Leader

Typically, the charge density of the lightning stepped leader is non-uniform (Becerra, 2008; Cooray et al., 2007; Golde, 1945, 1977; Lewke, Hernández, & Kindersberger, 2007). Golde (1945, 1977) assumed that the charge density decreased exponentially along the lightning stepped leader from the tip to the origin of the leader in the cloud,

$$\lambda(\eta) = \lambda_0 e^{-\eta/\xi}, \ 0 \le \eta \le L, \tag{3-5}$$

where λ is the charge density distribution (in C/m) along the leader, and λ_0 is the charge density at the leader tip; η is in m; ξ is the decay height constant, ξ=1,000 m; and L is the

length of the leader (in m). In addition, η=z-z_0, where z is the vertical distance from the ground (z=0 at the ground) and z_0 is the distance from the ground to the leader tip.

The total charge on the leader is obtained by integration of the charge density (3-5) along the leader length (Golde, 1945, 1977)

$$Q_l = \int_0^L \lambda(\eta) d\eta = \lambda_0 \xi [1 - e^{-L/\xi}], \tag{3-6}$$

where Q_l is the total charge (in C).

The relationship between the peak current of the lightning return stroke and the charge density at the leader tip is (Golde, 1945, 1977)

$$\lambda_0 = 4.36 \cdot 10^{-5} I_{\text{peak}}, \tag{3-7}$$

where I_{peak} is the peak current (in kA).

Using the charge simulation method, Cooray et al. (2007) derived a different non-uniform distribution for the charge density along the lightning stepped leader

$$\lambda(\eta) = a_0 \cdot \left(1 - \frac{\eta}{H - z_0}\right) \cdot G(z_0) \cdot I_{\text{peak}} + \frac{I_{\text{peak}} \cdot (a + b \cdot \eta)}{1 + c \cdot \eta + d \cdot \eta^2} \cdot F(z_0), \quad 0 \le \eta \le L, \ z_0 \ge 10, \tag{3-8}$$

where η, in m, is the distance along the leader; η=0 is at the leader tip, η=z-z_0; $\lambda(\eta)$ is the charge density (in C/m); H is the height of the cloud (typically H=4,000 m); z_0 is the distance from the ground to the leader tip (in m); I_{peak} is the peak current of the return stroke (in kA); and $G(z_0)$=1-(z_0/H), $F(z_0)$=0.3α+0.7β, β=1-(z_0/H), a_0=1.476·10^{-5}, a=4.857·10^{-5}, b=3.9097·10^{-6}, c=0.522 and d=3.73·10^{-3}. It is assumed that z_0>10 m.

Cooray et al. (2007) also found that distribution (3-8) was in a better agreement with the physical measurements than distribution (3-5) proposed by Golde (1945, 1977). The total charge on the leader is obtained by numerical integration of the charge density (3-8) along the leader.

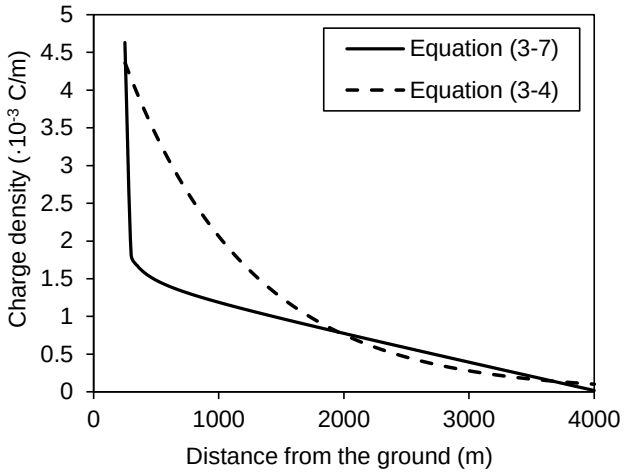

Figure 3. 8: Charge density along the lightning stepped leader for the LPL III (I_{peak}=100 kA, z_0=250 m).

Figure 3. 8 shows the charge density as a function of the height z. Calculations are performed using equations (3-5) and (3-8) for the LPL III (I_{peak}=100 kA). The distance from the stepped leader tip to the ground is z_0=250 m, and the length of the lightning stepped leader is L=3,750 m. As one can see, at the leader tip and at the vicinity of the cloud, the charge densities calculated by equations (3-5) and (3-8) are similar, but they are quite different in between. Table 3. 2 shows the total charge entering from the ground to the lightning channel, $Q_{t,\,100\,\mu s}$, calculated using equation (3-4) and provided by IEC

61400-24 standard (IEC 61400-24, 2002), and the total charge on the leader, Q_l, in the case of uniform (3-5) and non-uniform (3-8) charge density distributions. As one can see, the total charge is larger if charge density is uniform. However, the charge near the leader tip

$$Q_l^{tip} = \lim_{\eta \to 0} Q_l(\eta) = \lim_{\eta \to 0} \int_0^{\eta} \lambda(\eta) d\eta \tag{3-9}$$

is larger, if calculated using the charge density distribution (3-8). This is due to larger charge density near the tip predicted by the distribution (3-8) than that predicted by the distribution (3-5), as can be seen in Figure 3. 8. Since an electric field at a ground structure is mainly attributed to the charge at the bottom part of the lightning stepped leader (i.e., the leader tip), the electric field calculated using the charge distribution (3-8) will be larger than the electric field calculated using the charge distribution (3-5).

Table 3. 2: Total charge entering from the ground to the lightning channel, Q_t, 100 μs, and total charge on the lightning stepped leader, Q_l.

LPL	$Q_{t,\ 100\ \mu s}$ (C)		Q_l (C)	
	From IEC-61400-24	From Eq. (3-4)	From Eq. (3-6)	Integral of Eq. (3-8)
I	300	183	8.51493	5.70252
II	225	91.5	6.38619	4.27689
III	150	61	4.25746	2.85126

3.7 Modeling of the Electric Field in a Non-Conductive Wind Turbine Blade Due to a Lightning Stepped Leader

In this section, finite element analysis (FEA) is developed to determine electric fields in a non-conductive wind turbine blade due to a lightning stepped leader. Electric fields are calculated for the blades representing Sandia 100-meter All-glass Baseline Wind Turbine Blades (SNL 100-00) (Griffith & Ashwill, 2011). The FEA results are verified by comparisons with the analytical solution derived for the case of the leader with a uniform charge density. The electric fields obtained for the case of the leader with a non-uniform charge density (3-8) are compared to the dielectric breakdown strength of the blade to assess the conservativeness of the blade design. The dielectric breakdown strength is obtained using the experimental data reported in the literature (Madsen et al., 2006).

3.7.1 Problem Formulation

We consider a horizontal axis wind turbine blade that is subjected to a lightning stepped leader (see Figure 3. 9). Three blades, which are placed at a 150-m wind tower, represent Sandia 100-meter All-glass Baseline Wind Turbine Blades (SNL 100-00) (Griffith & Ashwill, 2011).

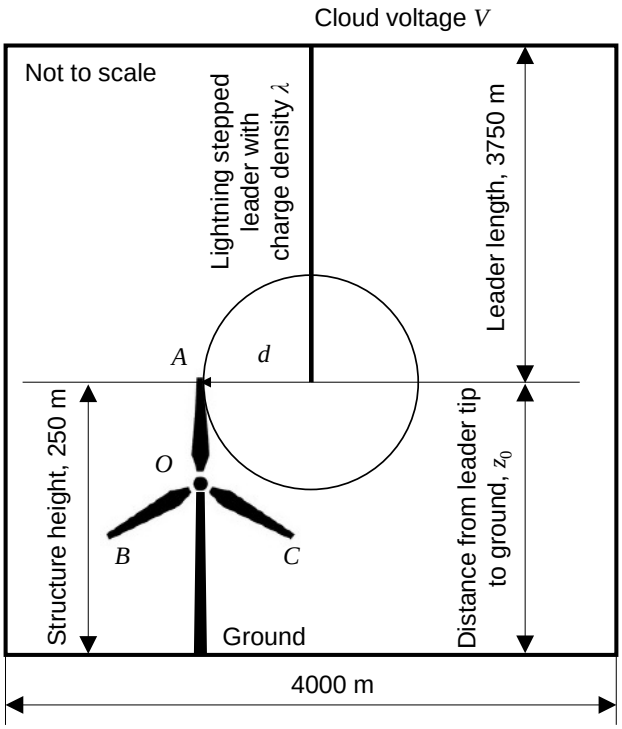

Figure 3. 9: Interaction of a lightning stepped leader and a wind turbine: problem formulation.

It is assumed that the leader is a vertical line charge that is perpendicular to the turbine axis and is located in the same plane with the blades (see Figure 3. 9). Both uniform and non-uniform charge density distributions on the leader are considered. The blades are assumed to be non-conductive. In other words, the effects of the receptors and down conductors on the electric field are ignored. The length of each blade is 100 m, the overall structure height (the length of the blade together with the height of the tower) is 250 m, and the distance from the leader tip to the ground z_0=250 m. The length of the lightning stepped leader is 3,750 m. The distance from the ground to the cloud is 4,000 m. Cloud voltage is assumed to be constant. A typical 100 m wind turbine blade is equipped with multiple receptors, which are evenly distributed at the surface and are connected to the internal down conductor. The down conductor is installed inside the

blade shell. Effects of the receptors and the down conductors are taken into account in the FEA study of Section 3.7.3, where ground potential is applied at the wind turbine exterior surface. Since blades are 100-meter long, the rolling sphere method is used to obtain the lightning strike distance (denoted as *d* in Figure 3. 9). It is assumed that the rolling sphere is tangentially attached to the tip of the blade *OA*. The lightning striking distance between the leader and blade *OA* is equal to the rolling sphere radius (2). Attachment to the tip is chosen because the tip region of the blade has the highest probability (>98%) to emit answering leaders (A detailed discussion on lightning strike attachment on wind turbine blade is in Section 5.2.1).

3.7.2 Electric Field Due to a Lightning Stepped Leader with the Uniform Charge Density: Analytical Solution

First, we consider a lightning stepped leader with the uniform charge density and find the electric field at the blade *OA* due to the leader (see Figure 3. 10). If the ground is assumed to be at the infinity and the electric potential between a cloud and the ground is ignored, and the effects of the wind turbine receptors and down conductors on the electric fields are disregarded, the problem of finding the electric field along a wind turbine blade admits an analytical solution. The solution procedure is straightforward and similar to calculations of the electric field due to a charged lines and rods (Tipler & Mosca, 2007; Uman, 2001).

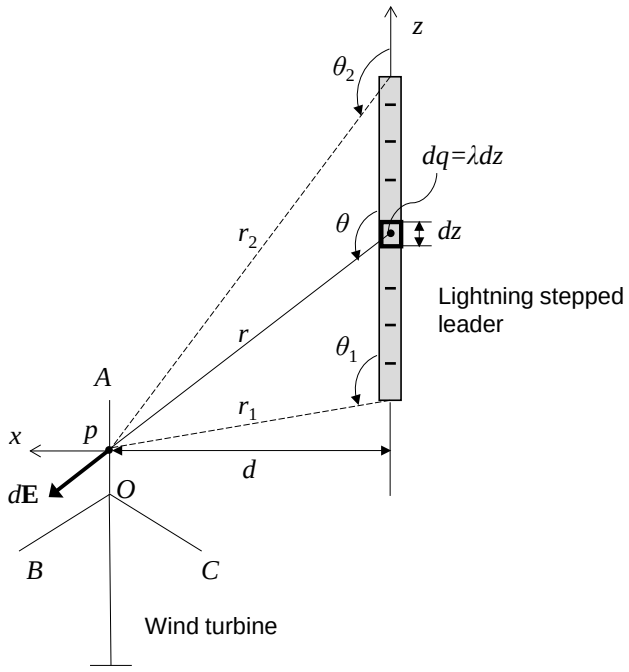

Figure 3. 10: Electric field calculation at point *p* of the blade *OA* due to a uniformly charged lightning stepped leader.

In accordance with the problem formulation described in Section 3.7.1, the leader is represented by a vertical line charge. The charge density is assumed to be uniform

$$\lambda = \frac{Q_l}{L}. \tag{3-10}$$

Here λ is the line charge density (in C/m); $Q_l(\eta) = \int_0^L \lambda(\eta) d\eta$ is the total charge (in C) of the lightning stepped leader with a non-uniform charge density (3-8); and *L* is the length of the lightning stepped leader (in m). The electric field due to the line charge is calculated using Coulomb's law based on the assumption that the field due to an infinitesimal line charge element *dq* is the same as the field due to a point charge.

Therefore, the electric field at an arbitrary point *p* of the blade *OA* due to the charge *dq* within *dz* can be calculated as

$$dE = \frac{kdq}{r^2} = \frac{k\lambda dz}{r^2} = \frac{k\lambda d\theta}{d}, \tag{3-11}$$

where *r* is the distance from charge *dq* to the point *p* at the blade, k=9·10^9 N·m^2·C^{-2} is Coulomb's constant, and $d=r\cdot\sin\theta$ is the lightning striking distance, which is equal to the rolling sphere radius (3-2). The *x*- and *z*-components of the electric field *E* from all the charge in the leader are

$$\begin{aligned} E_x &= \int_{\theta_1}^{\theta_2} \sin\theta \frac{k\lambda d\theta}{d} = -\frac{k\lambda}{d}(\cos\theta_2 - \cos\theta_1), \\ E_z &= \int_{\theta_1}^{\theta_2} \cos\theta \frac{k\lambda d\theta}{d} = \frac{k\lambda}{d}(\sin\theta_2 - \sin\theta_1). \end{aligned} \tag{3-12}$$

The magnitude (i.e., strength) of the electric field from all the charge in the leader is

$$|E| = \sqrt{E_x^2 + E_z^2} = \frac{2k\lambda}{d}\sin\frac{\theta_2 - \theta_1}{2}. \tag{3-13}$$

Here $|E|$ denotes the magnitude of the electric field (in V/m).

3.7.3 Finite Element Analysis of the Electric Fields Due to a Lightning Stepped Leader

In this section, finite element analysis (FEA) of the electric field in a wind turbine blade due to a lightning stepped leader is conducted. The problem formulated in Section 3.7.1 is solved using the COMSOL Multiphysics® finite element analysis software. The FEA enables us to account for the effects of the non-uniform charge density distribution and finite ground that were not included in the analytical model considered in Section 3.7.2.

3.7.3.1 Implementation in COMSOL Multiphysics®

The computational domain is a 3D parallelepiped containing a cutout in the shape of a wind turbine as shown in Figure 3. 11. The dimensions of the cutout are determined by the dimensions of the wind turbine. Wind turbine blades are assumed to be beams of square cross section, 2.5 m by 2.5 m. The computational domain represents the air between a cloud and the ground. The length and width of the parallelepiped are 4,000 m. The depth is $L + z_0$, where L=3,750 m is the length of the lightning stepped leader, z_0 = 250 m is the distance from the tip of the leader to the ground. The lightning stepped leader is assumed to be a vertical cylindrical channel of length L=3,750 m and of radius R_l=5 m. The radius is chosen as in (Lewke, 2007). The cylindrical leader channel is centrally placed in the 3D parallelepiped. Volume charge density $\rho_v = \lambda/\pi R_l^2$, where λ is the line charge density, is applied to the leader channel. Both uniform (3-10) and non-uniform (3-8) charge density distributions on the leader channel are considered. The lightning striking distance, d, as shown in Figure 3. 9, is calculated using the rolling sphere radius (3-2).

As for boundary conditions, cloud voltage, V, is applied to the top surface of the parallelepiped. Ground potential is applied to the bottom surface of the parallelepiped and at the part of the domain boundary corresponding to the surface of the cutout (i.e. exterior

surface of the wind turbine). In such a way, we account for the effects of multiple receptors and down conductors in the wind turbine on the electric field outside of the wind turbine. Open boundary conditions are assumed at all four vertical sides of the parallelepiped.

The present study is focused on estimating the electric fields along blades *OA*, *OB*, and *OC* induced by the lightning stepped leader. The analysis is conducted only for the defined domain (i.e. a 3D parallelepiped containing a cutout in the shape of a wind turbine). The domain (including the leader) is considered as an "air material" defined in the COMSOL Material Library. The domain is meshed with 815,112 free tetrahedral elements. The average duration of each simulation is 128 seconds on a 4-core laptop PC.

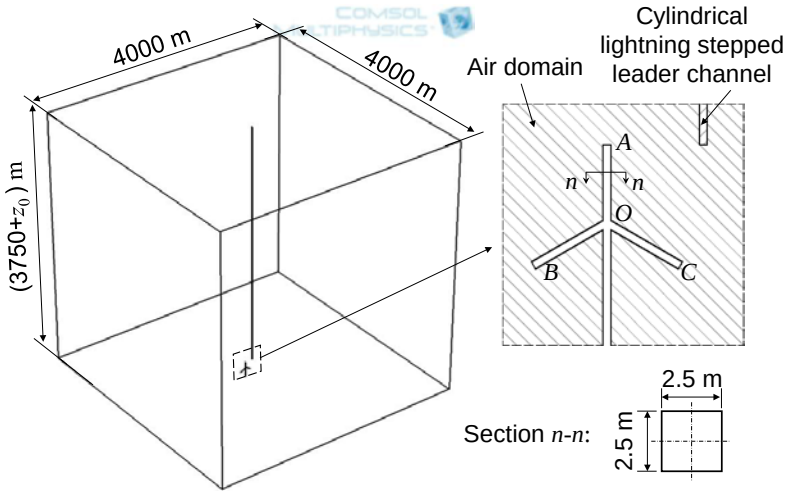

Figure 3. 11: Problem setup in COMSOL.

3.7.3.2 FEA results for the case of the uniform charge density

The lightning stepped leader with the uniform charge density is considered. FEA is conducted for five different cases, when the ground is set at (i) the infinity ($z_0=\infty$); (ii)

250 m below the leader tip (z_0=250 m), which corresponds to the real ground; and three intermediate cases: (iii) z_0=650 m, (iv) z_0=1250 m, and (v) z_0=3250 m. In all cases considered in Section 3.7.3.2, the effects of the wind turbine receptors and down conductors are ignored to facilitate comparisons with the analytical model (3-13). The total charge within the leader is determined by integrating (3-8) along the leader, where I_{peak}=200 A corresponds to the lightning protection level LPL I. The FEA results for the case where the ground is set at the infinity (z_0=∞) are compared with the analytical model predictions (3-13) and are used for verification purposes.

Figure 3. 12 shows the calculated magnitude of the electric field along the blade *OA* for five different cases. As one can see, good agreement exists between the analytical model prediction and FEA results for the case when ground is set at infinity, z_0=∞. It is also shown that in the case of the real ground, z_0=250 m, the magnitude of the electric field is considerably higher than for the case when the ground is set at the infinity, z_0=∞.

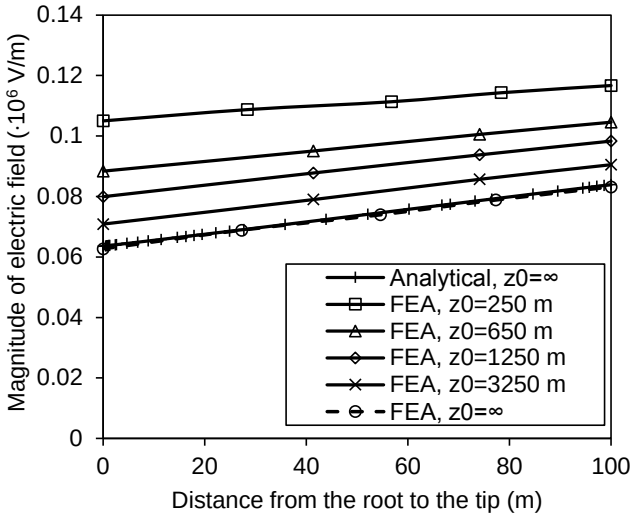

Figure 3. 12: The magnitude of the electric field along blade *OA* due to a leader with a uniform charge density, LPL I (I_{peak}=200 kA): effect of the distance from the leader tip to the ground.

3.7.3.3 FEA results for the case of the non-uniform charge density

Next, FEA was performed to calculate electric fields along the wind turbine blades *OA*, *OB*, and *OC* (see Figure 3. 10) due to a lightning stepped leader with a non-uniform charge density distribution (3-8). The cloud voltage is taken as V=10 kV/m.

Next, a lightning stepped leader with a non-uniform charge density distribution (3-8) is considered and FEA is performed to calculate electric fields along the wind turbine blades *OA*, *OB*, and *OC*, as shown in Figure 3. 11. In this section, two cases are analyzed. In the first case (hereinafter case 1), the effects of the wind turbine receptors and down conductors are ignored, whereas in the second case (hereinafter case 2), the effects of the wind turbine receptors and down conductors are taken into account by applying ground potential at the wind turbine exterior surface (i.e. tower and blade surfaces).The electric fields obtained from the two cases are compared. The cloud voltage is taken as V=40 MV (Becerra, 2008).

FEA results for case 1, in which the effects of the wind turbine receptors and down conductors are ignored, are shown in Table 3. 3 and Figure 3. 13, Figure 3. 14, and Figure 3. 15. Table 3. 3 shows the magnitudes of the electric fields at blade tips for case 1. Figure 3. 13 shows the magnitudes of the electric fields along blades *OA*, *OB*, and *OC* at LPL I for case 1. It can be seen that despite two times difference in the peak currents corresponding to LPL III and LPL I (see Table 3. 1), the difference in the electric fields at the tip of the blade *OA* is only about 4%. Such an insignificant difference can be explained by checking equation (3-2) for the lightning strike distance. As one can see, the higher peak current is associated with the larger lightning strike distance. At the same time, the electric field strength decays with an increase in the lightning strike distance (see, e.g., (3-13)). Therefore, an increase in the lightning strike distance counterbalances an increase in the peak current. Figure 3. 14 shows the magnitudes of the electric fields, and Figure 3. 15 shows the electric potentials at blade *OC* for three LPL levels for case 1.

Table 3. 3: The magnitude of the electric field at the wind turbine blade tips and the stepped leader tip using COMSOL for case 1. (Non-uniform charged lightning stepped leader, z_0=250 m).

LPL	Peak Current, I_{peak} (kA)	Magnitude of the Electric Field (V/m)			
		Blade *OA* Tip	Blade *OB* Tip	Blade *OC* Tip	Lightning Stepped Leader Tip
I	200	$1.99 \cdot 10^5$	$1.28 \cdot 10^5$	$2.08 \cdot 10^5$	$1.46 \cdot 10^6$
II	150	$1.96 \cdot 10^5$	$1.10 \cdot 10^5$	$1.76 \cdot 10^5$	$1.09 \cdot 10^6$
III	100	$1.92 \cdot 10^5$	$8.49 \cdot 10^4$	$1.30 \cdot 10^5$	$7.28 \cdot 10^5$

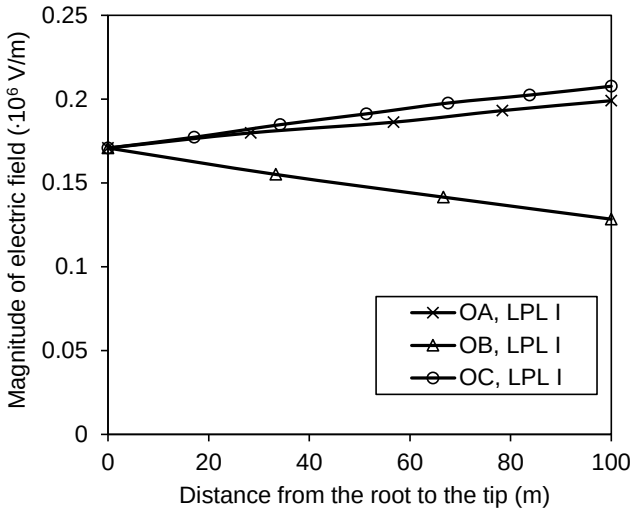

Figure 3. 13: The magnitude of the electric field at blades *OA*, *OB*, *OC*, LPL I for case 1.

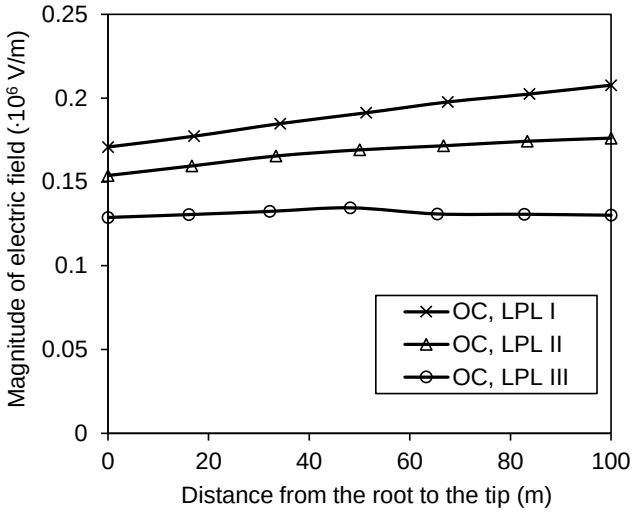

Figure 3. 14: The magnitude of the electric field along blades *OC* for different LPL levels for case 1.

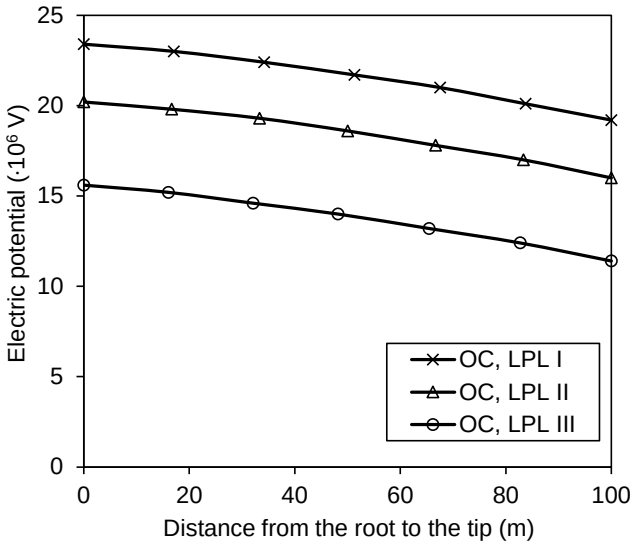

Figure 3. 15: Electric potential along blade *OC* for different LPL levels for case 1.

FEA results for case 2, in which the effects of the wind turbine receptors and down conductors are taken into account in the analysis, are shown in Table 3. 4, Figure 3. 16, Figure 3. 17, and Figure 3. 18. Figure 3. 16 shows the magnitudes of the electric fields along blades *OA, OB,* and *OC* at LPL I for case 2. It can be seen that the electric field at blade *OA* is generally larger than that at blades *OB* and *OC*. When compared to those obtained from case 1, the electric fields obtained from case 2 are generally around one order of the magnitude higher. Figure 3. 17 shows the magnitudes of the electric fields at blade *OA* for three LPL levels for case 2. Close examination of the electric fields at LPL I and LPL II reveals that along blade *OA*, the electric field at LPL I is higher than the electric field at LPL II except for the small region near the tip of blade *OA*. This can be further seen in Table 3. 4, where the magnitudes of the electric fields at the tips of the blades are shown. Similar to case 1, in spite of the higher peak current corresponding to LPL I, at the tip of blade *OA*, the magnitude of the electric field corresponding to LPL I is considerably lower than the magnitude of the electric field corresponding to LPL II. Lastly, Figure 3. 18 shows a contour plot of the electric field magnitude distribution in the vicinity of the wind turbine at LPL III for case 2. It is evident that the application of the ground potential boundary condition at the wind turbine exterior surface (i.e., receptors and down conductors) led to a significant increase in the magnitude of the predicted electric fields. Therefore omitting the effects of receptors and down conductors will lead to a significant underestimation of electric fields along the wind turbine blades and thus lead to incorrect estimations of dielectric breakdown in the GFRP wind turbine blades.

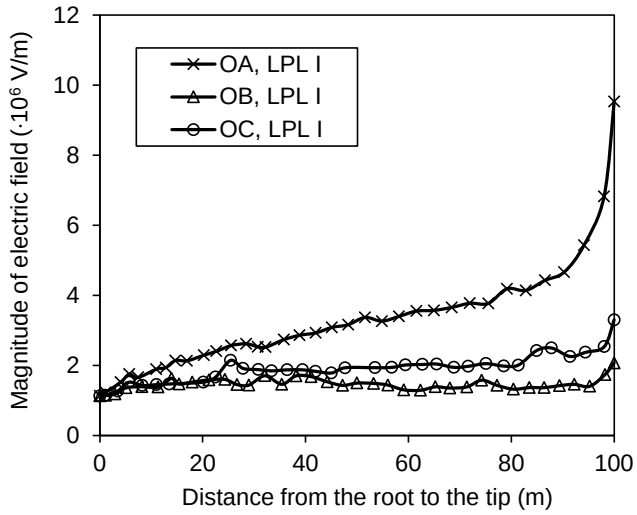

Figure 3. 16: The magnitude of the electric field at blades *OA*, *OB*, *OC*, LPL I for case 2.

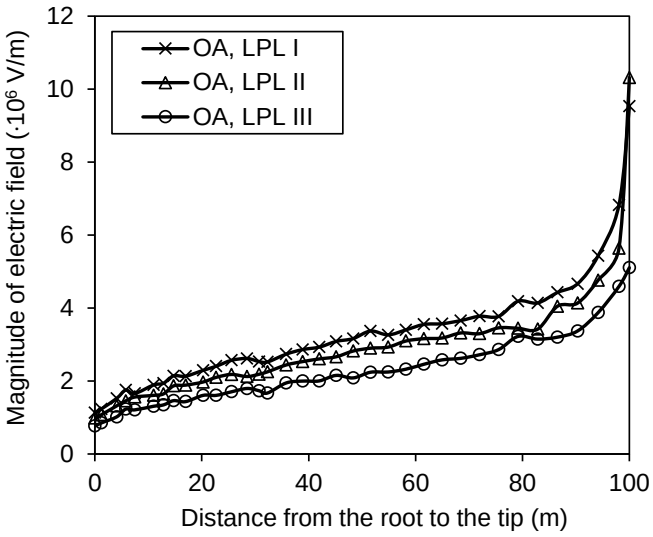

Figure 3. 17: The magnitude of the electric field along blade *OA* for different LPL levels for case 2.

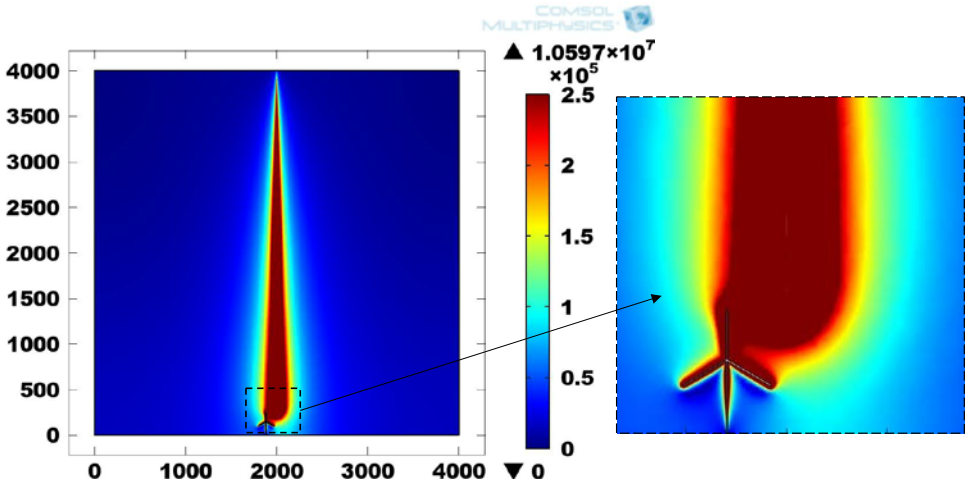

Figure 3. 18: Electric field magnitude distribution in the vicinity of the wind turbine at LPL III for case 2.

Table 3. 4: The magnitude of the electric field at the wind turbine blade tips and the stepped leader tip using COMSOL for case 2. (Non-uniform charged lightning stepped leader, z_0=250 m).

LPL	Peak Current, I_{peak} (kA)	Magnitude of the Electric Field (V/m)			
		Blade *OA* Tip	Blade *OB* Tip	Blade *OC* Tip	Lightning Stepped Leader Tip
I	200	$9.53 \cdot 10^6$	$2.07 \cdot 10^6$	$3.30 \cdot 10^6$	$1.99 \cdot 10^7$
II	150	$1.03 \cdot 10^7$	$1.58 \cdot 10^6$	$2.81 \cdot 10^6$	$1.52 \cdot 10^7$
III	100	$5.10 \cdot 10^6$	$1.30 \cdot 10^6$	$1.66 \cdot 10^6$	$1.04 \cdot 10^7$

3.7.4 Dielectric Breakdown Assessment in a Non-Conductive Composite Wind Turbine Blade

Madsen et al. (2006) conducted an extensive experimental study to determine the dielectric breakdown strength of the glass-fiber-reinforced polymer-matrix (GFRP) composite laminates used in the wind turbine blades (Madsen et al., 2006). Based on the analysis of the experimental data, he suggested the following empirical relationship between the dielectric breakdown strength and the thickness of the GFRP composite laminate (Madsen et al., 2006):

$$E_b = c_1 \cdot \frac{1}{t} + c_2, \tag{3-14}$$

where E_b is the average breakdown field strength of the composite laminate (in V/m), t is the thickness of the laminate (in m), $c_1 = 5.3 \cdot 10^4$ and c_2 is a constant related to the surface tracking resistance of the laminated composites and $3.0 \cdot 10^6 < c_2 < 9.0 \cdot 10^6$. Comparisons between experimental data (Madsen et al., 2006) and predictions obtained using equation (3-14), where $c_2 = 8.0 \cdot 10^6$, are shown in Figure 3. 19. As one can see, a good agreement exists. Therefore, equation (3-14) with parameters $c_1 = 5.3 \cdot 10^4$ and $c_2 = 8.0 \cdot 10^6$ is used in the present study to estimate the dielectric breakdown strength of the Sandia 100-meter All-glass Baseline Wind Turbine Blade (SNL 100-00) (Griffith & Ashwill, 2011). Planform of the blade is shown in Figure 3. 20 and Figure 3. 21.

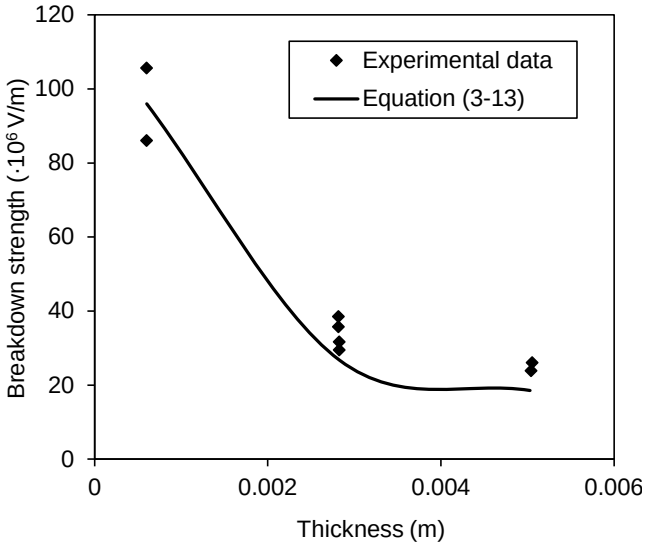

Figure 3. 19: Dielectric breakdown strength of the glass-fiber-reinforced composite laminate.

The root buildup and spar cap of the blade are made of GFRP composites. The other parts of the blade are made of sandwich panels with foam core and GFRP composite facesheets. The experimental data on the dielectric breakdown strength of the sandwich composites is not available, so only the root buildup and spar cap sections are included in the analysis. Moreover, the blade is divided into 34 sections along the spanwise direction. Thicknesses of the root buildup and spar cap at various sections along the spanwise direction are shown in Table 3. 5. Dielectric breakdown strengths of the root buildup and spar cap along the spanwise direction are shown in Figure 3. 19. They are compared to the magnitudes of the electric fields along blade *OA* obtained using FEA (electric fields obtained from case 1 and case 2 in Section 3.7.3.3) and shown in Figure 3. 13 (case 1) and Figure 3. 16 (case 2). Recall that the effects of receptors and down conductors are ignored in case 1 but are taken into account in case 2. The neglect of considering the effects of receptors and down conductors has led to a significant under-prediction of electric fields along the wind turbine blades. The corresponding safety

factors at LPL I, i.e. ratios of the dielectric breakdown strength to the magnitude of the electric field, are shown in Figure 3. 23 (case 1) and Figure 3. 24 (case 2). As one can see, the safety factor along the root buildup is larger than five even for case 2, for which the predicted electric fields are one order of magnitude higher than those predicted in case 1. Therefore, the root buildup design is generally conservative against the dielectric breakdown. As for the spar cap, the safety factor at the tip of blade *OA* is 55.39 for case 1 at the most severe LPL I and is 1.52 for case 2. It is evident that the effects of receptors and down conductors need to be taken into account during the analysis to achieve a conservative estimation of dielectric breakdown. The low safety factor 1.52 indicates that the tip of blade *OA* has the highest risk of experiencing dielectric breakdown. Recall that electric fields along blades *OB* and *OC* are weaker than along blade *OA*. Overall, blade *OA* is the most vulnerable to dielectric breakdown.

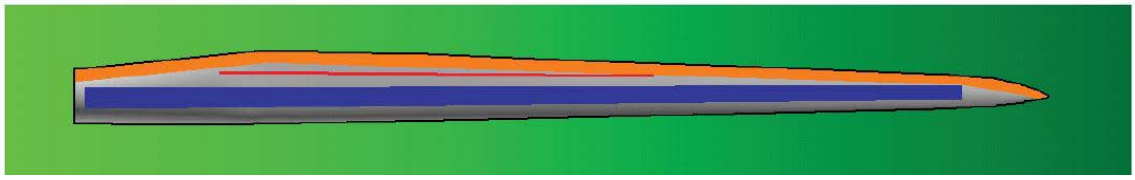

Figure 3. 20: Planform of Sandia 100-m baseline blade with laminated designations (Blue: spar cap, Orange: trailing edge reinforcement, Red: additional shear web).

Source: Griffith & Ashwill (2011). Sandia National Laboratories, SAND2011-3779.

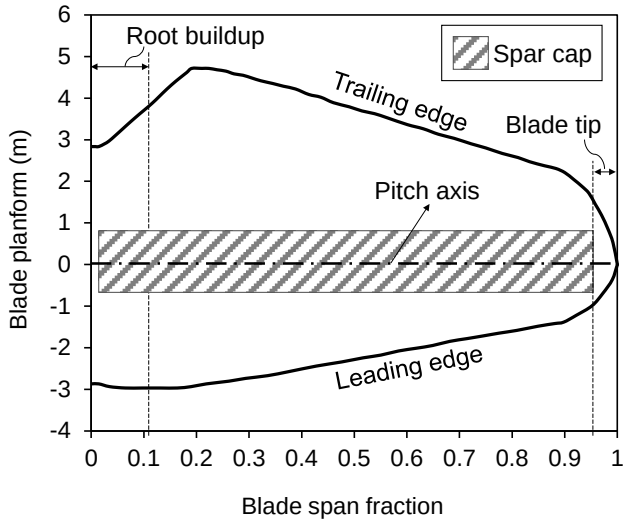

Figure 3. 21: Sandia 100-meter all-glass baseline wind turbine blade (SNL 100-00) planform.

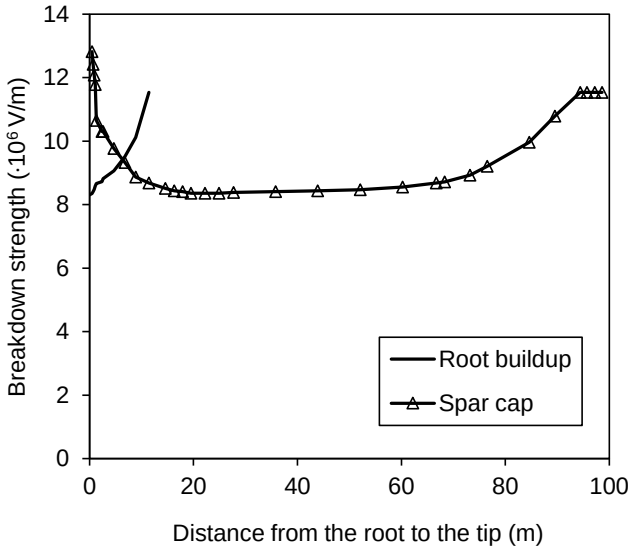

Figure 3. 22: Dielectric breakdown strength of the Sandia 100-meter all-glass baseline wind turbine blade (SNL 100-00) at both root buildup region and spar cap region. Distance at 0 denotes the blade root, distance at 100 m denotes the blade tip.

Table 3. 5: Composite laminate thickness at various sections of the wind turbine blade (Griffith & Ashwill, 2011).

Section Number	Blade Span Fraction	Overall Thickness (mm)	
		Root Buildup	Spar Cap
1	0.000	170	
2	0.005	150	1
3	0.007	130	2
4	0.009	110	3
5	0.011	90	4
6	0.013	80	10
7	0.024	73	13
8	0.026	65	13
9	0.047	50	20
10	0.068	35	30
11	0.089	25	51
12	0.114	15	68
13	0.146		94
14	0.163		111
15	0.179		119
16	0.195		136
17	0.222		136
18	0.249		136
19	0.277		128
20	0.358		119
21	0.439		111
22	0.521		102
23	0.602		85
24	0.667		68
25	0.683		64
26	0.732		47
27	0.765		34
28	0.846		17
29	0.895		9
30	0.944		5
31	0.957		5
32	0.972		5
33	0.986		5
34	1.000		

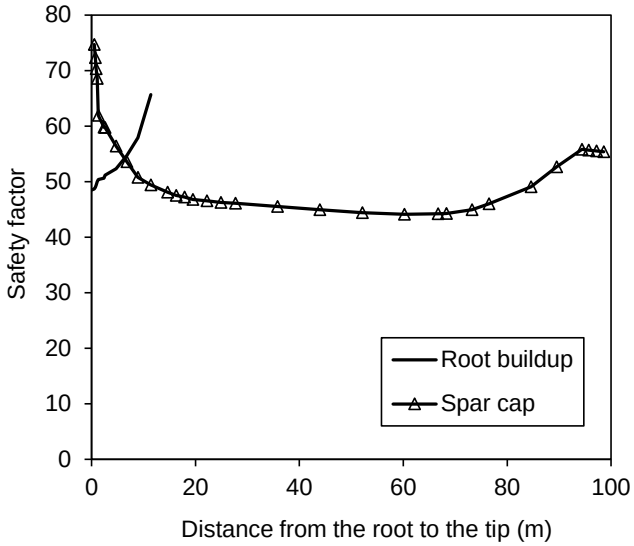

Figure 3. 23: Safety factor (ratio between estimated dielectric breakdown strength and electric field predicted from case 1 in Section 3.7.3.3) at LPL I for wind turbine blade *OC* root buildup region and spar cap region.

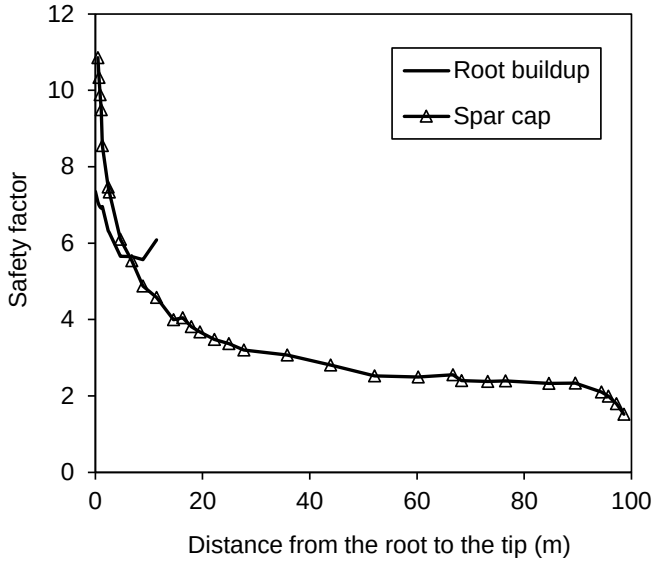

Figure 3. 24: Safety factor (ratio between estimated dielectric breakdown strength and electric field predicted from case 2 in Section 3.7.3.3) at LPL I for wind turbine blade *OC* root buildup region and spar cap region.

It is worth mentioning that the dielectric breakdown strength of composites may deteriorate during the service lifetime of the wind turbine blades due to the presence of moisture, defect accumulation, etc. Although experimental data specific to the composite wind turbine blades are not available, laboratory studies of the glass-reinforced composites may be useful to assess the extent of deterioration in properties. For instance, experimental results reported Morgan et al. (2009) indicate that Cyanate Ester/S2 glass composite retains 90% of its dielectric strength after six-month exposure to 99% humidity. Hong et al. (2009) observed a significant reduction in the breakdown strength in the specimens with 1.5% water content (the specimens were immersed in water until their weight increased by 1.5%). The dielectric strength measured in the specimens containing 1.5% of water was 20 kV/mm compared to 60 kV/mm for the dry specimens. Figure 3. 24 shows that if the breakdown strength is reduced three times, the safety factor at the tip region of the spar cap of blade *OA* (90~100 m from the blade root) falls below one at LPL I and at LPL II. Therefore, dielectric breakdown and severe structural damage are likely to occur. Although investigation of the deterioration effects on the dielectric breakdown strength is beyond the scope of this study, the results obtained in this work suggest that the tip region of Sandia 100-meter All-glass Baseline Wind Turbine Blade (SNL 100-00) is the most vulnerable to dielectric breakdown.

It should be mentioned that if dielectric breakdown does not occur in the composite laminated blades, lightning attachments will come as a direct heat injection into the surface of the non-conductive blades. The direct heat injection can produce a considerable damage that is manifested by thermal ablation, internal explosion, delamination, etc. For instance, experimental studies (Feraboli et al., 2009; Hirano et al., 2010; Li et al., 2015) suggest that an internal explosion occurs from interlaminar pressure buildup owing to the formation of pyrolysis gases. The pyrolysis gases are formed in the process of the interlaminar resin decomposition caused by the direct heat injection.

As a part of damage prediction due to lightning-induced heat injection, a heat transfer problem needs to be solved (Y.Wang & Zhupanska, 2015). A heat transfer problem formulation for non-conductive structures (prior to the dielectric breakdown) is different from the one for conductive structures (once the dielectric breakdown occurred). In the conductive structures, a heat transfer equation has to be solved simultaneously with electrodynamics equations to determine the distribution of the electric current and associated Joule heat densities. The direct heat injection into a structure from the lightning channel will still be a part of the heat transfer problem in the case of the conductive structure. In any case, careful analysis of the lightning-induced electric fields is essential for formulation of the physics-based thermo-mechanical damage models and is critical for development of damage tolerant composite blade designs.

CHAPTER 4
CHARACTERIZATION OF LIGHTNING-CURRENT-INDUCED HEAT FLUX

4.1 Lightning Current Waveform

Laboratory studies of the lightning strike use standard test waveforms that reproduce the significant effects of the natural environment. The standardized lightning strike electric current waveforms are described in the MIL-STD-464 standard (MIL-464-A, 1997) and the SAE ARP 5412 standard (SAE-ARP-5412A, 2005). A typical lightning waveform contains four components and is shown in Figure 2. 1.

The electric current for component A during the initial lightning stroke is much higher than for components B and C. Component C is the so-called continuing component, and component D represents a typical restrike. A detailed waveform of pulsed lightning current component A is also described in IEC-60060-1 (IEC-60060-1, 2010) and is shown in Figure 4. 1.

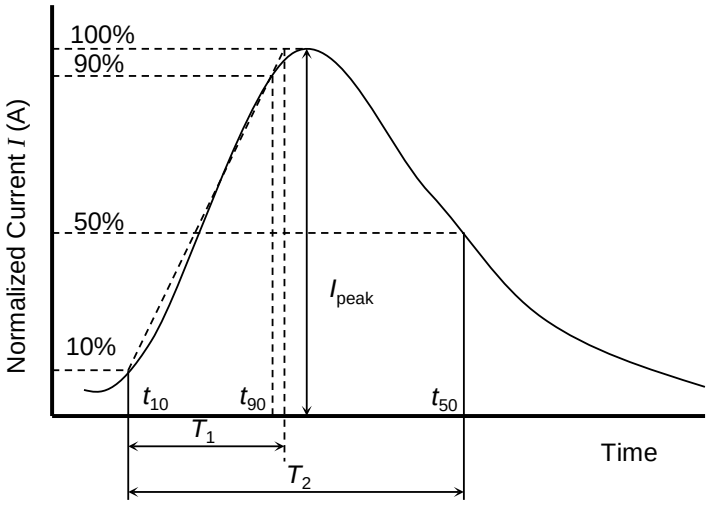

Figure 4. 1: Waveform for component A according to IEC-60060.

The waveform curve is governed by three input parameters, I_{peak}, T_1, and T_2. I_{peak} is the peak value for the lightning strike incidence during the initial strike, T_1 is the front time, and T_2 is the time to half value. IEC-60060-1 also lists time interval requirements that the waveform curve should meet (IEC-60060-1, 2010):

$$T_1 = \frac{t_{90} - t_{10}}{0.8}, \qquad T_2 = t_{50} - \frac{9t_{10} - t_{90}}{8}, \tag{4-1}$$

where t_{10}, t_{90}, and t_{50} are moments when its electric current value reaches 10, 90, and 50 percent of the peak value.

A double exponential expression is used to model the waveform for component A as suggested by the MIL-STD-464 standard (MIL-464-A, 1997):

$$I(t) = I_0\left(e^{-at} - e^{-bt}\right). \tag{4-2}$$

In this work, a waveform with (i.e., one of the three standard damped-oscillating current waveforms as specified by IEC-60060-1) is used. Based on equations (4-1) and (4-2), the explicit expression for this waveform is written in the form

$$I(t) = 1.5 I_{peak} \left(e^{-7.3 \cdot 10^4 t} - e^{-6.3 \cdot 10^5 t} \right), \tag{4-3}$$

where I_{peak} is the peak current for the lightning waveform component A, electric current $I(t)$ is measured in A, and time t is in seconds.

Plooster (Plooster, 1971a) suggested a simpler waveform that allows independent variation in the peak current, rise time, and decay constant:

$$I(t) = \begin{cases} I_{peak} \dfrac{t}{t_m}, & t < t_m, \\ I_{peak} \exp\left[-k \left(t - t_m \right) \right], & t > t_m, \end{cases} \tag{4-4}$$

where t_m is defined as a rise time to separate the linear increasing current portion and exponentially decay current portion, and k is the decay constant. In this work, the simplified expression (4-4) is utilized to describe the lightning waveform component A. Since the front time $T_1 = 4 \cdot 10^{-6}$ s is very close to the rise time t_m, the rise time is assumed to be $t_m = T_1 = 4 \cdot 10^{-6}$ s. The peak current is taken as $I_{peak} = 100,000$ A. The decay coefficient $k = 7 \cdot 10^4$ s^{-1} in equation (4-4) was chosen to fit the double exponential expression for the electric current (4-3). A comparison between the original double exponential current waveform (4-3) and the discretized two portion current waveform (4-4) is shown in Figure 4. 2.

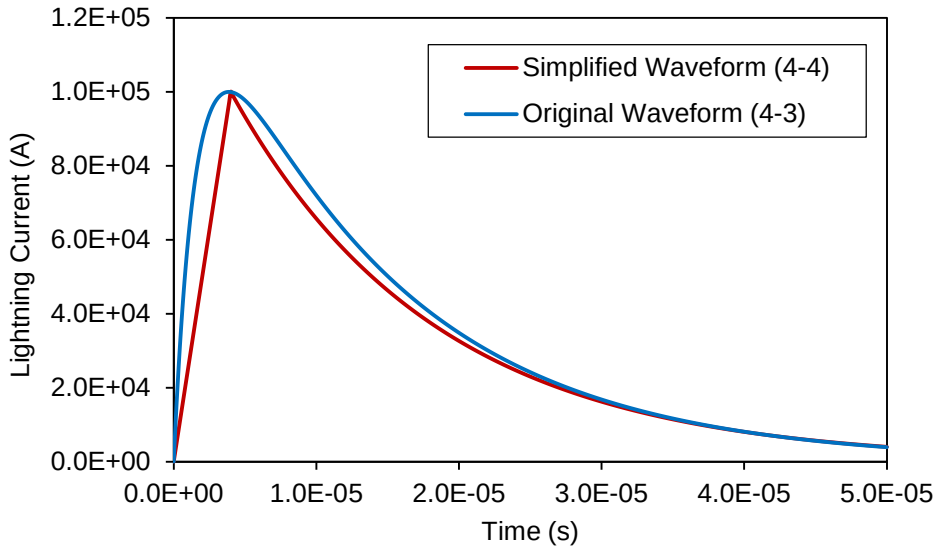

Figure 4. 2: Comparison between the simplified current waveform (4-4) and original double exponential waveform (4-3).

Note that the values for t_m and k parameters used in this work are different from those used by Plooster (Plooster, 1971a) because a different double exponential waveform was fitted in this work than in Plooster's work (Plooster, 1971a).

In the remaining parts of this paper, equation (4-4) will be used to describe the electric waveform for the lightning current component A.

4.2 Lightning Channel Radius Expansion

Lightning current flows in a narrow cylindrical plasma channel whose size depends on the current waveform, pressure, density, etc. One of the first models

describing dependence of the channel radius on the current was presented by Braginskii (Braginskii, 1958):

$$R(t) = \alpha \rho_0^{-1/6} \left[I(t) \right]^{1/3} t^{1/2}, \tag{4-5}$$

where $R(t)$ is the channel radius (in meters) that expands in time, α is a constant; $\alpha = 0.294$, ρ_0 is the air density at atmosphere pressure, $\rho_0 = 1.29$ kg/m^3; $I(t)$ is an instant current in amperes (the current is presumed to increase linearly with time) as is shown in Eq. (4-4); and t is time in seconds. Braginskii's model is based on the so-called "strong-shock" approximation that implies that the channel pressure is much greater than the ambient pressure. This limits the application of expression (4-5) to the early stages of the discharge. Expression (4-5) was numerically validated at component A peak currents by Plooster (Plooster, 1971a). Recently, Cooray and Rahman (Cooray & Rahman, 2005) suggested using a different constant α, namely $\alpha = 0.102$. They noticed that this new constant gives channel radii that are in better agreement with experimental data than those predicted by Braginskii's original model. At the same time, (4-5) is not suitable for estimation of the channel radius during the decaying part of component A waveform. The experimental and numerical results (Hill, 1971; Paxton et al., 1986; Plooster, 1971a) indicate that continuous expansion of the lightning channel occurs during the decaying part of component A, while expression (4-5) predicts a reduction in the channel radius as the electric current decays. To overcome this shortcoming of Braginskii's model, we suggest using the peak current I_{peak} instead of the instant current $I(t)$ together with $\alpha = 0.102$ in expression (4-5) to describe lightning channel radius expansion during component A:

$$R(t) = 0.097 I_{peak}^{1/3} t^{1/2}. \tag{4-6}$$

Comparisons of the channel radius obtained using (4-6) with numerical results of Hill, Paxton, and Plooster (Hill, 1971; Paxton et al., 1986; Plooster, 1971a) are shown in Figure 4. 3. In all models $I_{peak} = 20,000$ A. As one can see, the results obtained using expression (4-6) are consistent with other models. The model developed in Paxton's paper (Paxton et al., 1986) is essentially a generalization of Plooster's gas dynamic model (Plooster, 1971a) for lightning plasma channel. The two are different in the treatment of radiative transport. Plooster's constant density result stands for the case when the air density in the lightning channel is assumed to be equal to the surrounding atmosphere, while the constant pressure case assumes that the pressures are equal. Hill's model (Hill, 1971) is regarded as less accurate (Rakov & Uman, 1998). Detailed comparisons between numerical results obtained using different gas dynamic models including lightning channel radius expansion, temperature, and pressure can be found in Hill's paper (Hill, 1990).

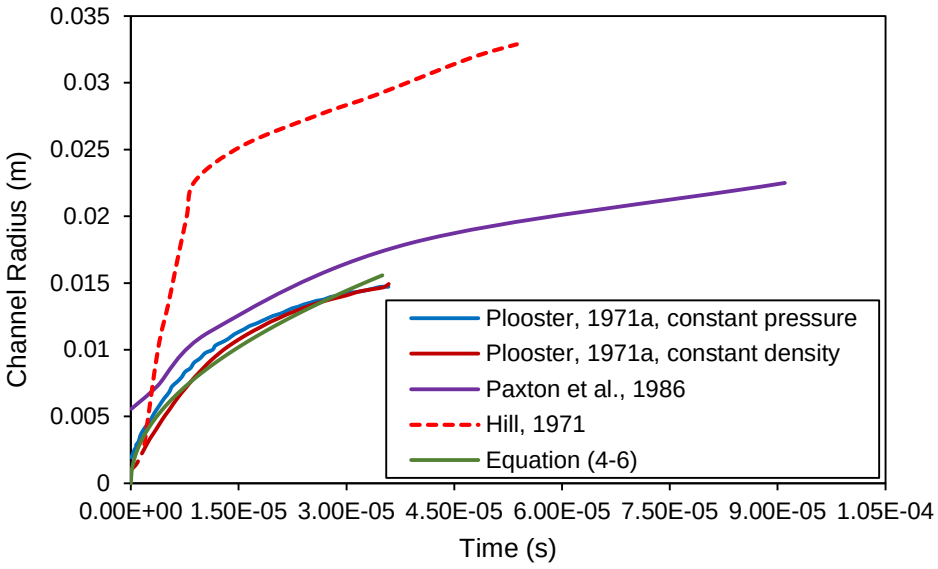

Figure 4. 3: Variation of the lightning channel radius with time: comparisons between different models.

Note that in the previously published studies on lightning-induced damage. Ogasawara et al. (2010) and F. S. Wang et al. (2014) used a pulsed lightning electric current with a concentrated point current, and Abdelal & Murphy (2014) and Muñoz et al. (2014) used a pulsed lightning electric current with a fixed lightning channel radius that was chosen arbitrarily or based on the analysis of the experimentally observed damage. In the present work, the initial pulsed current part of the lightning return stroke is included in the analysis, enabling calculation of the radius of the lightning channel based on the peak and duration of the initial pulsed current.

4.3 Lightning Current Density Spatial Distribution

Experimental measurements (Nestor, 1962; Perera, Rahman, Fernando, Liyanage, & Cooray, 2012; Manabu Tanaka, Terasaki, & Ushio, 2002; Tsai & Eagar, 1985) and numerical models on the electric arcs (Gonzalez, Lago, Freton, Masquere, & Franceries, 2005; Lowke & Tanaka, 2006; M. Tanaka et al., 2010) indicate that the electric arc current density $J(r)$ has a non-uniform Gaussian-like spatial profile with a maximum value at the center of the channel, $J_{max}(t)= J(r,t)|_{r=0}$. Therefore, the lightning arc current density distribution within the circular lightning channel is expected to have the form:

$$J(r,t) = J_{\max}(t)e^{-cr^2}, \qquad r \le R(t). \tag{4-7}$$

where c is a constant, r is the radial coordinate (m), $R(t)$ is the lightning channel radius (m) at time t, and $I(t)$ is the instant lightning electric current (A) at time t.

The analysis of the experimental heat flux distribution (Nestor, 1962; Perera et al., 2012; Manabu Tanaka et al., 2002; Tsai & Eagar, 1985) also suggests that the current density at r=0.55R is equal to about 10% of its maximum value at the center of the channel, $Q(r,t)|_{r=0.55R(t)}$=0.1$Q(r,t)|_{r=0}$. Using this relationship, constant c can be determined:

$$c = -\frac{\ln(0.1)}{(0.55 \cdot R(t))^2}. \tag{4-8}$$

In addition, the integral of the current density over the circular area equals the total current of the lightning channel:

$$\int_0^{2\pi}\int_0^{R(t)} rJ(r,t)drd\theta = I(t). \tag{4-9}$$

Substituting equation (4-7) into equation (4-9), the maximum current density $J_{max}(t)$ in the center of the lightning channel can be obtained as:

$$J_{\max}(t) = \frac{I(t)}{\int_0^{2\pi}\int_0^{R(t)} re^{-cr^2}drd\theta}. \tag{4-10}$$

Therefore, the final form for lightning current density distribution can be obtained by substituting $J_{max}(t)$ (equation (4-10)) and constant c (equation (4-8)) into equation (4-7):

$$J(r,t) = \frac{I(t)}{\int_0^{2\pi}\int_0^{R(t)} re^{-cr^2}drd\theta} e^{r^2\ln(0.1)/(0.55\cdot R(t))^2}, \qquad r \le R(t). \tag{4-11}$$

In our earlier paper (Y. Wang & Zhupanska, 2015), we calculated the maximum current density $J_{max}(t)$ directly using electric current divided by the circular area. The constant c was obtained by assuming that 10% of its maximum current density is located at r=R(t). The lightning current density distribution that we obtained in our earlier work is:

$$J(r,t) = \frac{I(t)}{\pi R^2(t)} e^{r^2\ln(0.1)/R^2(t)}, \qquad r \le R(t). \tag{4-12}$$

Figure 4. 4 shows the current density profiles on the anode structures due to electric arc discharges with constant current $I(t)$=200 A and constant radius $R(t)$=0.01 m. Nestor and Tsai obtained the current density profiles using experimental methods (Nestor, 1962; Tsai & Eagar, 1985). Lowke and Chemartin obtained the current density profiles using numerical methods based on magnetohydrodynamics method (MHD) (Chemartin et al., 2011; Lowke & Tanaka, 2006). The current density profiles calculated using obtained equation (4-11) and equation (4-12) are compared to the experimental and numerical results. It can be seen in Figure 4. 4 that our current model, equation (4-11), shows an approximate agreement with both the experimental and numerical results, while our old model, equation (4-12), underestimates the current density profile. The current density profile calculated using the old model is around 7 times lower than the experimental results.

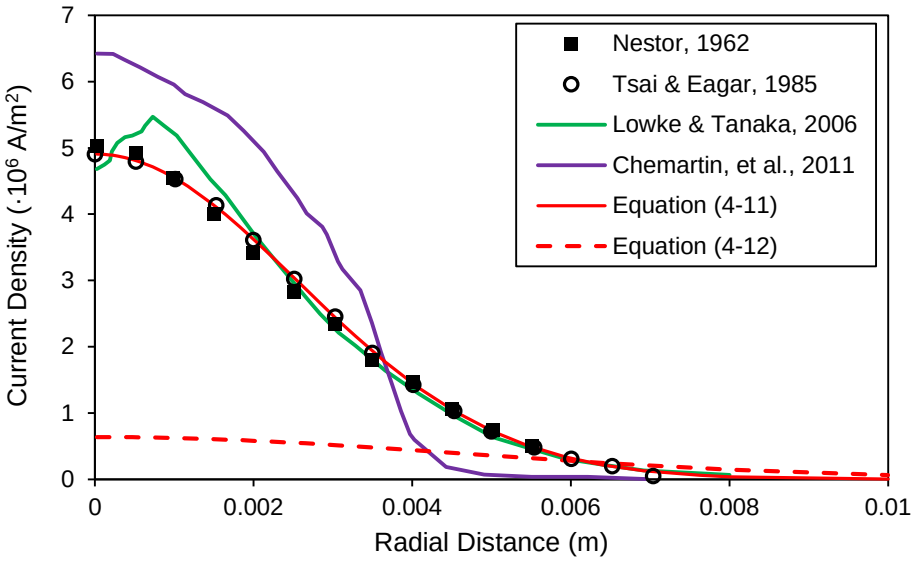

Figure 4. 4: Current density profiles on the anode structures due to an electric arc discharge with constant current of 200 A and constant radius of 0.01 m from experimental tests, numerical calculations, and our developed models.

4.4 Lightning-Current-Induced Heat Flux Distribution

As for the heat flux, the amount of heat flux injected into the structure surface from the lightning arc channel depends on the polarity of the materials. In the case of the anode structure, it can be expressed by (Chemartin et al., 2011; Fan & Kovacevic, 2004; Lago, Gonzalez, Freton, & Gleizes, 2004):

$$Q = J\left(U_a + \Phi_{mat} + \frac{5k_b}{2\varepsilon}\left(T_{arc} - T_{anode}\right)\right), \tag{4-13}$$

where J is the electric current density (A/m^2), U_a is the anodic voltage drop (V), Φ_{mat} is the work function of the material (V), T_{arc} is the arc temperature, T_{anode} is the anode temperature, k_b is Boltzmann's constant, and ε is the electron electrical charge. The third term in the big parentheses denotes the electron kinetic energy change in the anode structure. The anodic voltage drop U_a and the material work function Φ_{mat} are around 4 to 5 V, and the electron kinetic energy change in the anode structure is considered negligible for high electric current arcs (Chemartin et al., 2012). Therefore, the heat flux can be written as:

$$Q \approx 10J. \tag{4-14}$$

Equation (4-14) shows that the lightning-current-induced heat flux is approximately linear to the lightning current density, which also follows a Gaussian-like spatial distribution. The Gaussian-like heat flux spatial distribution of the electric arcs has also been found in experimental tests and numerical models (Chemartin et al., 2011; Lowke & Tanaka, 2006; Nestor, 1962; Perera et al., 2012; Manabu Tanaka et al., 2002;

Tsai & Eagar, 1985). Substituting equation (4-11) into equation (4-14), the non-uniform distribution of the lightning-current-induced heat flux can be obtained as:

$$Q = \frac{10I(t)}{\int_0^{2\pi}\int_0^{R(t)} re^{-cr^2} dr d\theta} e^{r^2 \ln(0.1)/(0.55\cdot R(t))^2}, \qquad r \le R(t). \tag{4-15}$$

Figure 4. 5 shows the comparison of heat flux on the anode structure using our model and from other numerical prediction (shown by the curve) with experimental results (shown by points) for an electric arc with a constant current of 150 A and a constant radius of 0.01 m. As one can see, the heat flux profile predicted using our model shows an approximate agreement with the experimental results and Lowke's numerical prediction (Lewke et al., 2007). Similarly, the heat flux on the anode structure for an electric arc with constant current of 200 A and constant radius of 0.01 m predicted using our model is compared with other numerical predictions and experimental data in Figure 4. 6. We can see, except for Lago's numerical prediction (Lago et al., 2004), that the heat flux predicted using our model shows an approximate agreement with the experimental result, Lowke and Gonzalez's numerical prediction (Lewke et al., 2007; Gonzalez et al., 2005). Lago's model (Lago et al., 2004) overestimated the heat flux. The maximum heat flux in the center of the electric arc predicted by Lago et al. (2004) is almost 2 times higher than the experimental results.

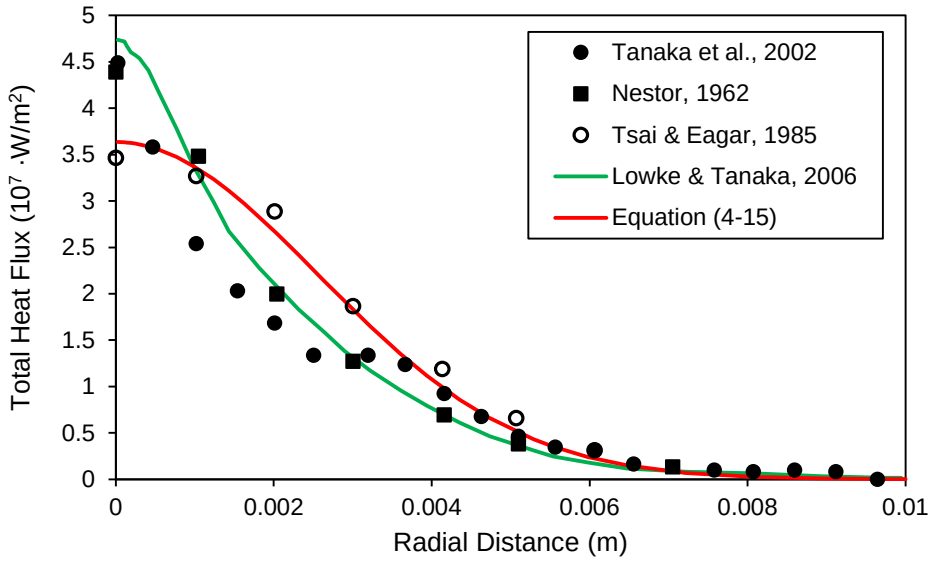

Figure 4. 5: Total heat flux on the anode structures due to an electric arc discharge with constant current of 150 A and constant radius of 0.01 m from experimental tests, other numerical models, and our model.

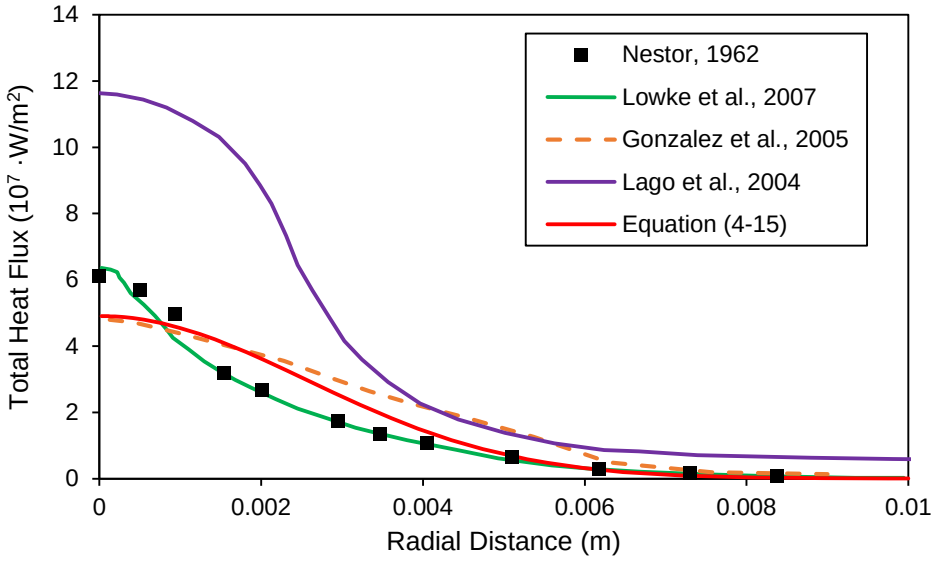

Figure 4. 6: Total heat flux on the anode structures due to an electric arc discharge with constant current of 200 A and constant radius of 0.01 m from experimental tests, other numerical models, and our model.

It is worth noting that some other previous studies (Lago et al., 2006; Manabu Tanaka, Terasaki, Ushio, & Lowke, 2003) also used non-uniform heat flux to model the thermal interaction between the electric arcs and the anode structures. However, these studies have limitations. Lago et al. (2006) numerically modeled the thermal interaction between an electric arc (800 A) with non-uniform heat flux distribution and a carbon fiber epoxy composite structure. However, the maximum temperature obtained in his model (Lago et al., 2006) is around 900 °C, which is much lower than the sublimation temperature of the carbon fiber (~3300 °C). The situation at high temperature when fiber undergoes sublimation is not modeled, because his model is not sufficient to handle the material phase transition. Furthermore, Tanaka et al. (2003) modeled the thermal interaction between a free-burning argon arc with non-uniform heat flux distribution and the stainless steel SUS304. However, their model allowed the temperature to keep increasing without removing the melted materials immediately when the temperature reached the melting point. The moving boundary condition, which is essential in solving the problems with material phase transition is not considered (Tanaka et al., 2003).

CHAPTER 5
MODELING OF LIGHTNING-INDUCED THERMAL ABLATION DAMAGE IN GFRP COMPOSITES AND ITS APPLICATION TO WIND TURBINE BLADES

5.1 Problem Formulation

In an electrically conductive material (e.g., a CFRP composite), Joule heating is produced when the energy dissipated by the lightning current, which is conducted through the material, is converted into the thermal energy. The governing heat transfer equation in this case has the form

$$\nabla \cdot \left(\mathbf{k}(T) \nabla T \right) = -Q_J + c(T) \rho \frac{\partial T}{\partial t}. \tag{5-1}$$

where $\mathbf{k}(T)$ is the temperature-dependent thermal conductivity tensor; Q_J is internal Joule heating generation; $c(T)$ is the temperature-dependent specific heat of the composite structure; ρ is density; T is field temperature, and t is time.

For electrically non-conductive composites (e.g., GFRP composites), the lightning current comes as a direct heat flux injection, the lightning current is conducted via the weakly charged surface of the structure or jumps between contaminated (moisture, dirty, salt, etc.) areas of the surface. Therefore, Joule heating is not generated in the structure and the corresponding heat transfer equation has the form:

$$\nabla \cdot \left(\mathbf{k}(T) \nabla T \right) = c(T) \rho \frac{\partial T}{\partial t}. \tag{5-2}$$

It is assumed that the structure is subjected to a lightning strike consisting of the pulsed current (component A) and continuous current waveform (component C), $I(t)$, schematically shown in Figure 5. 1. Lightning current flows in a narrow straight cylindrical plasma channel, the size of which depends on the current waveform, pressure, density, etc. (Borovsky, 1998; Braginskii, 1958; Hill, 1971, 1977, 1990; Paxton et al., 1986; Plooster, 1971a, 1971b). The lightning plasma channel injects heat into the structure with a non-uniform heat flux, $Q(r,t)$, which is a function of electric current waveform $I(t)$ and lightning channel radius $R(t)$. The heat flux is distributed over the circular area bounded by lightning channel radius $R(t)$ (see Figure 5. 2). The analytical expression of the non-uniform heat flux is presented in equation (4-15).

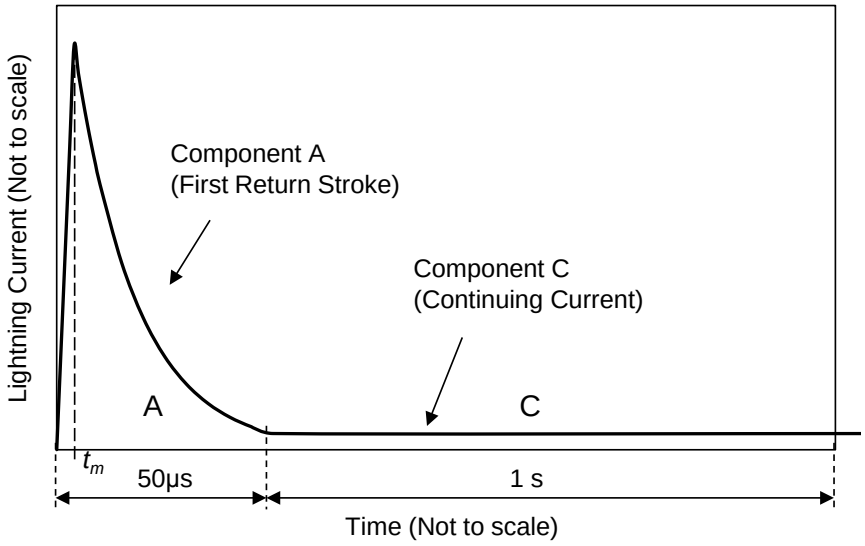

Figure 5. 1: Schematic of lightning current, pulsed current component A, continuous current component C.

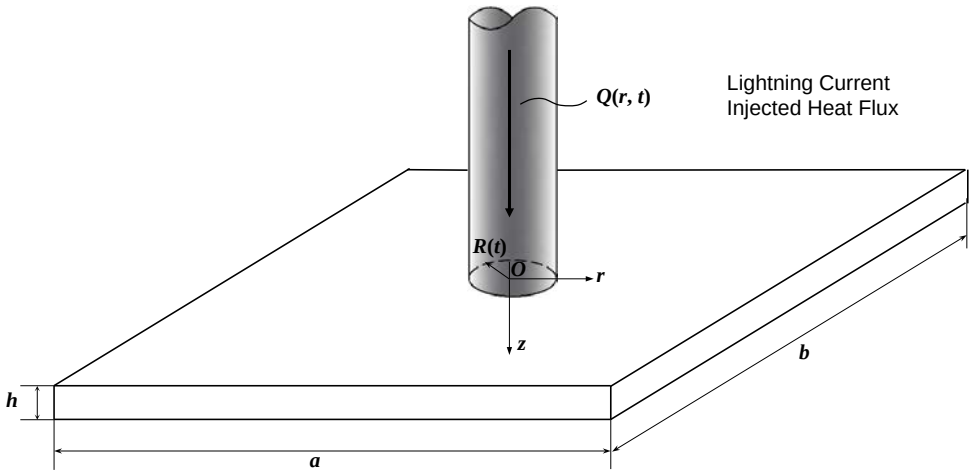

Figure 5. 2: Thermal interaction between a lightning channel and a composite panel.

The radius of the lightning channel expands over time, thus leading to a heat transfer problem with a moving boundary. Therefore, the following boundary conditions exist at the top surface of the anisotropic structure, z=0, subjected to a lightning strike:

$$-k_z(T)\left.\frac{\partial T}{\partial z}\right|_{z=0} = Q(r,t), \qquad r \le R(t), \tag{5-3}$$

where k_z is the thermal conductivity in the through-the-thickness direction. Explicit expressions for the lightning channel radius $R(t)$ and heat flux $Q(r,t)$ are shown in equations (4-6) and (4-15).

A radiation boundary condition is assumed at the parts of the top surface outside the lightning channel:

$$-k_z(T)\left.\frac{\partial T}{\partial z}\right|_{z=0} = \sigma\varepsilon\left(T_\infty^4 - T^4\right), \qquad r > R(t), \tag{5-4}$$

where σ=5.67·10^{-8} W/m^{2}K^4 is the Stefan-Boltzmann constant, ε is the emissivity of the surface (e.g., ε=0.85 for the GFRP composite), and T_∞ is the temperature of the surroundings (T_∞=25 °C). The surfaces, other than the top surface, which is exposed to the lightning strike, are assumed to be held initially at constant temperature T= T_∞.

Lightning-induced heat injection may generate extreme temperatures in the structure and result in material phase transitions. Moreover, since the non-uniform heat flux is applied over a moving circular area, phase boundaries can also move with time. The boundaries of the material phases are not known in advance and have to be determined as a part of the solution. In mathematical terms, this is the so-called Stefan problem (Caldwell & Kwan, 2004).

5.2 Composite Structure

5.2.1 Lightning Attachment on SNL 100-00 Wind Turbine Blade

In this thesis work, a three-dimensional wind turbine composite blade model was created using the Sandia 100-meter all-glass baseline wind turbine blade (SNL 100-00) (Griffith & Ashwill, 2011). It has been reported that the wind turbine blade tip is more susceptible to lightning strike than the remaining parts of the blade (Madsen et al., 2006).

According to Madsen et al.'s study (2006), most of the lightning attachment point (1%~100%) lies within a distance 10 m from the blade tip (see Figure 5. 3). The region far away from the tip region is unlikely (<1%) to be hit by a lightning strike. Figure 5. 3 shows the lightning attachment point distributions collected from the simulation results

developed by Madsen et al. (2006) and three field surveys from real wind farm sites (Horns Reef, Field Survey 2010, and Field Survey 2011). The average of the four distributions is also shown in Figure 5. 3. The figure shows that most of the lightning attachment points (1% ~100%) are located within 10 m from the tip of the wind blade. For regions far away from the wind blade tip (>10 m), the probability of having a lightning attachment is very low (<1%).

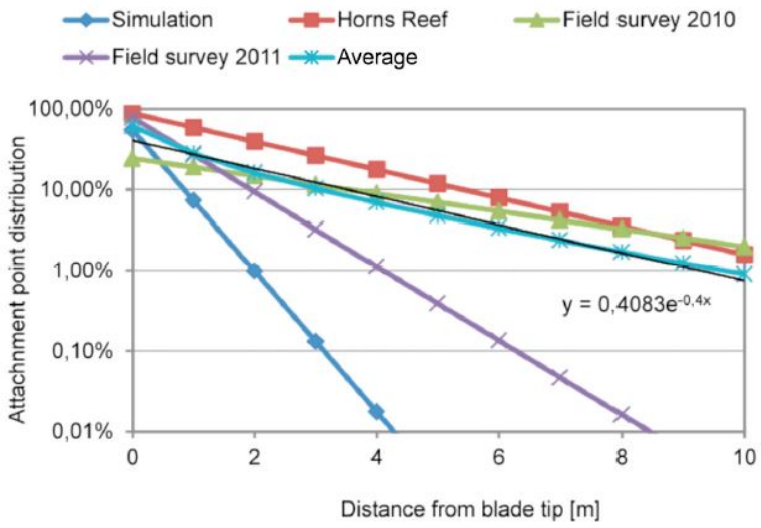

Figure 5. 3: Lightning attachment point distribution versus distance from blade tip.

Source: Madsen et al. (2006). PhD Thesis, Technical University of Denmark.

Therefore, only the tip region top panel of the wind turbine blade was used for the lightning strike study. The tip region is shown in Figure 5. 4 (a), and the lightning strike attachment point is located at the small area on the top surface of the blade tip as shown in Figure 5. 4 (b).

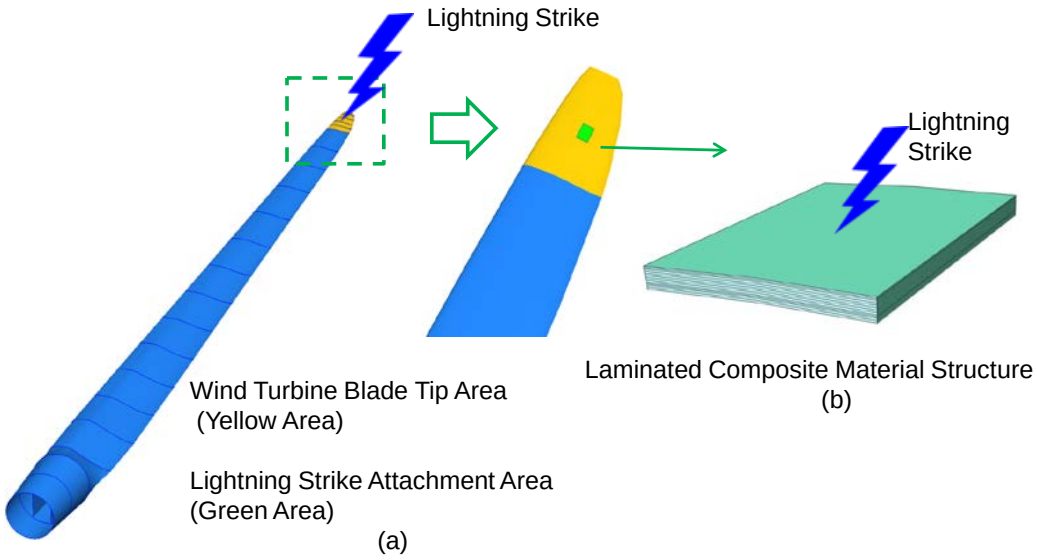

Figure 5. 4: Lightning strike attachment on the wind turbine blade.

5.2.2 Composite Materials and Laminate Schedule at Blade Tip

We consider a non-conductive laminated glass-fiber-reinforce polymer-matrix (GFRP) composite panel representing a tip region top panel of the Sandia 100-meter All-glass Baseline Wind Turbine Blade (SNL 100-00) (Griffith & Ashwill, 2011). The panel is subjected to the lightning current. The panel is non-conductive and the lightning current comes as a direct heat flux injection and without producing joule heat inside the panel.

The laminated GFRP composite panel is 0.12 m long, 0.12 m wide and 0.014 m thick. It consists of two SNL triaxial $[\pm 45]_2[0]_2$ E-glass fiber vinyl ester resin matrix and two VectorPly E-LT 5500 unidirectional $[0]_2$ E-glass fiber vinyl ester resin matrix fabrics placed between the SNL triaxial fabrics. The SNL triaxial fabric is fabricated by stacking one layer of VectorPly E-LT 5500 unidirectional two-ply $[0]_2$ fabric upon two layers of

Knytex DBM 1708 woven biaxial [±45] E-glass fiber vinyl ester resin matrix fabric (Griffith & Ashwill, 2011). The VectorPly fabric has a fiber volume fraction V_f=54% and the SNL triaxial fabric has a fiber volume fraction V_f=44%. Thickness of each unidirectional ply [0] is $1.3 \cdot 10^{-3}$ m and thickness of the biaxial fabric [±45] is $0.9 \cdot 10^{-3}$ m. Table 5. 1 shows laminate layup schedule for the considered composite panel. Note that plies with the same materials properties and orientation are combined in single layers.

Table 5. 1: Laminate composite fabric layups for the blade tip.

Fabric Type	Layer #	Orientation	Thickness (m)
Exterior Triaxial $[\pm 45]_2[0]_2$	Layer 1	$[\pm 45]_2$	$1.8 \cdot 10^{-3}$
	Layer 2	$[0]_2$	$2.6 \cdot 10^{-3}$
Unidirectional $[0]_2$	Layer 3	$[0]_4$	$5.2 \cdot 10^{-3}$
Interior Triaxial $[\pm 45]_2[0]_2$	Layer 4	$[\pm 45]_2$	$1.8 \cdot 10^{-3}$
	Layer 5	$[0]_2$	$2.6 \cdot 10^{-3}$

5.2.3 Thermal and Electrical Properties of E-Glass Fibers and Vinyl Ester Resin

E-glass fiber is a typical product of low-cost general-purpose fiber. As its letter designation “E” indicates, E-glass fiber attains very low electrical conductivity ($\sim 10^{-11}$ $1/\Omega \cdot m$) at ambient temperature. The electrical conductivity of vinyl ester resin is 5 orders lower than E-glass fiber, which makes the glass fiber vinyl ester resin matrix composite nearly nonconductive at ambient temperature. The electrical conductivity, thermal conductivity, and specific heat of both E-glass fiber and vinyl ester resin at ambient temperature are shown in Table 5. 2.

Table 5. 2: Electrical and thermal properties of E-glass fiber and vinyl ester resin at room temperature.

	Electrical Conductivity ($1/\Omega \cdot m$)	Thermal Conductivity ($W/m \cdot K$)	Specific Heat ($J/kg \cdot K$)
E-glass Fiber	$2.5 \cdot 10^{-11}$	1.32	810
Vinyl Ester Resin	$1.0 \cdot 10^{-16}$	0.13	1228

5.2.4 Temperature-dependent Anisotropic Thermal Conductivity

It has been reported that vinyl ester resin starts to decompose at 320-380 °C, and it can be fully decomposed at approximately 525-800 °C (Lua, O'Brien, Key, Wu, & Lattimer, 2006). In addition, it is known that the softening temperature for E-glass is 830-860 °C, and the liquidus temperature for E-glass is 1065-1077 °C (Wallenberger & Bingham, 2010). When the temperature reaches some critical value (~1100 °C) in the glass fiber vinyl ester composite, both the reinforcement phase and matrix residuals undergo sublimation. In order to model a thermal response of the glass-fiber-reinforced polymer-matrix (GFRP) composite over such a wide temperature range, temperature-dependent material properties need to be determined first.

Thermal conductivity of E-glass fiber vinyl ester resin matrix fabric is temperature dependent. Thermal conductivity of the resin, k_m, is temperature dependent, but thermal conductivity of glass fiber, k_f, is assumed to remain fairly constant even at temperatures when resin decomposition takes place (Lua et al., 2006). Thermal conductivity of the resin is determined as

$$k_m = F k_{mv} + (1 - F) k_{md}, \tag{5-5}$$

where k_{mv} is the thermal conductivity of the resin at its virgin state before its decomposition, and k_{md} is the decomposed thermal conductivity of the resin in its charred state. Thermal conductivity of the resin in its virgin state and in its charred state are determined by the experimentally derived empirical relationships (Lua et al., 2006):

$$\begin{aligned} k_{mv} &= 0.13\left[1.0 + 2.088\cdot 10^{-4}\left(T-20\right)\right], \\ k_{md} &= 0.0443\left[1.0 + 1.4298\cdot 10^{-6}\left(T-20\right)^2 + 3.3229\cdot 10^{-3}\left(T-20\right)\right], \end{aligned} \tag{5-6}$$

where temperature T is measured in °C and F is the instantaneous mass fraction of material remaining, defined by

$$F = \left(m - m_d\right)/\left(m_0 - m_d\right). \tag{5-7}$$

Here m is the current instantaneous mass, m_d is the decomposed mass, and m_0 is the initial virgin mass. F is obtained via the thermogravimetric test. In this study, F values are taken from the experimental data reported in the literature (Lua et al., 2006). It should be noted that expressions (5-7) are valid up to a temperature of 900 °C. When temperature exceeds 900 °C, the resin is fully decomposed, and the thermal conductivity of the composite becomes constant (Lua et al., 2006).

The overall anisotropic thermal conductivities of the composites are obtained using the rule of mixture. Figure 5. 5 presents the temperature-dependent thermal conductivity in the fiber direction for the glass fiber fabrics. Temperature-dependent thermal conductivity in the through-the-thickness direction is shown in Figure 5. 6.

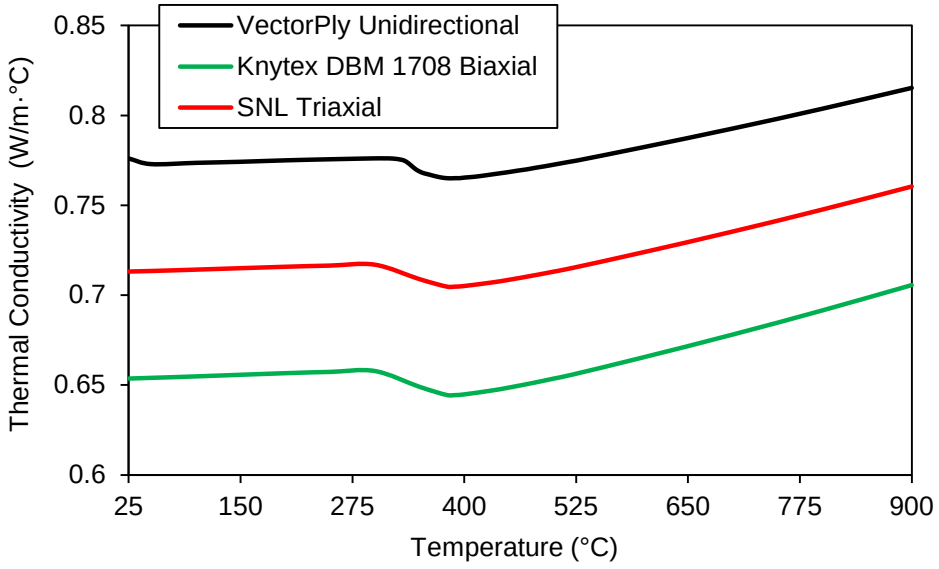

Figure 5. 5: Thermal conductivity in the fiber direction versus temperature for the GFRP composite laminates.

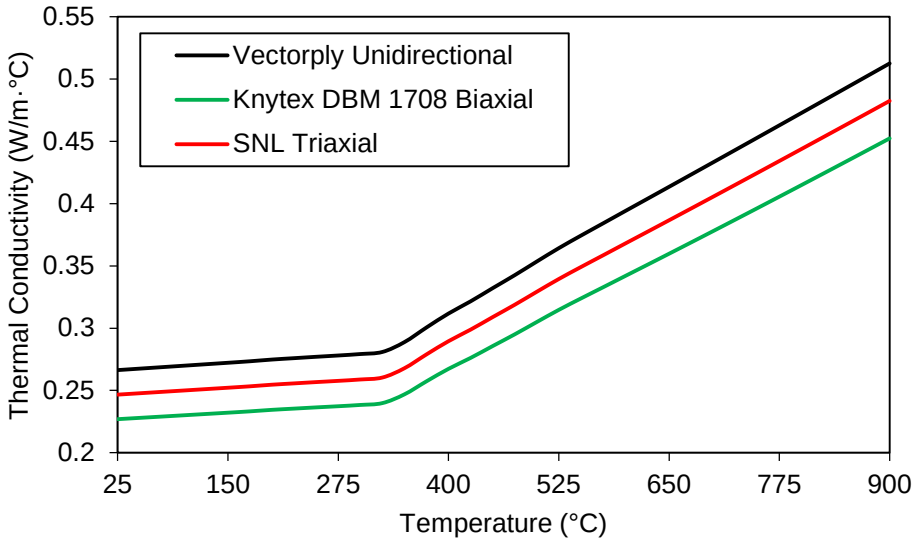

Figure 5. 6: Thermal conductivity in the through-the-thickness direction versus temperature for the GFRP composite laminates.

5.2.5 Temperature-dependent Specific Heat

Specific heat for the composite is calculated as

$$C = \frac{C_f V_f \rho_f + C_m \left(1 - V_f\right) \rho_m}{\rho_{com}}, \tag{5-8}$$

where C is the specific heat of the composite, C_f is the specific heat of the fiber, C_m is the specific heat of the resin, ρ_f is the density of E-glass fiber, ρ_f =2250 kg/m^3, ρ_m is the density of vinyl ester resin, ρ_m =1020 kg/m^3, and ρ is the density of the composite, which is defined by the rule of mixture

$$\rho = V_f \rho_f + \left(1 - V_f\right) \rho_m. \tag{5-9}$$

It is also assumed that the specific heat for E-glass fiber remains constant as temperature increases, but it changes as decomposition of the resin matrix with elevated temperature occurs

$$C_m = F C_{mv} + \left(1 - F\right) C_{md}, \tag{5-10}$$

where F is the instantaneous mass fraction of material remaining, which is defined by equation (5-7), C_{mv} is the specific heat of resin at its virgin state before its decomposition, and C_{md} is the specific heat of the decomposed resin in charred state (Lua et al., 2006):

$$C_{mv} = 1343.0\left[1.0 + 1.14796 \cdot 10^{-4}\left(T - 20\right)\right],$$
$$C_{md} = 1224.93\left[1.0 + 7.2047 \cdot 10^{-4}\left(T - 20\right)\right], \quad (5\text{-}11)$$

where temperature T is measured in °C. Using equations (5-8)-(5-11), the specific heat for the three types of GFRP composite laminates, used in the composite blade, were obtained. The results are shown in Figure 5. 7.

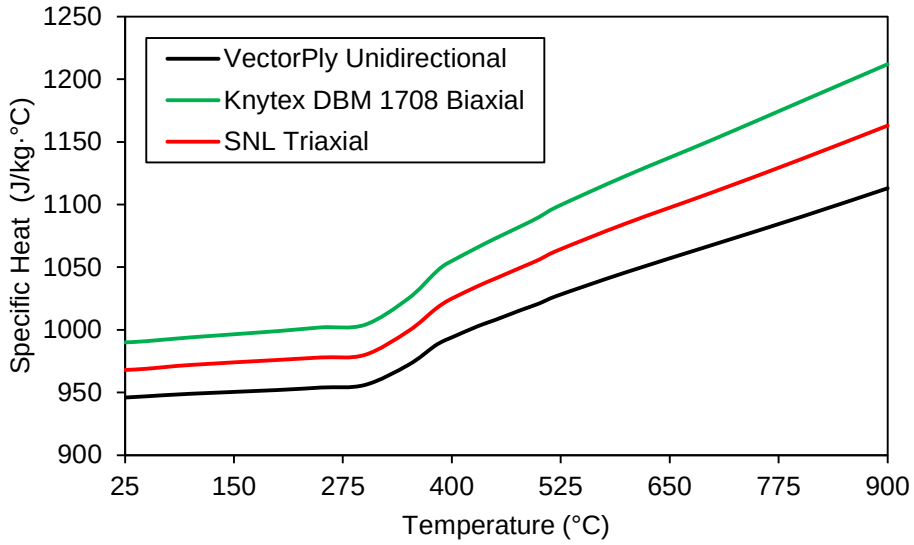

Figure 5. 7: Specific heat versus temperature for the GFRP composite laminates.

5.3 Numerical Treatment in FEA

Finite element analysis (FEA) of the nonlinear heat transfer subjected to a lightning strike is conducted using ABAQUS. The lightning strike heat flux is applied using a developed user-defined subroutine DFLUX, which determines both the lightning arc channel heat flux time and spatial evolution.

It is assumed in this work that when the surface temperature reaches a designated ablation temperature, a sublimation reaction takes place and material is immediately removed (i.e., ablation takes place). There are several approaches used in FEA to model thermal ablation. One of the most common approaches is to delete elements once their temperature reaches the ablation temperature. However, when this approach is used, reapplication of the heat flux boundary after elements are deleted is challenging. Another approach is to introduce virtual latent heat (Ogasawara et al., 2010). In this case, once the temperature of an element reaches the ablation temperature, the tangential stiffness is set to zero to stop the temperature increase. However, this approach is still far from accurate, as introduction of the virtual latent heat prevents the system from absorbing further thermal energy once the ablation temperature is reached. ABAQUS offers an alternative approach that utilizes a user subroutine Umeshmotion and arbitrary Lagrangian-Eulerian (ALE) adaptive mesh technique (Yin et al., 2014; ABAQUS 6.14 Documentation). Umeshmotion enables a user to define the motion of the nodes corresponding to different field values (i.e., temperature in the thermal ablation problem), while ALE allows better mesh deformation.

In this study, two approaches are used and compared. The first approach utilizes an ABAQUS subroutine Umeshmotion and ALE adaptive mesh, which will be designated as the Umeshmotion+ALE method. The second approach is developed based on the traditional element deletion method and will be designated as the element deletion method.

The Umeshmotion subroutine was developed by defining the proper motion of the nodes based on their temperature values under the current time increment. The motion of the nodes under thermal ablation was introduced by Lee (2008). A 2D 4-node planar element is shown in Figure 5. 8; the lightning heat flux is in the -*y* direction, and it is assumed that thermal ablation occurs when a portion of the element domain exceeds the ablation temperature T_{abl}. The motion of the nodes is then defined by moving the upper nodes *N*1 and *N*2, whose temperature exceeds the ablation temperature to the exact receding surface $T=T_{abl}$ (if $T^{N1} > T_{abl}$, $T^{N4} < T_{abl}$ is satisfied). To ensure this condition, a small time increment is desired to avoid the situation when $T^{N1} > T_{abl}$, $T^{N4} > T_{abl}$ (Lee, 2008). The temperature inside a finite element can be interpolated using nodal temperatures and the shape functions of the element. The location of the exact receding surface $T=T_{abl}$ on the $\xi = -1$ edge of the element in the normalized coordinates, η_{abl}, can be calculated by

$$\eta_{abl} = \frac{T^{N1} + T^{N3} - 2T_{abl}}{T^{N1} - T^{N3}}. \tag{5-12}$$

And in the actual coordinate system (x, y), position of the receding surface $T = T_{abl}$ is determined by

$$y_{abl} = \frac{1}{2}\left((1-\eta_{abl}) \cdot y^{N1} + (1+\eta_{abl}) \cdot y^{N4}\right), \tag{5-13}$$

where y^{N1} and y^{N4} are the vertical coordinates of nodes *N*1 and *N*4, respectively. The same node motion calculation is applied at the element edge $\xi = 1$ that is associated with

nodes *N*2 and *N*3. In such a way, the upper nodes *N*1 and *N*2 move to their new positions *N*1’ and *N*2’, which determine position of the receding surface.

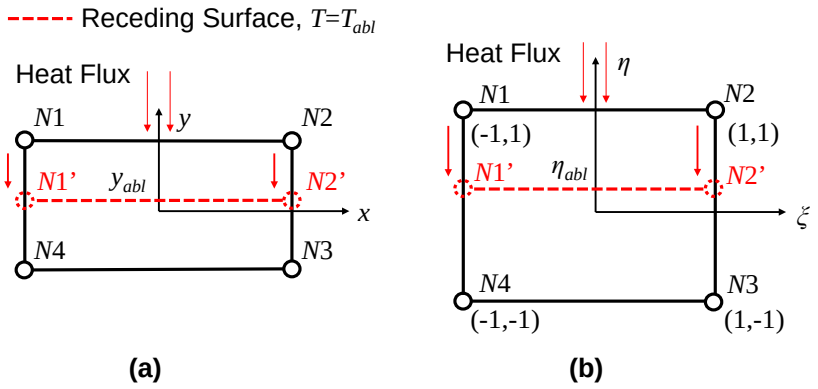

Figure 5. 8: Umeshmotion+ALE method. Motion of the nodes in the 4-node linear planar finite element during thermal ablation: (a) actual coordinates, and (b) normalized coordinates.

If applicable, the Umeshmotion+ALE method is accurate because the heat flux boundary is constrained at the nodes and there is no need to re-apply heat flux boundary condition. However, this method is not applicable for the modeling of ablation in inhomogeneous materials (e.g. laminated composite materials, which are of interest in this study) if thermal ablation penetration depth exceeds the depth of the subsurface homogeneous material domain (i.e. crosses the boundary between two distinct material domains). This is because the mesh in ABAQUS is not allowed to flow from one material domain into another material domain. Therefore, Umeshmotion+ALE method works accurately only if an ablation front is confined within one material domain and does not approach an interface between two distinct material domains. As the ablation front

approaches the interface between two material domains, the computations are aborted due to severe mesh distortion. To overcome this limitation, an element deletion method is developed as a part of the present work.

The following description of the element deletion method is given below for the case of a layered material, in which the in-plane thermal conductivity is much greater than the through-the-thickness thermal conductivity (e.g. fiber-reinforced laminated composites). It is assumed that heat flux is applied to the top surface of a finite element (see Figure 5. 9) and thermal ablation occurs when a portion of the element exceeds the ablation temperature T_{abl}.

Due to the difference in the in-plane and through-the-thickness thermal conductivities, much larger temperature gradients are expected to appear between adjacent vertical nodes $N2$ and $N3$ and $N1$ and $N6$ in the through-the-thickness direction compared to the adjacent horizontal nodes $N1$ and $N2$ and $N3$ and $N6$ in the in-plane direction (see Figure 5. 9(a)). In addition, if the mesh size in the in-plane direction is sufficiently small, the temperature difference between the adjacent horizontal nodes can be neglected, $T^{N1} \approx T^{N2}$, $T^{N3} \approx T^{N}$. Thus, the ablation front will first propagate in the vertical direction and the temperature at the upper nodes $N1$ and $N2$ of element 1 will reach the ablation temperature T_{abl} at some moment of time t_1. As time progresses, the temperature of the upper nodes $N1$ and $N2$ of element 1 will exceed the ablation temperature, $T_{t_1}^{N1,N2} > T_{abl}$ and the receding surface (i.e. ablation front) $T = T_{abl}$ will move somewhere between upper and bottom nodes of element 1. As this happens, the volume of the material above the receding surface should be removed. However, an element cannot be partially removed. Element 1 will stay intact until the receding surface reaches the bottom of element 1, $T_{t_2}^{N3,N6} = T_{abl}$ (see Figure 5. 9(b)). After that, element 1 will be automatically deleted from further computations and the heat flux boundary condition will be re-applied at the upper nodes of the next vertically adjacent element (i.e. element 2 in Figure 5. 9(c)).

This element deletion procedure has been implemented in ABAQUS using a user-defined subroutine. The subroutine monitors nodal temperatures at each time increment and stops computations once an element with bottom nodes temperatures exceeding the ablation temperature is identified. Such element is deleted using Python script. Then, a new heat flux boundary condition boundary is recalculated and analysis is resumed. Figure 5. 10 shows a flow chart of the entire numerical procedure of the element deletion method. The capabilities and effectiveness of the Umeshmotion+ALE and the element deletion methods are compared in the next section.

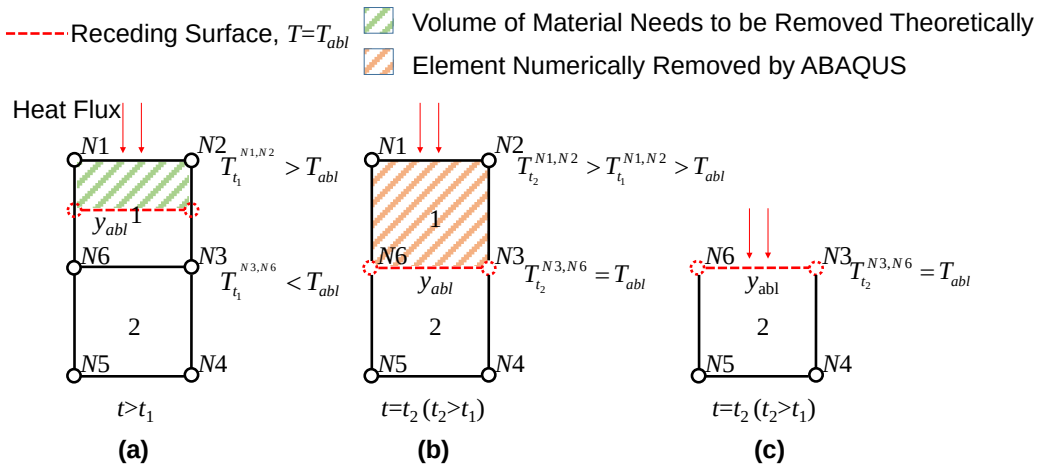

Figure 5. 9: Illustration of the element deletion method.

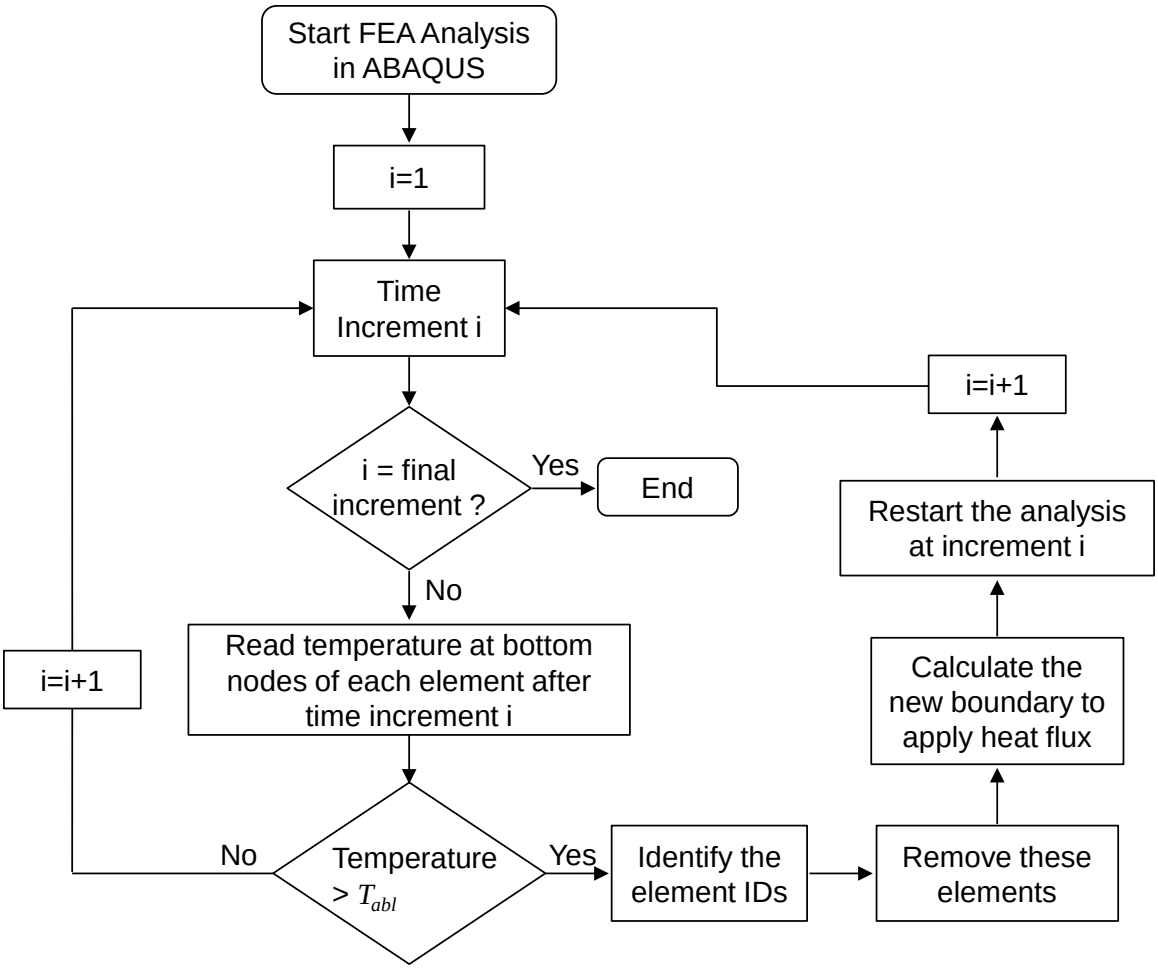

Figure 5. 10: Flow chart of the numerical treatment of element deletion method in ABAQUS.

5.4 Mesh Dependency of Thermal Response in GFRP Composite Structure Due to Short-Duration Pulsed Lightning Current

The finite element analysis (FEA) of heat transfer in a glass-fiber-reinforced polymer-matrix (GFRP) composite structure subjected to a pulsed lightning current may yield mesh-dependent solutions due to the extremely short duration (50~500 μs). It is

therefore critical to select an appropriate mesh size and time increment to avoid mesh-dependent FEA solutions. In this section, the effect of mesh size on the FEA solution is investigated for a heat transfer problem in a solid square cube subjected to a top-surface-loaded uniform heat flux, 1×10^{8} W/m^2, with an extremely short duration, t=500 μs. The four side surfaces and the bottom surface are adiabatic. The side of the square cube is 0.1 mm long. Material properties of the woven biaxial [±45] E-glass fiber vinyl ester resin matrix fabric (described in Section 5.2) are assigned to the current square cube. The time increment of the FEA is fixed as Δt=9.8×10^{-6} s. Five FEA cases are conducted using different mesh sizes Δx (hexahedron cube mesh). The mesh size Δx and the ratio between the time increment and mesh size $\Delta t/\Delta x$ are tabulated in Table 5. 3 for the five cases. During the FEA, the temperature of the cube is allowed to keep increasing without considering thermal ablation. In other words, the Umeshmotion+ALE method and the element deletion method are not used.

Table 5. 3: Mesh size and ratio between time increment and mesh size for the five FEA cases.

Case #	1	2	3	4	5
Δx (m)	1×10^{-5}	8×10^{-6}	5×10^{-6}	3×10^{-6}	2×10^{-6}
$\Delta t/\Delta x$	1	1.23	2	3.3	5

Figure 5. 11 shows the temperature history on the top surface of the GFRP square cube due to the short-duration, high-intensity uniform heat flux obtained from five FEA cases using different mesh sizes (see Table 5. 3). It can be seen that the mesh dependency of the predicted temperature history is quite noticeable when $\Delta t/\Delta x$ is equal to or smaller than 2. However, the mesh dependency becomes negligible when $\Delta t/\Delta x$ is equal to or larger than 3.3. Although a larger value of $\Delta t/\Delta x$ is desired to minimize the mesh

dependency on the predicted temperature fields, at a fixed time increment, a small mesh size Δx would adversely yield a large number of elements, which would result in an unaffordable computational time. Therefore, the $\Delta t/\Delta x$ is controlled between 3 and 4 in the following FEA simulations with the short-duration, high-intensity pulsed lightning current such that the mesh dependency can be minimized without compromising computational cost.

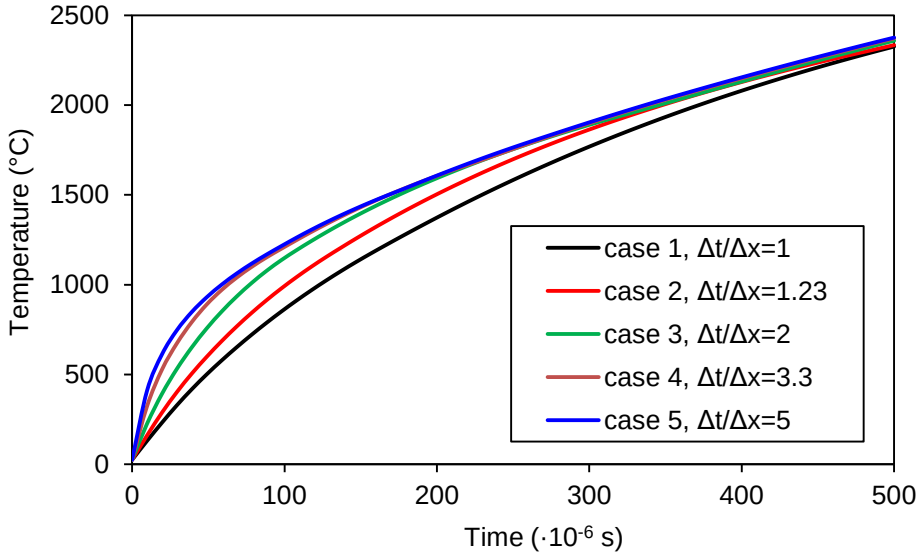

Figure 5. 11: Temperature history on the top surface of the GFRP square cube due to the short-duration, high-intensity uniform heat flux obtained using different mesh sizes.

5.5 Mesh Dependency of Thermal Ablation Predicted Using Element Deletion Method

As described in Section 5.3, a small element size is desired when the element deletion method is used to predict thermal ablation in the composite structure, especially

in the regions of high temperature gradients. In the context of the lightning-strike-induced thermal ablation, that region would be near the lightning strike attachment surface. If the mesh size is not sufficiently small, when the temperature at the bottom nodes reaches the ablation temperature, the temperature at the top node may already far exceed the ablation temperature ($T^{N1}>>T^{N6}$ in Figure 5. 9). In this case, using the element deletion method will lead to an under-prediction of thermal ablation. In this section, thermal ablation is predicted for a 2D square isotropic plate under a uniform heat flux. The side of the 2D square plate is 10 mm long. The thermal conductivity is 6.578×10^{-4} W/m·°C, the density is 1.814×10^{-6} kg/m^3, and the specific heat is 1004.3 J/kg·°C. The uniform heat flux applied to the top edge of the 2D plate is 350 W/m^2 with a duration of 50 μs. The two side edges and one bottom edge are adiabatic. Ablation is assumed to occur immediately at 1100 °C. To investigate the mesh dependency of predicted thermal ablation using the element deletion method, two FEA cases are performed, one with coarse mesh, and the other with fine mesh. The resulting number of elements is 10000 for the FEA case with coarse mesh and 40000 for the FEA case with fine mesh. In addition, the predicted thermal ablations from the two FEA cases using the element deletion method are compared with the predicted thermal ablation using Umeshmotion+ALE method with coarse mesh. Figure 5. 12 shows the comparison of the ablation depth versus time predicted from the two FEA cases using the element deletion method and another FEA case using the Umeshmotion+ALE method. It can be observed that the predicted thermal ablation depth using the element deletion method with fine mesh agrees well with the prediction using the Umeshmotion+ALE method. However, the predicted thermal ablation depth using the element deletion method with coarse mesh is 4.23% lower than the prediction using the element deletion method with fine mesh at the end of the step, and is 6.33% lower than the prediction using the Umeshmotion+ALE method.

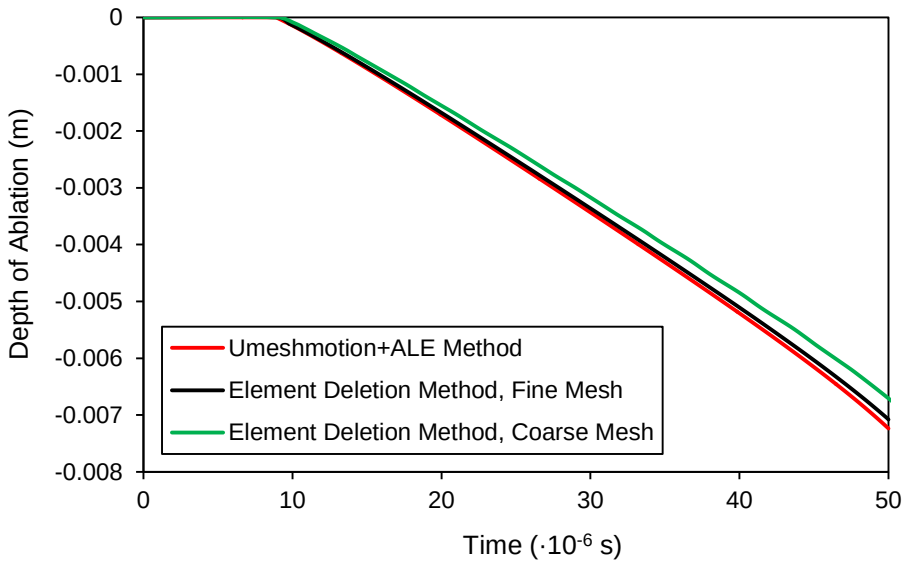

Figure 5. 12: Comparison of ablation depth versus time predicted from two FEA cases using element deletion method with different mesh sizes and another FEA case using Umeshmotion+ALE method.

5.6 FEA Results and Discussions

Three different lightning severity cases that correspond to lightning protection levels, LPL I, LPL II, and LPL III (IEC-61400-24, 2002) are considered in the present work. The specific lightning current waveform parameters for the pulsed and the continuing lightning currents at three LPL levels are shown in Table 5. 4.

Table 5. 4: Lightning current waveform parameters.

Case	Pulsed Lightning Current (Component A)					Continuing Lightning Current (Component C)		
	Peak Current, I_{peak}	Rise Time, t_m	Duration	Decay Constant, k	Action Integral	Constant Current	Duration	Charge Transfer
	(kA)	(μs)	(μs)	(1/μs)	($\cdot 10^6$ A/m^2)	(kA)	(s)	(Coulombs)
LPL I	200	4	50	0.07	0.339	2	0.6	1200
LPL II	150	4	50	0.07	0.191	1.5	0.6	900
LPL III	100	4	50	0.07	0.085	1	0.6	600

Finite element analysis (FEA) was conducted to solve the nonlinear heat transfer problem in the laminated GFRP composite panel described in Section 5.1 subjected to the lightning current corresponding to LPL I, LPL II, and LPL III. To account for the rapid material phase transition due to instant glass fiber sublimation, it was assumed that material was immediately removed once the temperature in the composite material exceeded the sublimation temperature of the glass fiber (1100 °C). Each layer of the laminated GFRP composite panel was modeled as a homogenized anisotropic ply and was meshed using CPE8T element in ABAQUS. The four edges and the bottom surface of the composite panel are adiabatic. The lightning-current-induced heat flux (4-15) is modeled using an ABAQUS user-defined subroutine DFLUX (see APPENDIX A.1), which determines both the temporal and spatial evolution of the lightning-current-induced heat flux on the top surface of the composite panel. In addition, a surface radiation boundary condition (5-4) is applied on the top surface of the composite panel outside the circular lightning channel

The FEA analysis was conducted sequentially from the lowest lightning protection level (LPL III) to the highest lightning protection level (LPL I) using the

Umeshmotion+ALE method as described in Section 5.3. If Umeshmotion+ALE method failed (i.e. the ablation front approached the boundary between Layer 1 $[\pm 45]_2$ and Layer 2 $[0]_2$), the developed element deletion method was used for the failed case and other LPL levels with higher electric current.

First, a computational analysis has been carried out to solve the nonlinear heat transfer in the laminated composite panel due to pulsed lightning current for the three LPL cases. The Umeshmotion+ALE method has been used for this computational analysis, as it is expected that the thermal ablation induced by the short-duration pulsed lightning current is not sufficient to reach the interface between the woven (layer 1) and the unidirectional layer (layer 2). The computational results showed that the thermal ablation in the laminated composite panel due to the pulsed lightning current is insignificant for the three LPL cases. Figure 5. 13 shows the thermal ablation at the center of composite panel starts at $t=1.0\cdot10^{-7}$ s, $t=1.1\cdot10^{-7}$ s and $t=1.2\cdot10^{-7}$ s, respectively for LPL I, II, and III. The maximum ablation depths reach $8.00\cdot10^{-5}$ m, $7.49\cdot10^{-5}$ m, and $6.75\cdot10^{-6}$ m, respectively, for the three LPL cases at the end of the step, at $t=5.0\cdot10^{-5}$ s. The ablation depth at $t=5.0\cdot10^{-5}$ s increased 1.11 times from LPL III to LPL II and 1.19 times from LPL III to LPL I. It is evident that the surface of the composite panel undergoes a rapid thermal ablation during the linear increasing portion of the pulsed lightning current, $t<t_m=4.0\cdot10^{-6}$ s (t_m is the rise time of the pulsed lightning current; see Figure 5. 13). However, after the lightning current reached its peak value, $t>t_m$, the lightning current started to decay exponentially. The significant lightning current drop failed to further ablate the composite panel. In addition, the maximum ablation depth of the laminated composite panel in the case of LPL I reached $8.00\cdot10^{-5}$ m, which is smaller than 1/20 of the thickness of layer 1 ($1.80\cdot10^{-3}$ m), and is far from the interface between the woven (layer 1) and the unidirectional layer (layer 2). As discussed previously, the Umeshmotion+ALE method works accurately when the thermal ablation does not approach the material domain interface. Therefore, in this computational analysis, the

Umeshmotion+ALE method is adequate. Figure 5. 14 illustrated the ablation zone profile in the composite panel. The maximum radius of the thermal ablation zone at the surface of the composite panel reached 0.014 m, 0.012 m, and 0.010 m, respectively, for the cases of LPL I, II, and III. It is worth noting that the maximum radius of the thermal ablation zone at the surface of the laminated composite panel is smaller than the lightning channel radius calculated from equation (4-6). This is due to the Gaussian-like heat flux spatial distribution and the rapid lightning current decaying after it reached its peak value at $t=t_m$.

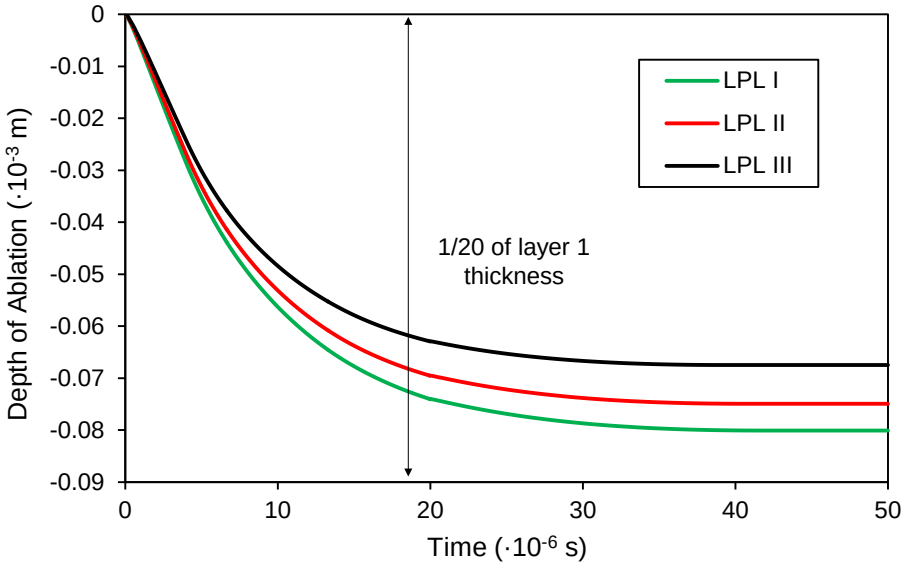

Figure 5. 13: Ablation depth vs. time at $r=0$ of the composite panel due to pulsed lightning current for different LPL levels using the Umeshmotion+ALE method.

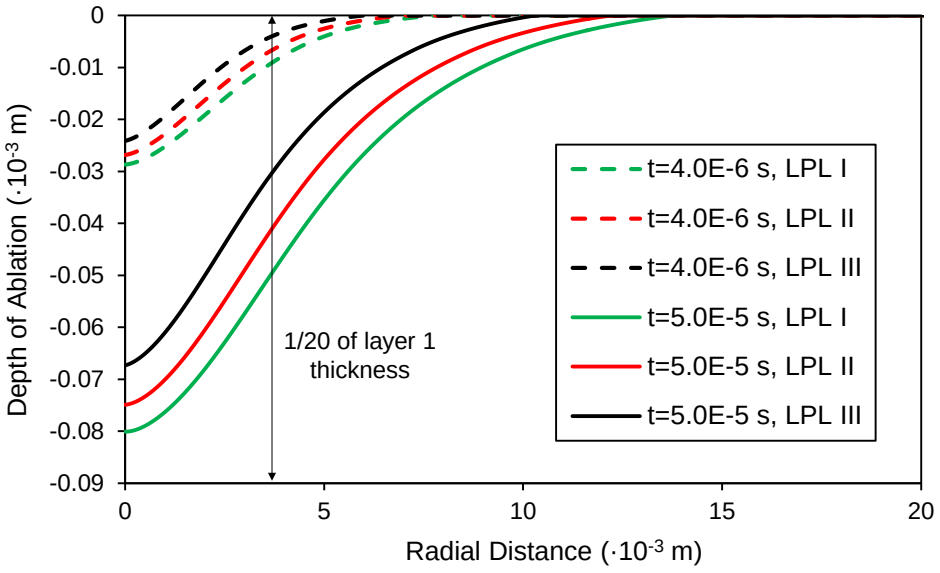

Figure 5. 14: Ablation zone profile of the composite panel due to pulsed lightning current for different LPL levels using the Umeshmotion+ALE method.

In our previous study (Y. Wang & Zhupanska, 2015), we showed that ablation produced by component A is insignificant compared to that produced by component C. Thus, heat transfer analysis of component C can be done independently of component A under the assumption that the radius of the lightning arc channel during component C is equal to the radius of the arc channel at the end of component A.

The FEA heat transfer analysis of LPL III component C using the Umeshmotion+ALE method was aborted at t=0.17 s (see Figure 5. 15), when severe mesh distortion was observed and when ablation depth at the center of the composite panel reached $1.54 \cdot 10^{-3}$ m, which is relatively close to the interface between Layer 1 and Layer 2 (see Table 5. 1 for the thickness of the layers). This proved that the Umeshmotion+ALE is inadequate for ablation modeling in the laminated composites subjected to the realistic lightning currents and, therefore, the element deletion method needs to be used. The FEA heat transfer analysis of LPL III component C using the

element deletion method was successfully completed. The ablation depth at the center of the composite panel, r=0, as a function of time is shown in Figure 5. 15. As one can see, Layer 1 and a part of Layer 2 are ablated. The results obtained using the element deletion method are also in a good agreement with the results obtained using the Umeshmotion+ALE method in the region where the Umeshmotion+ALE method is applicable.

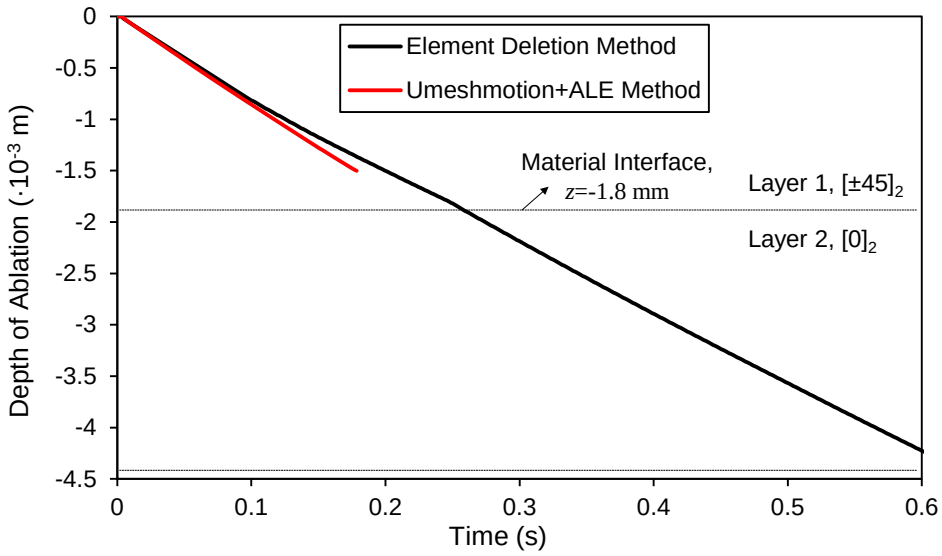

Figure 5. 15: Depth of ablation vs. time at the center of the composite panel, component C, LPL III case: comparison between element deletion method and Umeshmotion+ALE method.

Table 5. 5 contains the numerical results and approximate percent relative errors. It can be seen that the percent relative error for the ablation depth increases with time, as the ablation front approaches the material interface between Layer 1 and Layer 2 and computations using the Umeshmotion+ALE method become increasingly inaccurate.

Table 5. 5: Ablation depth vs. time at the center of the composite panel at the beginning of the component C, LPL III: comparisons between the Umeshmotion+ALE method and the element deletion method.

Time (s)	Ablation Depth (m)		Depth Difference (m)	Percent Relative Error
	Umeshmotion+ALE Method	Element Deletion Method		
0.01	$-6.73\cdot10^{-5}$	$-6.67\cdot10^{-5}$	$5.41\cdot10^{-7}$	0.80%
0.02	$-1.57\cdot10^{-4}$	$-1.55\cdot10^{-4}$	$9.58\cdot10^{-6}$	1.21%
0.05	$-4.24\cdot10^{-4}$	$-4.07\cdot10^{-4}$	$1.64\cdot10^{-5}$	3.87%
0.10	$-8.57\cdot10^{-4}$	$-8.17\cdot10^{-4}$	$3.96\cdot10^{-5}$	4.62%
0.12	$-1.03\cdot10^{-3}$	$-9.64\cdot10^{-4}$	$6.16\cdot10^{-5}$	6.01%
0.15	$-1.28\cdot10^{-3}$	$-1.18\cdot10^{-3}$	$9.77\cdot10^{-5}$	7.65%

Further comparisons in predictions using the Umeshmotion+ALE method and the element deletion method can be found in Figure 5. 16, where temperature distributions in the through-the-thickness direction at the center of the composite panel, r=0, at times t=0.05 s and t=0.15 s are shown.

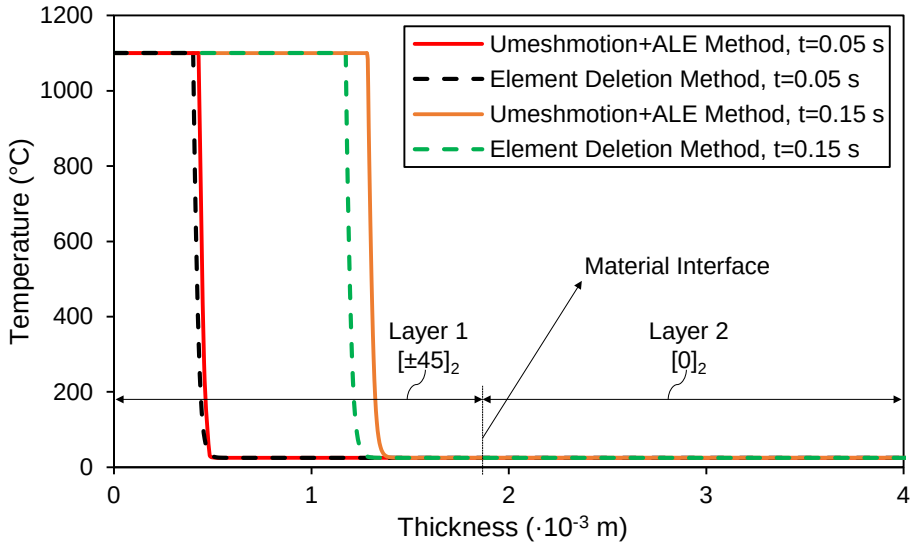

Figure 5. 16: Temperature distributions in the through-the-thickness direction at the center of the composite panel, at t=0.05 s and t=0.15 s, component C, LPL III: comparisons between the Umeshmotion+ALE method and the element deletion method.

Components C for LPL I and LPL II cases were investigated using FEA with the element deletion method only. Ablation depth and temperature distributions were obtained and analyzed. Figure 5. 17 shows depth of ablation vs time for all three LPL levels. Figure 5. 18 shows the ablation front radius vs time at the surface for all three LPL levels. Figure 5. 19 shows the ablation front contours in (r, z)-plane at different moments of time Figure 5. 20 shows ablation profiles for LPL I, LPL II, and LPL III at the end (t=0.6 s) of component C. Thicknesses of the laminate subsurface layers are also shown. The results indicate that ablation depths at the end of component C are $5.13 \cdot 10^{-3}$ m (LPL I case), $4.66 \cdot 10^{-3}$ m (LPL II case), and $4.22 \cdot 10^{-3}$ m (LPL III case). As one can see, in all three cases, the ablation depth is greater than the thickness of Layer 1 of the laminate. The radius of the ablation zone at the surface of the composite panel at the end of component C reaches 0.027 m (LPL I case), 0.024 m (LPL II case), and 0.020 m (LPL III case).

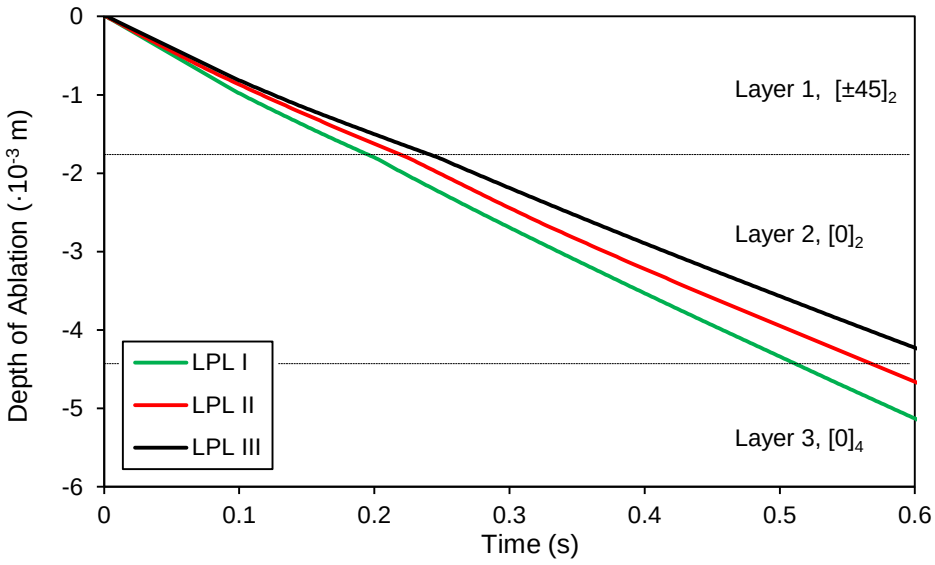

Figure 5. 17: Depth of ablation vs. time at the center of the composite panel, component C, LPL I, LPL II, and LPL III.

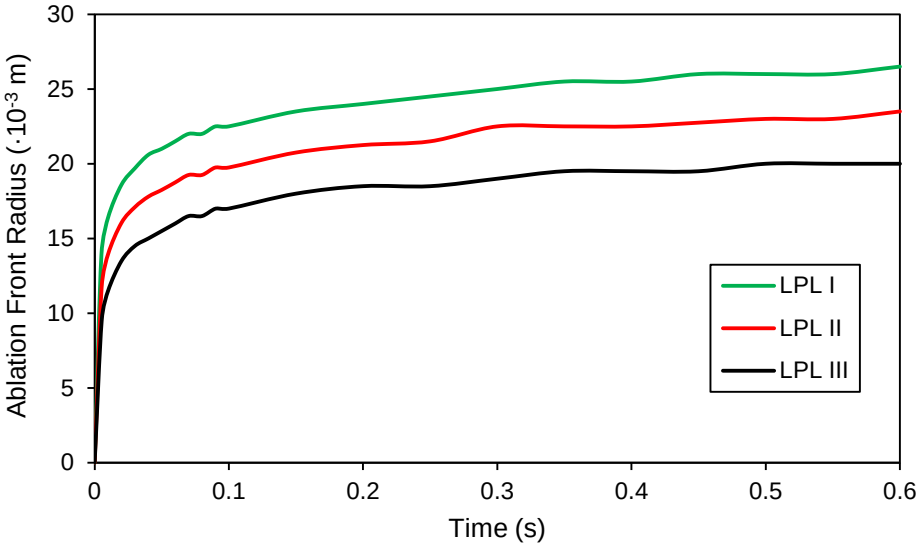

Figure 5. 18: Ablation front radius vs. time at the surface of the composite panel, component C, LPL I, LPL II, and LPL III.

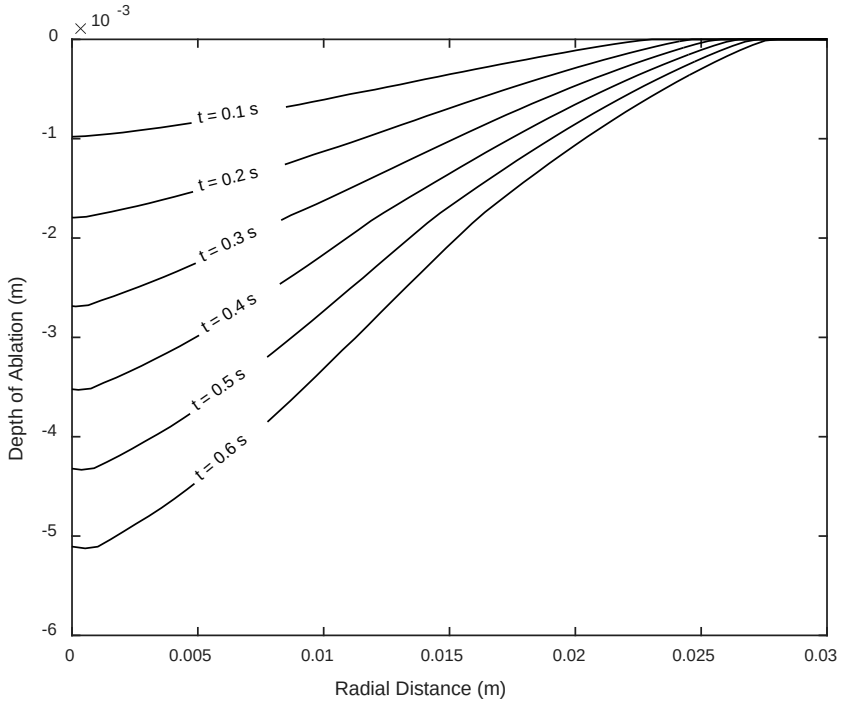

Figure 5. 19: Ablation front contours at different moments of time, component C, LPL I.

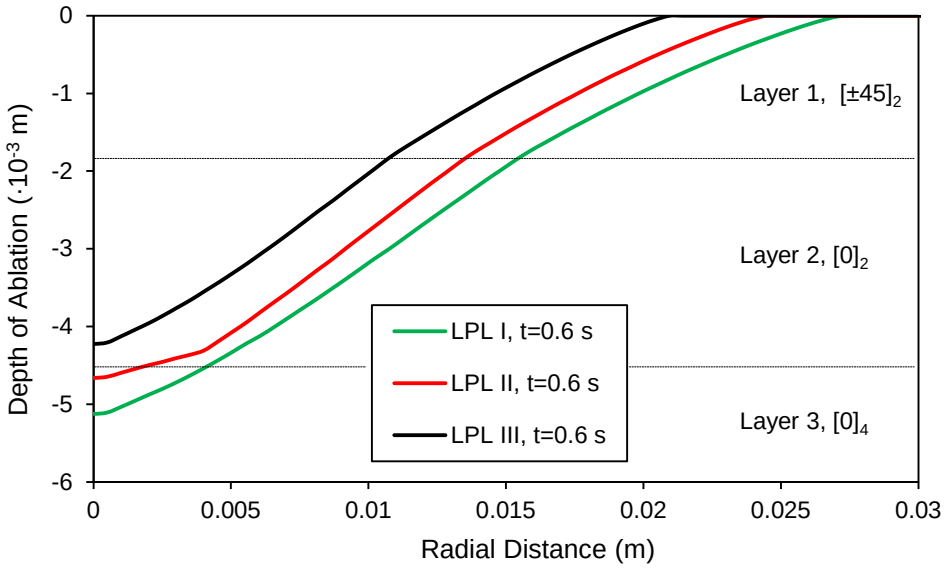

Figure 5. 20: Ablation zone profiles at the end (*t*=0.6 s) of component C, LPL I, LPL II, and LPL III.

Figure 5. 21 shows the temperature profile in the through-the-thickness direction. Figure 5. 22 shows the distribution of the temperature field in the radial direction at the surface of the panel at time t=0.3 s and t=0.6 s. Figure 5. 23 shows the overall ablation profiles and the temperature changes at time t=0.1 s, t=0.2 s, t=0.3 s, t=0.4 s, t=0.5 s, and t=0.6 s in the laminated composite panel due to continuing lightning current for LPL I. The majority of the temperature changes are found to be at the surface the composite panels. The subsequent laminate layers are not significantly affected by the lightning-current-induced heat flux. This is due to the progressive surface ablation which continuously disposes the excessive heat from the lightning channel.

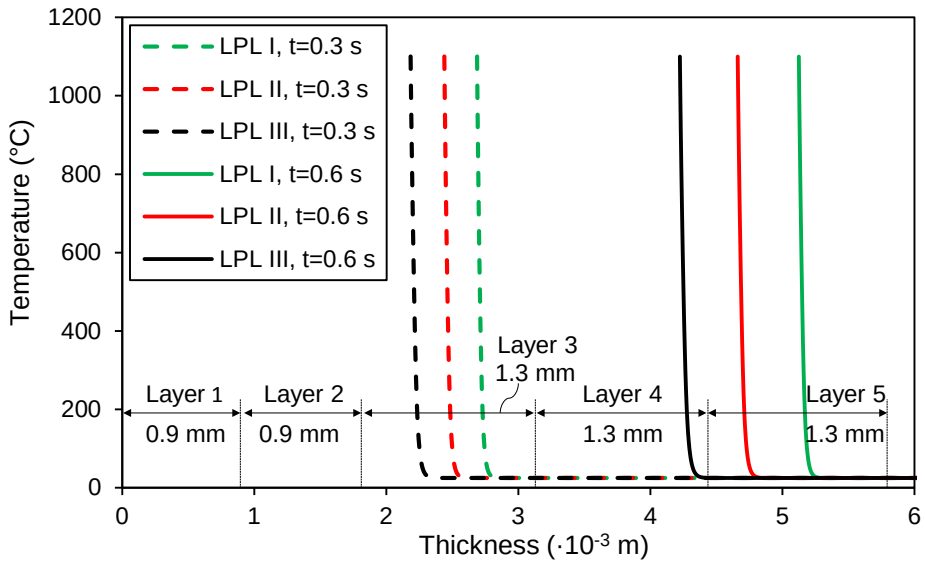

Figure 5. 21: Temperature in the through-the-thickness direction at r=0, at t=0.3 s and t=0.6 s of the composite panel due to continuing lightning current for different LPL cases using the element deletion method.

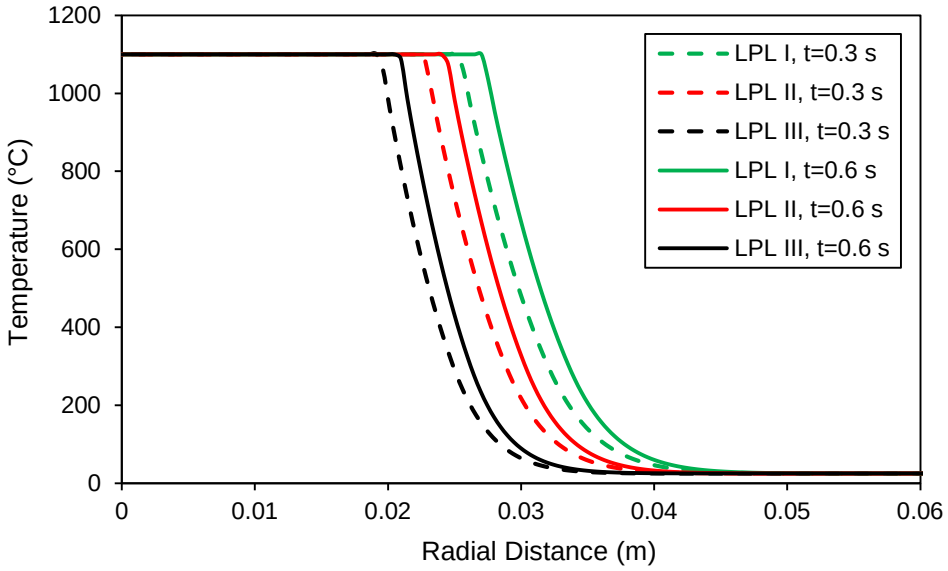

Figure 5. 22: Temperature in the radial direction on the surface of the panel at *t*=0.3 s and *t*=0.6 s of the composite panel due to continuing lightning current for different LPL cases using the element deletion method.

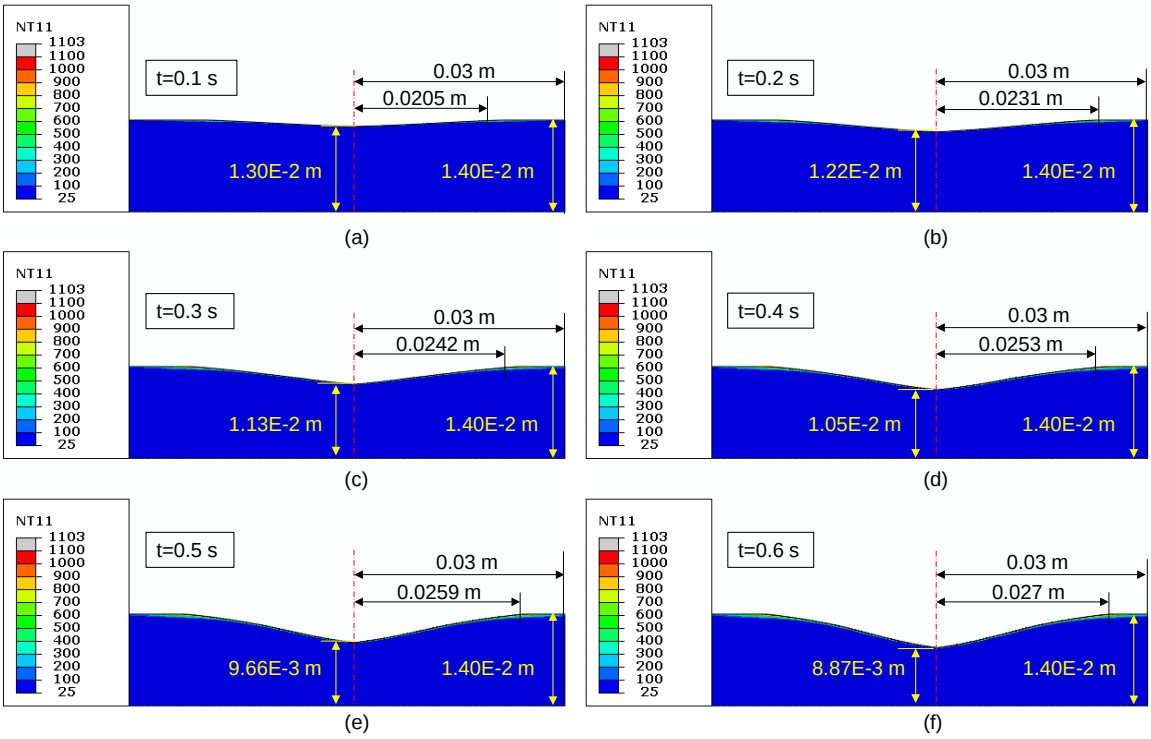

Figure 5. 23: Cross section contour plots of the ablation profile and temperature distribution at various times of the composite panel due to continuing lightning current for LPL I using the element deletion method.

Figure 5. 24 shows a zoomed in contour plot of temperature in the composite panel at the end of component C, LPL I. As one can see, there is a severe temperature gradient in the region immediately adjacent to the ablation front. The results for LPL II and LPL III cases are similar.

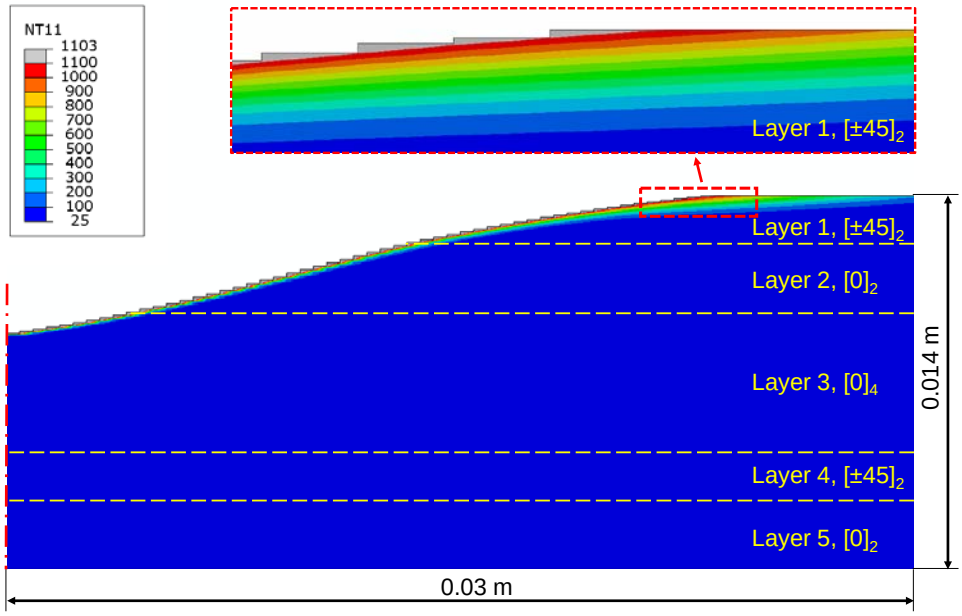

Figure 5. 24: Temperature distribution in the composite panel at the end of component C, LPL I.

CHAPTER 6
MODELING OF LIGHTNING-INDUCED THERMAL ABLATION DAMAGE IN CFRP LAMINATED COMPOSITE PANELS

6.1 Introduction

Carbon-fiber-reinforced polymer-matrix (CFRP) composites are typically stronger and lighter than glass-fiber-reinforced polymer-matrix (GFRP) composites. To provide improved reliability and damage tolerance for wind turbine blades, using CFRP composite laminates has been considered an alternative solution. In particular for offshore wind turbines, which requires long blades (>100 m) for large power production, CFRP composite laminates are widely used due to their superior strength- to-weight ratio. However, this also raises new challenges in the development of lightning strike protection systems. Unlike the non-conductive GFRP composites, CFRP composites are electrically conductive. Therefore, in addition to the direct heat injection, the Joule heating is generated when lightning current flows through the structure and leads to more extensive damage and even catastrophic structural failure.

Although a considerable number of experimental studies (Feraboli & Miller, 2009; Feraboli & Kawakami, 2010; Gou et al., 2010; Hirano et al., 2010; Li et al., 2015; Mall et al., 2009; Naghipour et al., 2006) examining lightning-strike-induced damage in CFRP composite laminates have been produced in recent years, the predictive numerical models (Abdelal & Murphy, 2014; F. S. Wang et al., 2014; Muñoz et al., 2014; Ogasawara et al., 2010) are extremely limited and are still far from maturity. In the existing literature, no actual progressive thermal ablation has been modeled within the FEM simulation. In the work by Ogasawara et al. (2010), the damage zones (i.e., delamination zone, surface recession zone) affected by the lightning-strike-induced heat

were estimated from the temperature distribution obtained from the simulations. The same method of damage estimation has been adopted by Muñoz et al. (2014). Abdelal et al. (2014) assumed that the thermal ablation in the CFRP composite laminated panel comes from material surface vaporization and used the Hertz-Knudsen equation to track the ablation rate. In addition, to move the electric current boundary condition to the next laminate layer once the preceding laminate layer was ablated, the CFRP composite laminated panel was assumed to have a fictitious high electrical conductivity (1×10^6 S/mm) in the through-the-thickness direction when ablation occurs at 3316 °C (Abdelal & Murphy, 2014). However, none of these studies (Abdelal & Murphy, 2014; Muñoz et al., 2014; Ogasawara et al., 2010) predicted the progressive shape change (i.e., ablation profile) of the CFRP composite laminated panel.

This chapter focuses on the modeling of the thermal ablation in CFRP composite laminates subjected to lightning strike. The problem formulation for GFRP composites presented in Chapter 5 is modified to take into account both direct heat injection and Joule heating produced by lightning strikes in the CFRP composites. A corresponding computational procedure with finite element analysis (FEA) by integrating ABAQUS and MATLAB is developed. The computational procedure allows the prediction of lightning-strike-induced progressive thermal ablation in the CFRP composite laminates due to both direct heat injection and Joule heating. This procedure enables the user to account for the moving boundary of the expanding lightning channel and the phase transition moving boundary associated with instantaneous material removal due to sublimation through the development of two ABAQUS user-subroutines and the MATLAB scripts.

6.2 Problem Formulation

In an electrically conductive material (e.g., a CFRP composite), Joule heating is produced when the energy dissipated by the lightning current, which is conducted through the material, is converted into thermal energy. The temperature response due to the electric current and surface heat flux can be formulated using Maxwell's equation of conservation of charge and thermal energy balance law (i.e., equation (5-1)). The two sets of equations are highly coupled due to the Joule heat generation $\boldsymbol{Q_J}$ by the electric current conduction:

$$Q_J = \mathbf{J} \cdot \mathbf{E}. \tag{6-1}$$

The Maxwell's equation of conservation of charge, in the case of steady-state direct current (i.e., lightning current component C), the equation is written as:

$$\nabla \cdot \mathbf{J} = 0. \tag{6-2}$$

In addition, the conduction of electric current is described by Ohm's law:

$$\mathbf{J} = \boldsymbol{\sigma} \cdot \mathbf{E}, \tag{6-3}$$

where **J** is the electric current density tensor, $\boldsymbol{\sigma}$ is the anisotropic temperature-dependent electrical conductivity tensor, T is the temperature, and **E** is the electrical field tensor.

The center on the top surface of the CFRP laminated composite panel is applied with the lightning-strike-induced electric current and surface heat flux (see Figure 6. 1):

$$\begin{cases} -\sigma_3(T)\left.\dfrac{\partial V}{\partial z}\right|_{z=0} = J(r,t), & r \le R(t), \\ -k_3(T)\left.\dfrac{\partial T}{\partial z}\right|_{z=0} = Q(r,t), & r \le R(t), \end{cases} \tag{6-4}$$

where σ_3 and k_3 are the electrical conductivity and thermal conductivity in the through-the-thickness direction, respectively. $R(t)$ is the instant lightning channel radius. J and Q are the lightning-strike-induced electric current and surface heat flux, respectively, and are both expressed as a function of radial coordinate r and time t (see Sections 4.3 and 4.4):

$$\begin{cases} J(r,t) = -\dfrac{\ln(0.1)}{(0.55)^2}\dfrac{1}{\left(1-e^{\frac{\ln(0.1)}{(0.55)^2}\cdot R^2(t)}\right)}\dfrac{I(t)}{\pi R^2(t)}e^{\frac{\ln(0.1)}{(0.55\cdot R(t))^2}\cdot r^2}, & r \le R(t), \\ Q(r,t) = -\dfrac{\ln(0.1)}{(0.55)^2}\dfrac{10}{\left(1-e^{\frac{\ln(0.1)}{(0.55)^2}\cdot R^2(t)}\right)}\dfrac{I(t)}{\pi R^2(t)}e^{\frac{\ln(0.1)}{(0.55\cdot R(t))^2}\cdot r^2}, & r \le R(t). \end{cases} \tag{6-5}$$

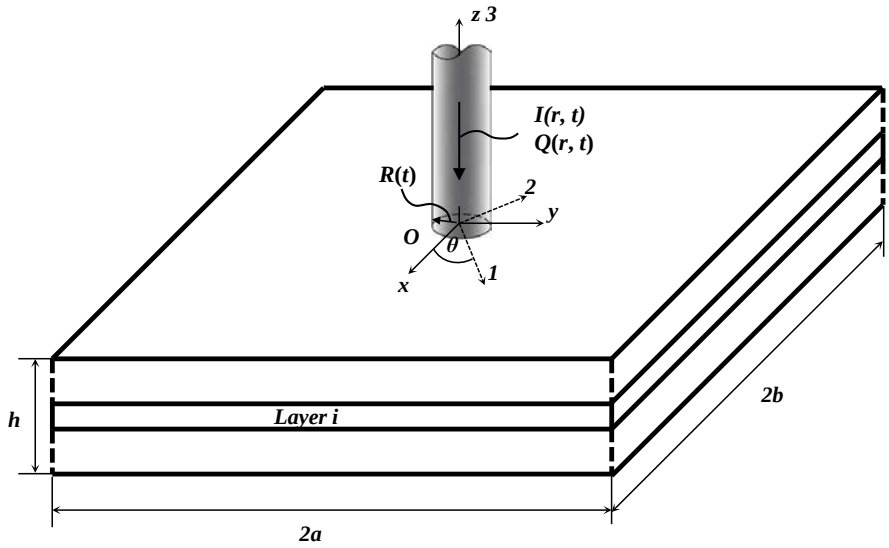

Figure 6. 1: CFRP composite laminated panel subjected to lightning-strike-induced electric current and surface heat flux.

Furthermore, the four side edges and the bottom surface of the panel are adiabatic and are applied with zero electric potential.

$$V\big|_{x=\pm b} = 0,\ V\big|_{y=\pm a} = 0,\ V\big|_{z=-h} = 0. \tag{6-6}$$

In addition, thermal radiation between the ambient environment and the top surface of the panel is considered as a natural boundary condition as the exterior surface of the CFRP composite panel is directly exposed to the ambient environment (see equation (5-4) in Section 5.1). However, surface convection is neglected due to the short duration of the lightning strike event.

6.3 Composite Structure

The CFRP composite panel considered in this thesis study is chosen as the CFRP composite substrate in the experimental study by NASA (Salah et al., 2013), so as to enable the model validation with the experimental results reported in the NASA study (Salah et al., 2013).

6.3.1 Composite Materials and Laminate Schedule

The CFRP composite laminate panel consists of 16 unidirectional Hexcel 8552/AS4 composite lamina layers and two woven fabric Hexcel 8552/AS4 composite lamina layers (Salah et al., 2013). The fiber volume fraction, density at room temperature and thickness of the unidirectional and woven fabric laminae are shown in Table 6. 1. The laminate schedule is: [(0/90F)/45/90/-45/0/45/90/-45/0/0/-45/90/45/0/-45/90/45/(0/90F)] (Salah et al., 2013). The total thickness of the composite laminate is 2.47 mm.

Table 6. 1: Fiber volume fraction, density at room temperature and ply thickness of the unidirectional and woven fabric composite laminae (Product Data. HexPly® 8552 Epoxy matrix, 2014).

Laminate	Fiber Volume Fraction	Density at Room Temperature (g/cm^3)	Thickness (mm)
Hexcel 8552/AS4 (Unidirectional)	57.42%	1.58	0.130
Hexcel 8552/AS4 (Woven)	55.29%	1.57	0.195

6.3.2 Temperature-dependent Thermophysical Properties

The temperature-dependent material properties of the CFRP composites depend on resin decomposition, thermal oxidation and fiber sublimation under elevated temperature. The reported temperature-dependent thermophysical properties of CFRP composites are not quite consistent in the existing literature. For example, Table 6. 2 lists the thermophysical properties of the unidirectional CFRP composite lamina from room temperature (25 °C) to the sublimation temperature of carbon fiber (3316 °C) reported by Griffis et al. (1986), while Table 6. 3 lists the temperature-dependent thermophysical properties of the unidirectional CFRP composite lamina used in the work by Abdelal & Murphy (2014). It can be noticed that the longitudinal thermal conductivities reported by Griffis et al. (1986) are much larger than those reported by Abdelal & Murphy (2014). Thermophysical properties play significant roles in determining thermal response and thermal ablation in the CFRP composite structures. Using different temperature-dependent thermophysical properties can result in significantly different predictions of thermal response and thermal ablation in the CFRP composite structure. For woven CFRP composite lamina, it is generally assumed that the density and the thermal properties are the same as those of the unidirectional lamina, except that the thermal conductivity in the longitudinal direction is equal to the thermal conductivity in the transverse direction.

Table 6. 2: Temperature-dependent CFRP composite (unidirectional lamina) thermal-physical properties reported by Griffis et al. (1986).

Temperature, T (°C)	Density, ρ (kg/m^3)	Thermal Conductivity, k (W/m·°C)			Specific Heat, c (J/kg·°C)
		Longitudinal	Transverse	Through-the-thickness	
25	1.597	46.863	0.682	0.682	1225
330	1.597	28.790	0.407	0.407	2057
360	1.597	27.103	0.378	0.378	3178
375	1.597	26.400	0.368	0.368	5032
500	1.597	18.800	0.241	0.241	4910
525	1.150	17.400	0.223	0.223	3645
573	1.150	14.800	0.176	0.176	1646
815	1.150	12.810	0.155	0.155	1720
1168	1.150	10.790	0.125	0.125	1825
3316	1.150	10.603	0.125	0.125	2510

Table 6. 3: Temperature-dependent CFRP composite (unidirectional lamina) thermal-physical properties reported by Abdelal & Murphy (2014).

Temperature, T (°C)	Density, ρ (kg/m^3)	Thermal Conductivity, k (W/m·°C)			Specific Heat, c (J/kg·°C)
		Longitudinal	Transverse	Through-the-thickness	
25	1.52	8	0.67	0.67	1065
343	1.52	2.608	0.18	0.18	2100
500	1.10	1.736	0.10	0.10	2100
510	1.10	1.736	0.10	0.10	1700
1000	1.10	1.736	0.10	0.10	1900
3316	1.10	1.736	0.10	0.10	2509
>3316 (load elements – gas)	1.10	1.015	1.015	0.10	5875
>3316 (unload elements – gas)	1.10	1.015	1.015	0.10	5875

6.3.3 Electrical Conductivity of CFRP Composite Laminates at Room Temperature

The anisotropic electrical conductivity of the CFRP composite laminate is also temperature-dependent. However, experimental data on the electrical conductivity of CFRP composites above ~330 °C has rarely been reported. In this study, a micromechanics approach is used to determine the anisotropic electrical conductivity of the CFRP composites from room temperature (25 °C) to the sublimation temperature of carbon fiber (3316 °C).

First, the electrical conductivity of the CFRP composites at room temperature is determined using the rule of mixtures:

$$\sigma_1 = \sigma_f V_f + \sigma_m (1 - V_f), \tag{6-7}$$

where σ_1 is the overall electrical conductivity of the composite lamina in the longitudinal direction (in S/m); σ_f is the electrical conductivity of carbon fiber (in S/m); V_f is the fiber volume fraction; σ_m is the electrical conductivity of the polymer-matrix (resin); and σ_m = 4.9×10^{-16} S/m (Product Data. HexPly® 8552 Epoxy matrix, 2014), which is considered electrically non-conductive. Therefore, equation (6-7) can be reduced to

$$\sigma_1 = \sigma_f V_f . \tag{6-8}$$

Note that the electrical conductivity for AS4 carbon fiber is σ_f =5.88×10^{4} S/m (Product Data. HexTow AS4, 2016).

The electrical conductivities in the transverse direction σ_2 and in the through-the-thickness direction σ_3 of the CFRP composite lamina are much lower than the electrical conductivity in the longitudinal direction. Generally, the CFRP fiber network in the

transverse direction and in the through-the-thickness direction are quite similar. However, due to the existence of the resin-rich regions between plies in the through-the-thickness direction (see Figure 6. 2), the electrical conductivity in the through-the-thickness direction is even lower than the electrical conductivity in the transverse direction. Similar to the thermophysical properties, the directional electrical conductivities reported in the existing literature are also not quite consistent. For instance, in the work by Kawakami (2011), the electrical conductivity in the transverse direction is $\sigma_2=5\times10^{-5}\sigma_1$, and the electrical conductivity in the through-the-thickness direction is $\sigma_3=8\times10^{-6}\sigma_1$ for unidirectional CFRP lamina and $\sigma_3=1\times10^{-6}\sigma_1$ for woven fabric CFRP lamina. However, Ogasawara et al. (2010) reported that $\sigma_2=2.68\times10^{-5}\sigma_1$, $\sigma_3=2.7\times10^{-8}\sigma_1$. Using either of these two relationships, the overall anisotropic electrical conductivities for the two types (i.e., unidirectional and woven) of composite laminae can be roughly estimated. The directional electrical conductivity obtained using the relationship by Kawakami (2011) for the current composite laminate is denoted as the "Kawakami relationship," while the electrical conductivity obtained using the relationship by Ogasawara et al. (2010) is denoted as the "Ogasawara relationship." They are both tabulated in Table 6. 4. It can be noted that the electrical conductivities in the through-the-thickness direction, σ_3, obtained using the "Ogasawara relationship" are two to three orders of magnitude lower than those obtained using the "Kawakami relationship." Since the generation of Joule heating is proportional to inverse of the electrical conductivity, J^2/σ, the two to three orders of magnitude difference between the electrical conductivity can have a significant impact on the prediction of thermal response and thermal ablation. In addition, it is worth noting that for woven composite lamina, the electrical conductivity in the longitudinal direction and in the transverse direction are generally considered the same, $\sigma_1= \sigma_2$.

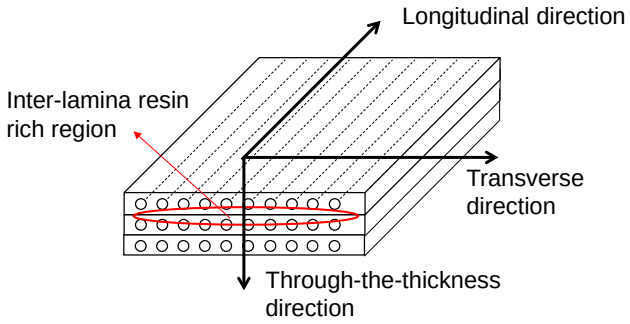

Figure 6. 2: Schematic of the inter-lamina resin-rich region.

Table 6. 4: AS4/8552 CFRP composite electrical conductivity at room temperature.

Unidirectional Hexcel 8552/AS4 Lamina			
Direction	Longitudinal (S/mm)	Transverse (S/mm)	Through-the-thickness (S/mm)
Kawakami Relationship	σ_1=33.8	$\sigma_2=1.69\times10^{-3}$	$\sigma_3=2.704\times10^{-4}$
Ogasawara Relationship	σ_1=33.8	$\sigma_2=9.08\times10^{-4}$	$\sigma_3=9.160\times10^{-7}$
Woven Hexcel 8552/AS4 Lamina			
Kawakami Relationship	σ_1 =32.5	σ_2=32.5	$\sigma_3=3.25\times10^{-5}$
Ogasawara Relationship	σ_1 =32.5	σ_2=32.5	$\sigma_3=8.81\times10^{-7}$

Table 6. 5 shows the comparisons of the obtained overall anisotropic electrical conductivities for the unidirectional composite lamina at room temperature with those reported in the literature (Abdelal & Murphy, 2014; Liu et al., 2015; Muñoz et al., 2014; Kawakami, 2011; Ogasawara et al., 2010). The type of composite material is shown in parentheses after the first author name in the first column of the table. Note that electrical

conductivities reported by Ogasawara et al. (2010), Muñoz et al. (2014), and Kawakami (2011) were obtained experimentally. Studies by Abdelal & Murphy (2014) and Liu et al. (2015) did not report how the electrical conductivities were determined. It can be noted in Table 6. 5 that our results (i.e., the current study in Table 6. 5) for the electrical conductivities in the longitudinal direction and in the transverse direction are consistent with the other results reported in the literature. However, the results for the electrical conductivity in the through-the-thickness direction are quite different.

Table 6. 5: Overall electrical conductivity of the unidirectional CFRP composites at room temperature: comparisons between results reported in different studies.

Models	Electrical Conductivity (S/mm)		
	σ_1	σ_2	σ_3
Current study, Kawakami Relationship (AS4/8552)	33.8	1.690×10^{-3}	2.704×10^{-4}
Current study, Ogasawara Relationship (AS4/8552)	33.8	9.08×10^{-4}	9.160×10^{-7}
Ogasawara et al. (2010) (IM600/133)	29.3	0.787×10^{-3}	7.940×10^{-7}
Abdelal & Murphy (2014) (IM600/133)	35.97	1.145×10^{-3}	3.876×10^{-6}
Muñoz et al. (2014) (G0986/RTM6-2)	14.631	Not available	2.700×10^{-3}
Liu et al. (2015) (Not specified)	34.6	1.220×10^{-3}	3.240×10^{-6}
Kawakami (2011) (T700/2510)	23.09	8.000×10^{-3}	1.1236×10^{-4}
Kawakami (2011) (T800/3900)	16.58	1.028807×10^{-3}	8.4034×10^{-5}
Kawakami (2011) (IM7/977-3)	39.68	1.964637×10^{-3}	3.22581×10^{-4}

6.3.4 Temperature-dependent Directional Electrical Conductivity

In the existing literature related to lightning strike modeling on CFRP composites, assumptions have been made for the temperature-dependent electric conductivity. In the work by Ogasawara et al. (2010), the electrical conductivity in the through-the-thickness direction of the CFRP is assumed to increase linearly from 7.94×10^{-7} S/m to 0.1 S/m (1.3×10^{5} times) when lightning-induced surface recession starts to occur at a temperature above 600 °C until the carbon fiber sublimation temperature at around 3000 °C. In the work by Abdelal & Murphy (2014), the electrical conductivities in the transverse direction and in the through-the-thickness direction of the CFRP composites are assumed to increase linearly from 0.001145 S/m to 2 S/m and from 3.876×10^{-6} S/m to 2 S/m, respectively, when the temperature exceeds 343 °C (when resin starts to decompose) until 500 °C; above that, the electrical conductivities are assumed to be temperature-independent. Liu et al. (2015) used temperature-independent electrical conductivity in their study, as they claimed that the temperature-dependent electrical properties are difficult to measure and no available experimental data can be used. Muñoz et al. (2014) also assumed temperature-independent electrical conductivity for the CFRP composite used in their simulation, except for the electrical conductivity in the through-the-thickness direction, which is assumed to be five times higher when the temperature exceeds 600 °C.

In the meantime, studies have also shown that the electrical conductivity of the carbon fiber itself is temperature-dependent. Therefore, equation (6-8) becomes

$$\sigma_1(T) = \sigma_f(T)V_f. \tag{6-9}$$

The temperature-dependency of the electrical conductivity for carbon fiber $\sigma_f(T)$ is found to be similar to that of semiconductors (Sauder et al., 2002). The fiber volume fraction V_f is assumed to be a constant (the effect of mass loss to the electrical conductivity of the overall composite laminate is ignored). Typically, the electric conduction of a semiconductor is governed by lattice scattering when carrier concentration is intrinsic, particularly at high temperature (>100 °C). The temperature-dependency when T>100 °C can be characterized using the Arrhenius equation; the natural logarithm of the electrical conductivity is linear to the inverse of temperature,

$$\ln \sigma_f = -\frac{\Delta E}{2k_b}\frac{1}{T} + \ln C, \tag{6-10}$$

where σ_f is the electrical conductivity of carbon fiber (in S/m); C is a constant; ΔE (in ev) is the energy gap (activation energy) between the strip of valence E_V and the strip of conduction E_C ($\Delta E=E_C-E_V$); k_b is the Boltzmann constant, k=8.617×10^{-5} ev/K; and T is temperature (in K). To use this equation, the temperature unit must be converted from Celsius to Kelvin.

Sauder et al. (2002) studied the electrical conductivity of a PAN-based fiber in the longitudinal direction at temperature range 90 °C ~1800 °C using experimental measurements. The data points in Figure 6. 3 show their obtained electrical conductivity in a natural logarithm scale as a function of the inverse of temperature. The line in Figure 6. 3 indicates the slope of the data points, which is $-\Delta E/2k$ in equation (6-10), and is plotted at temperature range 330 °C ~ 1800 °C. The corresponding activation energy value ΔE at temperature range 330 °C ~ 1800 °C is ΔE= 0.12 ev. The activation energy value ΔE at low temperature range 25 °C ~ 330 °C is obtained by assuming the electrical conductivity at low temperature range also follows the Arrhenius equation. The slope of

the data points at the corresponding low temperature range 25 °C ~ 330 °C can be obtained, and therefore, so can the activation energy, which is obtained as ΔE = 0.0024 ev. At high temperature range 1800 °C ~ 3316 °C, it is assumed that the activation energy value equals the value at medium temperature range 330 °C ~ 1800 °C, ΔE= 0.12 ev.

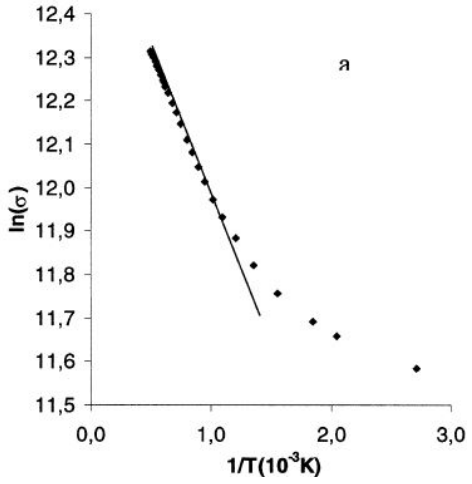

Figure 6. 3: Electrical conductivity of a PAN-based carbon fiber versus temperature (Sauder et al., 2002).

The temperature-dependent electrical conductivity of AS4 carbon fiber $\sigma_f(T)$ is therefore calculated using equation (6-10). Constant C in equation (6-10) is calculated using the boundary condition $\sigma_f(T$=25 °C) = 33.8 S/mm (for unidirectional laminate composite). After the temperature-dependent electrical conductivity of AS4 carbon fiber $\sigma_f(T)$ is determined, equation (6-9) is used to calculate the temperature-dependent electrical conductivity of the overall laminate composite in the longitudinal direction, $\sigma_1(T)$. The temperature-dependent electrical conductivities of the overall laminate composite in the transverse direction and in the through-the-thickness direction are

calculated by assuming that the activation energy values in these two directions are the same as those in the longitudinal direction (see Table 6. 6). The directional temperature-dependent electrical conductivities of CFRP composite laminate calculated based on the activation energy values reported by Sauder et al. (2002) are denoted as the “Elec. Cond. obtained using activation energy values by Sauder et al. (2002)” hereinafter.

However, we also found different activation energy values for the CFRP composite laminate in a study by Takahashi & Hahn (2011). In their work (Takahashi & Hahn, 2011), the directional electrical resistance from room temperature to ~60 °C was measured by the two-probe method. Different activation energy values at different directions of the CFRP composite laminate were reported (see Table 6. 6), unlike the previous case in which we determined the temperature-dependent electrical conductivity by assuming that the activation energy values are the same for all directions based on the original activation energy values of carbon fibers reported by Sauder et al. (2002). In this section, the directional temperature-dependent electrical conductivities using the activation energy values reported by Takahashi & Hahn (2011) are also calculated using equation (6-10). However, as mentioned earlier, the electrical resistance of the CFRP composite laminate was only measured up to ~60 °C (Takahashi & Hahn, 2011). It is therefore assumed that the activation energy values above ~60 °C are equal to those reported up to ~60 °C. In other words, the activation energy values are assumed to be temperature-independent. The directional temperature-dependent electrical conductivities of CFRP composite laminate calculated based on the activation energy values reported by Takahashi & Hahn (2011) are denoted as the “Elec. Cond. obtained using activation energy values by Takahashi & Hahn (2011)” hereinafter.

Table 6. 6: Activation energy values at different directions from different models.

Model	Temperature	Activation Energy, ΔE (ev)		
		Longitudinal	Transverse	Through-the-thickness
Sauder et al. (2002)	25 °C – 330 °C	0.0024	0.0024	0.0024
	330 °C – 3316 °C	0.12	0.12	0.12
Takahashi & Hahn (2011)	25 °C – 3316 °C	4.48×10^{-3}	1.19×10^{-2}	8.15×10^{-3}

The comparison of the directional temperature-dependent electrical conductivity for the overall composite lamina obtained using the activation energy values reported by Sauder et al. (2002) with those obtained using the activation energy values reported by Takahashi & Hahn (2011) is shown in Table 6. 7. One can see that the electrical conductivity in all directions increased by ~3 times from 25 °C to 3316 °C predicted using the activation energy values reported by Sauder et al. (2002), whereas the increase of the electrical conductivity in all directions from 25 °C to 3316 °C predicted using the activation energy values reported by Takahashi & Hahn (2011) is less than 25%. Therefore, using the temperature-dependent electrical conductivity predicted using the activation energy values reported by Sauder et al. (2002) will result in the prediction of a smaller thermal ablation in the CFRP composite laminate than that using the temperature-dependent electrical conductivity predicted using the activation energy values reported by Takahashi & Hahn (2011).

Table 6. 7: Temperature-dependent directional electrical conductivities: comparison between proposed model using the activation energy values reported by Sauder et al. (2002) and the one using the activation energy values reported by Takahashi & Hahn (2011).

Temp	Elec. Cond. obtained using activation energy values by Sauder et al. (2002)			Elec. Cond. obtained using activation energy values by Takahashi & Hahn (2011)		
	σ_1	σ_2	σ_3	σ_1	σ_2	σ_3
(°C)	(S/mm)	(S/mm)	(S/mm)	(S/mm)	(S/mm)	(S/mm)
25	33.8	0.00169	0.00027	33.8	0.000908	9.16E-07
100	34.11688	0.001706	0.000273	34.39391	0.000951	9.45E-07
330	34.60375	0.00173	0.000277	35.31578	0.00102	9.92E-07
500	44.56958	0.002228	0.000357	35.65105	0.001046	1.01E-06
800	57.29741	0.002865	0.000458	35.98696	0.001073	1.03E-06
1000	63.43443	0.003172	0.000507	36.12393	0.001084	1.03E-06
1400	72.28205	0.003614	0.000578	36.30045	0.001098	1.04E-06
1800	78.31854	0.003916	0.000627	36.40931	0.001107	1.05E-06
2200	82.68663	0.004134	0.000661	36.48316	0.001112	1.05E-06
2600	85.98947	0.004299	0.000688	36.53654	0.001117	1.06E-06
3000	88.57254	0.004429	0.000709	36.57694	0.00112	1.06E-06
3316	90.2461	0.004512	0.000722	36.60251	0.001122	1.06E-06

In addition, the comparison of the obtained electrical conductivity using the Takahashi & Hahn (2011) model with those assumed in other studies is listed in Table 6. 8. It is worth noting that we determined the temperature-dependent directional electrical conductivity of the CFRP composite lamina by considering the experimental data for carbon fibers and using the rule of mixture. The temperature-dependent anisotropic electrical conductivity used in other studies is often based on arbitrary assumptions.

Table 6. 8: Temperature-dependent directional electrical conductivities: comparison between proposed model using the activation energy values reported by Takahashi & Hahn (2011) and assumptions used in other literature.

Temp	Elec. Cond. obtained using activation energy values by Takahashi & Hahn (2011) Model			Assumption by Ogasawara et al. (2010)			Assumption by Abdelal & Murphy (2014)			Assumption by Muñoz et al. (2014)		
	σ1	σ2	σ3	σ1	σ2	σ3	σ1	σ2	σ3	σ1	σ2	σ3
(°C)	(S/mm)	(S/mm)	(S/mm)	(S/mm)	(S/mm)	(S/mm)	(S/mm)	(S/mm)	(S/mm)	(S/mm)	(S/mm)	(S/mm)
25	33.8	0.000908	9.16E-07	29.3	0.000787	7.94E-07	35.97	0.001145	3.88E-06	14.631	n/a	2.70E-03
100	34.39391	0.000951	9.45E-07	29.3	0.000787	7.94E-07	35.97	0.001145	3.88E-06	14.631	n/a	0.004109
200	34.9016	0.000989	9.71E-07	29.3	0.000787	7.94E-07	35.97	0.001145	3.88E-06	14.631	n/a	0.005987
300	35.23647	0.001014	9.88E-07	29.3	0.000787	7.94E-07	35.97	0.001145	3.88E-06	14.631	n/a	0.007865
330	35.31578	0.00102	9.92E-07	29.3	0.000787	7.94E-07	35.97	0.001145	3.88E-06	14.631	n/a	0.008429
400	35.47391	0.001032	1E-06	29.3	0.000787	7.94E-07	35.97	0.726844	0.726117	14.631	n/a	0.009743
500	35.65105	0.001046	1.01E-06	29.3	0.000787	7.94E-07	35.97	2	2	14.631	n/a	0.011622
600	35.78826	0.001057	1.02E-06	29.3	0.000787	7.94E-07	35.97	2	2	14.631	n/a	0.0135
700	35.89767	0.001066	1.02E-06	29.3	0.000787	7.94E-07	35.97	2	2	14.631	n/a	0.0135
800	35.98696	0.001073	1.03E-06	29.3	0.000787	7.94E-07	35.97	2	2	14.631	n/a	0.0135
900	36.06121	0.001079	1.03E-06	29.3	0.000787	7.94E-07	35.97	2	2	14.631	n/a	0.0135
1000	36.12393	0.001084	1.03E-06	29.3	0.000787	7.94E-07	35.97	2	2	14.631	n/a	0.0135
1100	36.1776	0.001088	1.04E-06	29.3	0.005071	0.004319	35.97	2	2	14.631	n/a	0.0135
1200	36.22406	0.001092	1.04E-06	29.3	0.009355	0.008636	35.97	2	2	14.631	n/a	0.0135
1300	36.26466	0.001095	1.04E-06	29.3	0.013638	0.012954	35.97	2	2	14.631	n/a	0.0135
1400	36.30045	0.001098	1.04E-06	29.3	0.017922	0.017272	35.97	2	2	14.631	n/a	0.0135
1500	36.33223	0.0011	1.04E-06	29.3	0.022206	0.02159	35.97	2	2	14.631	n/a	0.0135
1600	36.36065	0.001103	1.05E-06	29.3	0.02649	0.025907	35.97	2	2	14.631	n/a	0.0135
1700	36.3862	0.001105	1.05E-06	29.3	0.030774	0.030225	35.97	2	2	14.631	n/a	0.0135
1800	36.40931	0.001107	1.05E-06	29.3	0.035057	0.034543	35.97	2	2	14.631	n/a	0.0135
1900	36.4303	0.001108	1.05E-06	29.3	0.039341	0.038861	35.97	2	2	14.631	n/a	0.0135
2000	36.44946	0.00111	1.05E-06	29.3	0.043625	0.043178	35.97	2	2	14.631	n/a	0.0135
2100	36.46702	0.001111	1.05E-06	29.3	0.047909	0.047496	35.97	2	2	14.631	n/a	0.0135
2200	36.48316	0.001112	1.05E-06	29.3	0.052193	0.051814	35.97	2	2	14.631	n/a	0.0135
2300	36.49805	0.001114	1.05E-06	29.3	0.056477	0.056132	35.97	2	2	14.631	n/a	0.0135
2400	36.51184	0.001115	1.05E-06	29.3	0.06076	0.060449	35.97	2	2	14.631	n/a	0.0135
2500	36.52463	0.001116	1.05E-06	29.3	0.065044	0.064767	35.97	2	2	14.631	n/a	0.0135
2600	36.53654	0.001117	1.06E-06	29.3	0.069328	0.069085	35.97	2	2	14.631	n/a	0.0135
2700	36.54766	0.001118	1.06E-06	29.3	0.073612	0.073403	35.97	2	2	14.631	n/a	0.0135
2800	36.55805	0.001119	1.06E-06	29.3	0.077896	0.07772	35.97	2	2	14.631	n/a	0.0135
2900	36.56779	0.001119	1.06E-06	29.3	0.082179	0.082038	35.97	2	2	14.631	n/a	0.0135
3000	36.57694	0.00112	1.06E-06	29.3	0.086463	0.086356	35.97	2	2	14.631	n/a	0.0135
3100	36.58555	0.001121	1.06E-06	29.3	0.090747	0.090674	35.97	2	2	14.631	n/a	0.0135
3200	36.59366	0.001121	1.06E-06	29.3	0.095031	0.094991	35.97	2	2	14.631	n/a	0.0135
3316	36.60251	0.001122	1.06E-06	29.3	0.1	0.1	35.97	2	2	14.631	n/a	0.0135

6.4 Numerical Treatment in FEA

A coupled electric-thermal transient step was defined to model the formulated problem (described in Section 6.2). The non-uniform lightning-strike-induced surface heat flux $Q(r, t)$ (6-5) is applied using an ABAQUS user-subroutine DFLUX, and the non-uniform surface electric current density $J(r, t)$ (6-5) is defined using the analytical field option in ABAQUS. In addition, the surface radiation boundary condition (5-4) was defined on the top surface of the CFRP composite laminated panel with uniform emissivity distribution. The coefficient of emissivity is 0.85, and the ambient temperature is 25 °C.

It is worth mentioning that ABAQUS does not allow the subroutine Umeshmotion to be used in a coupled electric-thermal step. Therefore, the Umshmotion+ALE method described in Section 5.3 is not applicable in the case of CFRP composite structure. In this section, the element deletion method described in Section 5.3 is modified to take into account the Joule heating generated by the conduction of lightning current for modeling thermal ablation in conductive CFRP composite structure.

Similar to the thermal ablation produced in GFRP composites, thermal ablation in the CFRP composite panel due to rapid fiber sublimation also results in a moving boundary condition. The surface of the material progressively recedes in the through-the-thickness direction and therefore requires the associated lightning-strike-induced electric current and surface heat flux (6-5) boundary conditions to move simultaneously with the receding surface (i.e., ablation front, see Figure 6. 4). The developed numerical procedure described in Section 5.3 enables element deletion once the temperature of the element exceeds a designated ablation temperature. In the case of CFRP composite, the designated ablation temperature is the sublimation temperature of carbon fiber (3316 °C). The developed numerical procedure also enables boundary condition update after elements are removed. Figure 6. 5 shows the schematic of the element deletion method

and boundary condition update for modeling thermal ablation with FEA. The element deletion is achieved using the keywords "*model change" with the ABAQUS Standard solver. As described in Section 5.3, we used an ABAQUS subroutine Umeshmotion to monitor the nodal temperatures. However, in the case of CFRP composites, Umeshmotion is not applicable in the coupled electric-thermal step; instead, another ABAQUS subroutine, URDFIL, was developed to monitor nodal temperatures after each time increment. The analysis is paused when the temperatures of the bottom nodes at any element reach the designated ablation temperature. The associated elements are identified and removed from subsequent analysis via Python scripts and MATLAB scripts. The analysis can be resumed after the surface current density and heat flux boundary conditions are reapplied via ABAQUS restart analysis. A MATLAB script controls the entire execution of the developed numerical procedure.

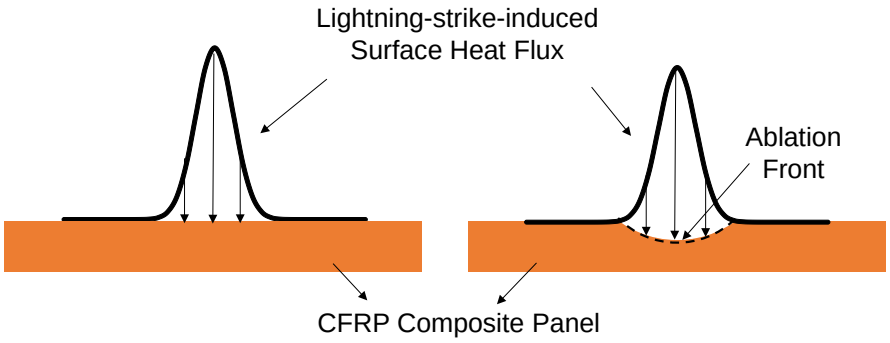

Figure 6. 4: Boundary condition update after materials are removed (same for lightning-strike-induced electric current).

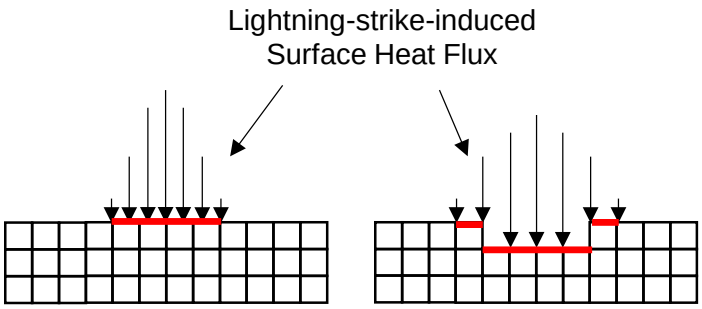

Figure 6. 5: Boundary condition update after materials are removed in FEA.

It should be mentioned that, in the existing literature, almost no attempts have been undertaken to simulate thermal ablation by progressive modeling. Ogasawara et al. (2010) introduced a virtual latent heat (1×10^{11} J/kg) to limit the maximum temperature to the sublimation temperature of carbon fiber (3000 °C) and estimated the lightning-strike-induced damage zones in the CFRP composite laminated panel based on the obtained temperature distribution from the simulations. The area of the surface recession (i.e., thermal ablation) zone caused by carbon sublimation was assumed to be the same as the areas where the temperature was ≥ 3000 °C. However, without modeling the moving boundary condition due to instant material phase transition, the introduction of virtual latent heat prevents the subsequent laminate layers from absorbing further energy, thus resulting in a significant underestimation of the depth of thermal ablation. The same method of damage estimation has also been used by Muñoz et al. (2014). In addition, Abdelal & Murphy (2014) assumed the material surface vaporization to be the ablation mechanism in the CFRP composite laminate due to lightning strike and used a Hertz-Knudsen equation to capture the ablation rate. However, since the materials are not actually removed during FEA after thermal ablation occurs, the update of the electric current boundary condition from the preceding layer to the next layer in their model still relies on using a fictitious high electrical conductivity (1×10^{6} S/mm) in the through-the-thickness direction of the CFRP composite laminate (Abdelal & Murphy, 2014). In

particular, Abdelal & Murphy (2014) assumed that the electrical conductivity in the through-the-thickness direction of the CFRP composite laminate increased from 3.876×10^{-6} S/mm to 2 S/mm (~5.2×10^{5} times) between 343 °C and 500 °C and increased from 2 S/mm to 1×10^{6} S/mm (5×10^{5} times) when the temperature exceeded 3316 °C. These drastic increases (five orders) of electrical conductivity may lead to severe numerical convergence issues.

6.5 FEA Results and Discussions

6.5.1 Effects of Thermal and Electrical Conductivity on Surface Ablation Area and Ablation Depth in CFRP Composites Due to Continuing Lightning Current

In this section, the effects of the thermal and electrical conductivity on the surface ablation area and ablation depth in the CFRP composite laminated panel due to lightning strike are investigated. As described earlier, a typical lightning strike consists of a pulsed current and a continuing current. In this section, we only consider the continuing lightning current

$$I(t) = 368 \text{ A}, \ t \le t_c, \tag{6-11}$$

where t_c is the duration of the continuing lightning current, t_c=0.468 s.

In addition, the lightning channel expands during the initial stage of lightning discharge (pulsed lightning current) due to the high pressure within the lightning channel. The channel radius becomes constant when the pressure within the lightning channel reaches equilibrium with the ambient pressure,

$$R = 0.097 I_{peak}^{1/3} t_r^{1/2}, \tag{6-12}$$

where I_{peak} is the peak value of the pulsed lightning current, I_{peak} =20,000 A and t_r is the duration of the lightning channel expansion. Theoretically, the lightning channel expands until the pressure within the lightning channel reaches equilibrium to the surrounding ambient pressure. However, very few studies on the evolution of lightning-induced pressure have been reported in the existing literature. In this section, it is assumed t_r=50 μs.

To investigate the effects of using different thermal and electrical conductivities on the resulting thermal ablation due to the continuing lightning current (6-11), in this section, FEA predictions of thermal ablations in the CFRP composite panel using various sets of directional thermal and electrical conductivities of the CFRP composite laminates are compared. For the purpose of comparison, exact predictions of thermal ablations are not pursued. Therefore, the developed element deletion method (described in Sections 5.3 and 6.4) is not used in this section. Instead, during FEA, the temperature of the elements is allowed to keep increasing beyond the ablation temperature (3316 °C). The area where the temperature is above 3316 °C is considered to be ablated. This method is denoted as the “Plain Heat Transfer Method.” It should be mentioned again that this Plain Heat Transfer Method does not predict the exact thermal ablations due to the lack of treatment for material phase transitions. The method is used only for the purpose of investigating the effects of using different directional thermal conductivities and electrical conductivities on the thermal ablations in the CFRP composites.

Three comparison cases are carried out, with each case containing two FEA simulations using different electrical or thermal conductivities. In the first case, the directional temperature-dependent electrical conductivity values for both FEA

simulations are taken from Table 6. 7 (Elec. Cond. obtained using activation energy values by Sauder et al. (2002)). The directional thermal conductivity for the two FEA simulations are assumed to be temperature-independent, and the values are different as are shown in Table 6. 9. This case is to investigate the effect of thermal conductivity on the resulting thermal ablation in the CFRP composites. In the second case, the directional temperature-dependent thermal conductivity values for both FEA simulations are taken from Table 6. 2, and the directional electrical conductivity for both two FEA simulations are assumed to be temperature-independent with σ_2= 0.00451231 S/mm, σ_3= 0.000721969 S/mm. The longitudinal electrical conductivity values for the two FEA simulations are different, as shown in

Table 6. 10. This case is to investigate the effect of longitudinal electrical conductivity on the resulting thermal ablation in the CFRP composites. In the third case, the same thermal conductivity values used in the second case are used. The directional electrical conductivity for both FEA simulations are also assumed to be temperature-independent with σ_1=33.8 S/mm, σ_2= 0.00451231 S/mm. The values of the electrical conductivity in the through-the-thickness direction for the two FEA simulations are different, as shown in Table 6. 11. This case is to investigate the effect of through-the-thickness electrical conductivity on the resulting thermal ablation in the CFRP composites.

Table 6. 9: The first comparison case: effect of thermal conductivity on the resulting thermal ablation in CFRP composites due to continuing lightning current.

FEA Simulation #	Thermal Conductivity (W/mm^2)	Max. Surface Ablation Radius (mm)	Max. Ablation Depth (mm)
1	k_1=0.010603, k_2=0.000125, k_3=0.000125.	19.86	0.4875
2	k_1=0.046863, k_2=0.000682, k_3=0.000682.	17.37	0.91
Difference		-12.50%	+86.7%

Table 6. 10: The second comparison case: effect of longitudinal electrical conductivity on the resulting thermal ablation in CFRP composites due to continuing lightning current.

FEA Simulation #	Electrical Conductivity (S/mm)	Max. Surface Ablation Radius (mm)	Max. Ablation Depth (mm)
1	σ_1=33.8, σ_2=4.51×10^{-3}, σ_3=7.22×10^{-4}.	19.86	0.5525
2	σ_1=14, σ_2=4.51×10^{-3}, σ_3=7.22×10^{-4}.	21.09	0.585
Difference		+6.19%	+5.88%

Table 6. 11: The third comparison case: effect of through-the-thickness electrical conductivity on the resulting thermal ablation in CFRP composites due to continuing lightning current.

FEA Simulation #	Electrical Conductivity (S/mm)	Max. Surface Ablation Radius (mm)	Max. Ablation Depth (mm)
1	σ_1=14, σ_2=4.51×10^{-3}, σ_3=8.68×10^{-5}.	20.46	0.5525
2	σ_1=14, σ_2=4.51×10^{-3}, σ_3=8×10^{-7}.	38.26	0.6175
Difference		+87.0%	+11.76%

It can be observed from Table 6. 9 that an increase in thermal conductivity leads to a reduction (12.50%) in the surface ablation area and a significant increase (86.7%) in ablation depth. Since the extending of the thermal ablation in the through-the-thickness direction is mainly related to the thermal conductivity in the through-the-thickness direction, it is therefore evident that the thermal ablation depth is very sensitive to the k_3.

Table 6. 10 shows that the decrease of the σ_1 leads to a slight increase in surface ablation area (6.19%) and ablation depth (5.88%), it is evident that the effects of the longitudinal electrical conductivity are not quite significant. The effect of the through-the-thickness electrical conductivity is shown in Table 6. 11. It can be noticed that the decrease of σ_3 leads to a significant increase in surface ablation area (87.00%) and a noticeable increase in ablation depth (11.76%). It is therefore evident that the extending of surface ablation area is very sensitive to σ_3, while the extending of the ablation depth is very sensitive to k_3 (see Table 6. 9). Therefore, obtaining accurate directional temperature-dependent electrical and thermal conductivities of the CFRP composite is critical for the prediction of thermal ablations.

6.5.2 Comparisons of the Proposed Element Deletion Method with Other Methods Used in the Literature

Finite element analysis has been performed using the proposed solution procedure with the element deletion method (described in Sections 5.3 and 6.4). During the FEA, the elements are deleted automatically and progressively once the material temperature exceeds the sublimation temperature of carbon fiber (3316 °C). The lightning-strike-induced electric current and surface heat flux boundary conditions (6-4) are also updated accordingly after the elements are removed. The deleted elements represent the ablated material and enable the prediction of the progressive shape change in the CFRP composite panel due to thermal ablation.

To investigate the differences between the predictions of thermal ablation using our proposed solution procedure and using the existing solution procedures by Ogasawara et al. (2010) and Abdelal & Murphy (2014), additional FEA attempts have been undertaken to predict the thermal ablation in the CFRP composite laminated panel using the solution procedures proposed by Ogasawara et al. (2010) and Abdelal et al. (2014). The case using the solution procedure by Ogasawara et al. (2010) is denoted as the "Ogasawara Method," in which a virtual latent heat (1×10^{11} J/kg) was introduced to limit the maximum temperature to 3316 °C. The case using the solution procedure by Abdelal & Murphy (2014) is denoted as the "Abdelal Method," in which the electrical conductivity in the through-the-thickness direction of the CFRP composite laminated panel was assumed to increase to 2 S/mm between 343 °C and 500 °C and increase from 2 S/mm to 1×10^{6} S/mm when the temperature > 3316 °C. In addition to these two cases, we have performed another FEA case using the Plain Heat Transfer Method (described in Section 6.5.1). The case using our proposed solution procedure with the element deletion method is denoted as the "Element Deletion Method."

In this section, the thermal conductivity reported by Griffis et al. (1986) (see Table 6. 2) and the "Elec. Cond. obtained using activation energy values by Sauder et al. (2002)" (see Table 6. 7) are used in all FEA cases. The duration of the lightning channel expansion (see equation (6-12)) used in all FEA cases is t_r=50 μs. In addition, continuing lightning current (6-12) is applied to the CFRP composite panel in all FEA cases.

The predicted radius of the thermal ablation area on the surface of the composite laminated panel and the depths of the thermal ablation in the center of the composite panel from the four FEA cases are tabulated in Table 6. 12. It should be noted that the FEA case using the Abdelal Method aborted due to numerical convergence issues.

Table 6. 12: Predicted radius of surface ablation area and depth of thermal ablation using various methods.

Case	Max. Surface Ablation Radius (mm)	Max. Ablation Depth (mm)
Element Deletion Method	12.04	1.02
Ogasawara Method	18.59	0.021
Abdelal Method	Analysis Aborted	Analysis Aborted
Plain Heat Transfer Method	18.60	0.42

Figure 6. 6 illustrates the temperature distributions along the x-direction at y=0 and z=0 (i.e., the red curve in the CFRP composite panel in Figure 6. 6) at the end of the step obtained from the Plain Heat Transfer Method. As one can see, without proper numerical treatment, the lightning current results in an unrealistically high temperature in the CFRP composite panel, up to 170000 °C. In contrast, the maximum temperature for the Element Deletion Method case and the Ogasawara Method case is limited to 3316 °C, as is shown in Figure 6. 7.

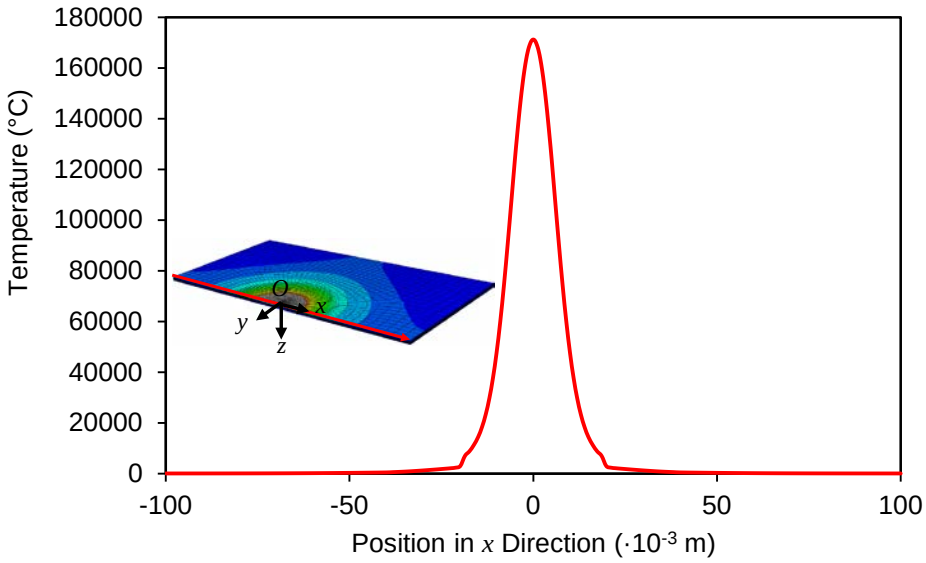

Figure 6. 6: Temperature distributions at t=0.468 s in the x-direction at y=0 and z=0 of the composite panel obtained using Plain Heat Transfer Method.

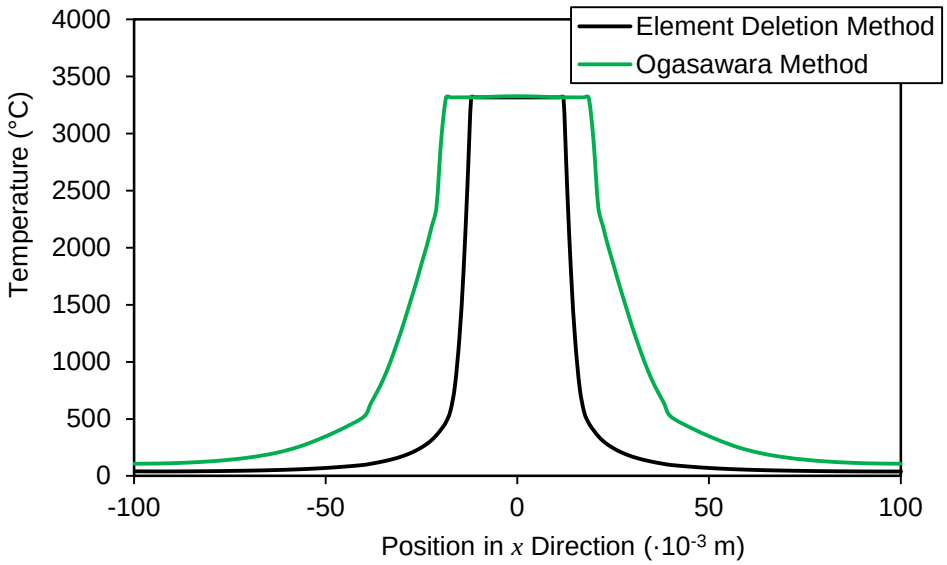

Figure 6. 7: Comparison of Temperature distributions at t=0.468 s in the x-direction at y=0 and z=0 of the composite panel between Element Deletion Method and Ogasawara Method.

The ablation depth history in the center (i.e., the origin of the coordinate) of the composite panel obtained from different FEA cases is plotted in Figure 6. 8. The composite layers are denoted by “L” and the number of the layer. For example, “L1” denotes layer 1. It is clearly observed from Figure 6. 8 that the ablation predicted from the Plain Heat Transfer Method case reaches only to the third layer, which is much smaller than the ablation predicted from the case using the Element Deletion Method, for which the ablation reaches to the eighth layer. However, when compared to the depth of ablation predicted from both the Element Deletion Method case and the Plain Heat Transfer case, the prediction from the Ogasawara Method case is significantly lower, for which even the first layer (i.e., thickness of the first layer is 0.195 mm) is not completely ablated. This significant under-prediction is due to the introduction of virtual latent heat using the Ogasawara Method case, which prevents the subsequent laminate layers from absorbing further energy from the lightning current.

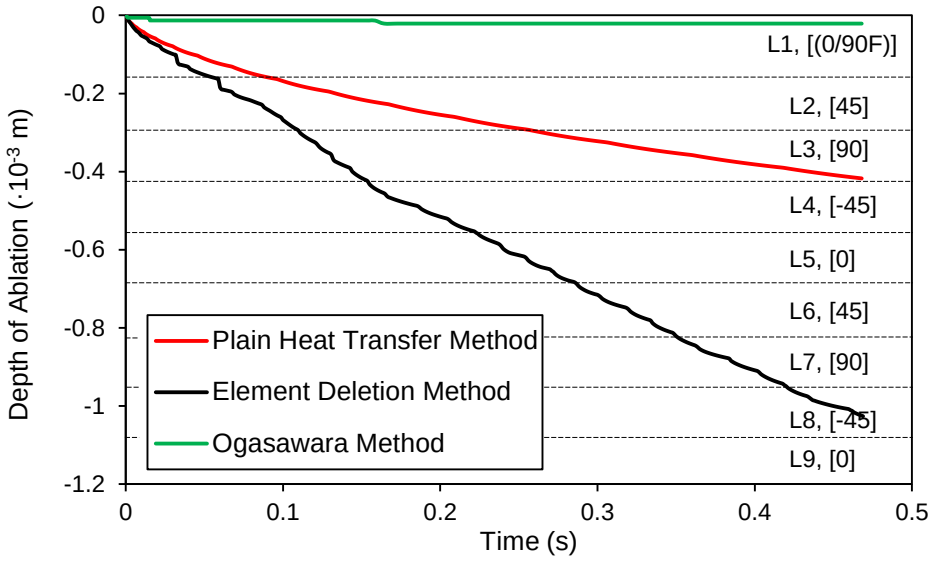

Figure 6. 8: Ablation depths in the center of the composite panel: comparison of the Element Deletion Method, Ogasawara Method, and Plain Heat Transfer Method.

The differences of the ablation depths in the center and the ablation profiles through the thickness of the CFRP composite panel at different times can be observed in Figure 6. 9. The ablation front for the Plain Heat Transfer case and the Ogasawara case are chosen as the boundary at which the temperature equals 3316 °C. As shown in Figure 6. 9, the prediction from the Plain Heat Transfer case and the Ogasawara case significantly underestimated the ablation profile in the through-the-thickness direction of the composite panel. The underestimation is due to the loss of energy dissipated in the material, for which the material is supposed to be removed due to continuous material sublimation. However, it is also interesting to find that the surface ablation areas exhibited from the Plain Heat Transfer case and the Ogasawara case are generally larger than the surface ablation area predicted from the case with the element deletion method. This is due to progressive element removal, which moves down the lightning-strike-induced electric current and surface heat flux boundary conditions continuously in the through-the-thickness direction. In cases without element deletion (i.e., the Plain Heat Transfer case and the Ogasawara case), the lightning-strike-induced electric current and surface heat flux boundary conditions remain on the top surface of the composite panel, which results in a larger ablation area in the in-plane direction. The growth of the ablation area on the surface of the composite panel is demonstrated in Figure 6. 10. The ablation area on the surface of the CFRP composite panel rapidly expands in the beginning of the lightning discharge and quickly reaches a steady state after 0.1 s, unlike the ablation in the through-the-thickness direction of the composite panel, which continuously develops, as shown in Figure 6. 8 and Figure 6. 9.

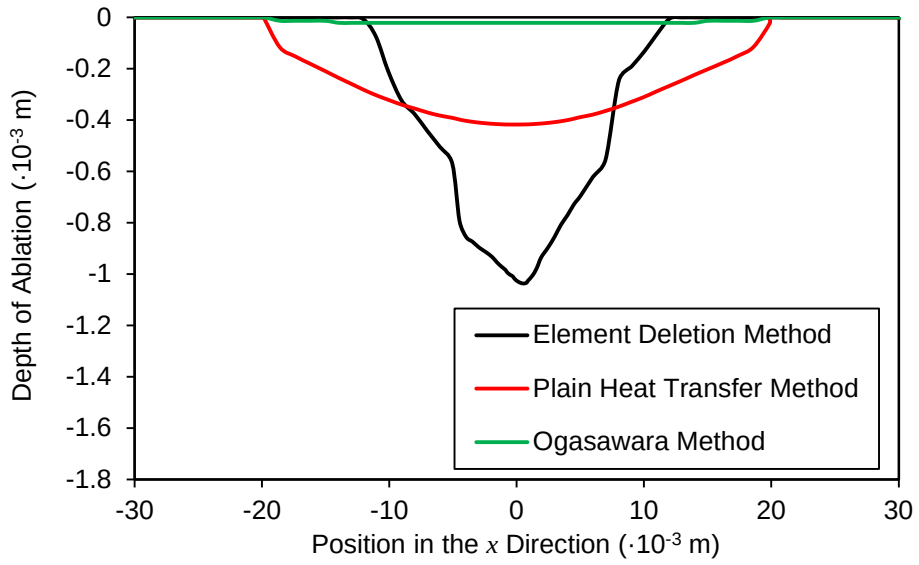

Figure 6. 9: Ablation profiles at t=0.468 s along the x-direction at y=0 of the composite panel: comparison of the Element Deletion Method, Ogasawara Method, and Plain Heat Transfer Method.

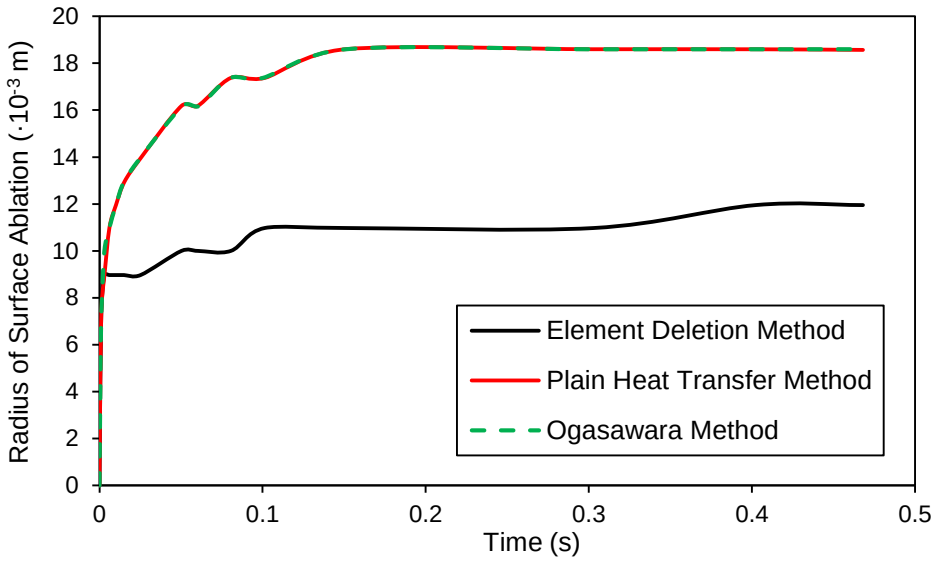

Figure 6. 10: Radius of the surface ablation area of the composite panel: comparison of the Element Deletion Method, Ogasawara Method, and Plain Heat Transfer Method.

The differences of the temperature distributions and the ablation zones at the end of the step between the predictions from the Element Deletion Method case and the Plain Heat Transfer Method case are plotted in the contour plot, Figure 6. 11. The ablation zone for the Plain Heat Transfer Method case (Figure 6. 11(a)) is shown by hiding the elements whose temperature exceed 3316 °C at the end of the FEA, while the ablation zone for the case using the proposed element deletion method (Figure 6. 11(b)) is obtained by removing elements progressively during the FEA. It can be clearly observed that the ablation predicted by the element deletion method is much deeper than the ablation predicted without element deletion, whereas the radius of the surface ablation zone is smaller than the prediction without element deletion.

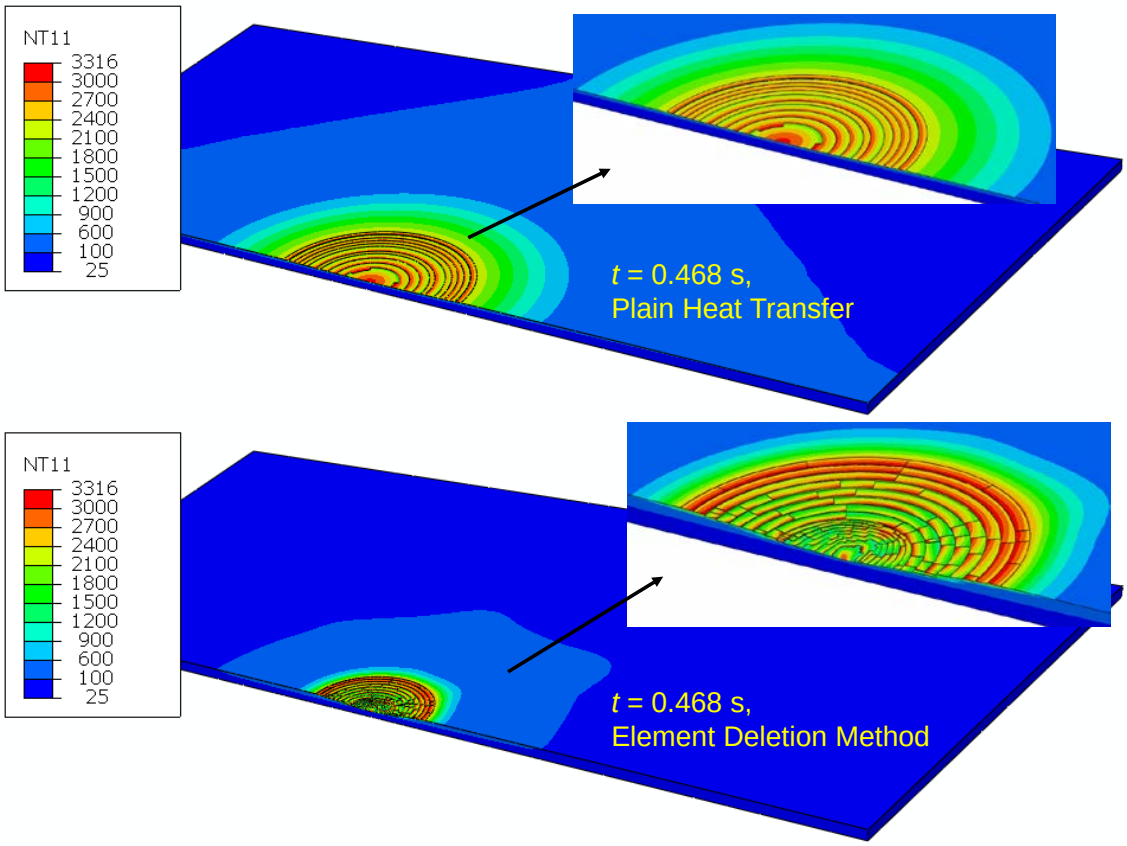

Figure 6. 11: Ablation profiles along the *x*-direction at *y*=0 of the composite panel: comparison between the Element Deletion Method case and the Plain Heat Transfer Method case.

6.5.3 Model Validation with Reported Experimental Results

Lightning strike experimental tests on the CFRP composite laminated panel were reported in the NASA's study (Salah et al., 2013). Artificial pulsed lightning current (component D) and continuing lightning current (component C) are generated in laboratory conditions and are sequentially applied to the CFRP composite laminated substrates (Salah et al., 2013). The specific lightning current waveform parameters used

in the experimental tests are shown in Figure 6. 12 and in Table 5. In our simulation study, the thermal ablation due to the pulsed lightning current is not considered, and only the thermal ablation due to the continuing lightning current is predicted. Such choice of simulation is due to the extreme short duration of the pulsed current and the extreme small thermal ablation induced by the pulsed current (Y. Wang & Zhupanska, 2015).

The radius of the laboratory-generated artificial lightning spark channel was not mentioned in the experimental study (Salah et al., 2013). In the present computational study, it is assumed that the duration of the lightning channel expansion (see equation (6-12)) is t_r=50 μs. Using equation (6-12), the constant radius of the lightning arc channel during the lightning current component C waveform is calculated as R=18.87 mm.

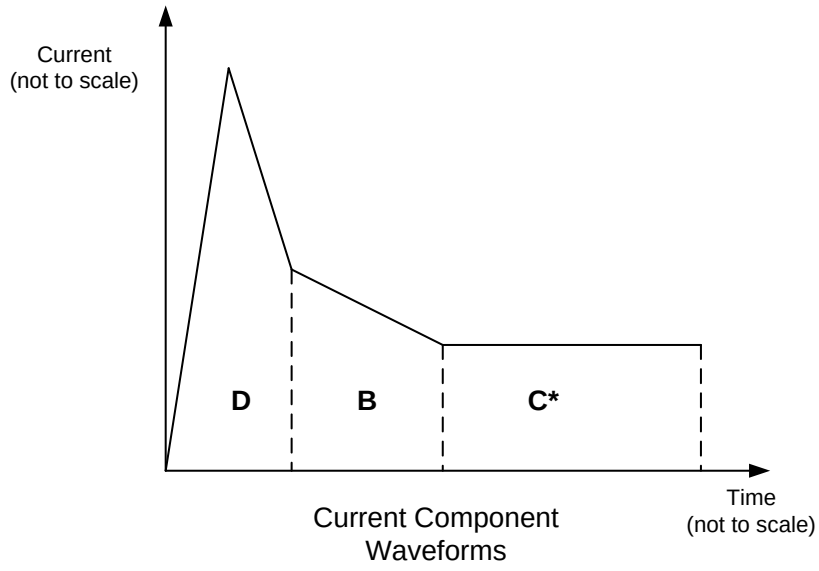

Figure 6. 12: Lightning current waveform used in NASA experimental study (Salah et al., 2013).

Table 6. 13: Lightning current waveforms parameters used in the experimental study (Salah et al., 2013).

Component A	Component B	Component C			Component D	
Not Applied	Not Applied	A	ms	coul	kA	$\times 10^6$ $A^2 \cdot s$
		368	468	172	20.80	0.220

It should be mentioned that at this point, we still lack confidence in deciding which set of electrical and thermal conductivities discussed in Sections 6.3.2 and 6.3.4 represent the true properties for the CFRP composites. Therefore, we performed two FEA cases: the first FEA case (Case 1 hereinafter) uses the thermal conductivity reported by Griffis et al. (1986) (see Table 6. 2) and the "Elec. Cond. obtained using activation energy values by Sauder et al. (2002)" (see Table 6. 7); whereas the second FEA case (Case 2 hereinafter) uses the thermal conductivity reported by Abdelal & Murphy (2014) (see Table 6. 3) and the "Elec. Cond. obtained using activation energy values by Takahashi & Hahn (2011)" (see Table 6. 7), as well as a modified duration of lightning channel expansion, t_r=220 μs (and therefore a modified lightning channel radius R=40 mm using (4-6)). The modified duration of lightning channel expansion is chosen as it has been reported that the pressure within the lightning channel drops to an ambient pressure within the first 200 μs of a typical pulsed lightning discharge (Chemartin et al., 2012). As can be seen in Figure 6. 13, for a pulsed lightning discharge with peak current of 100 kA and rise time of 5 μs, the radius of the lightning-induced pressure-affected zone reached to almost 150 mm when the pressure drops to the ambient pressure at approximately 200 μs.

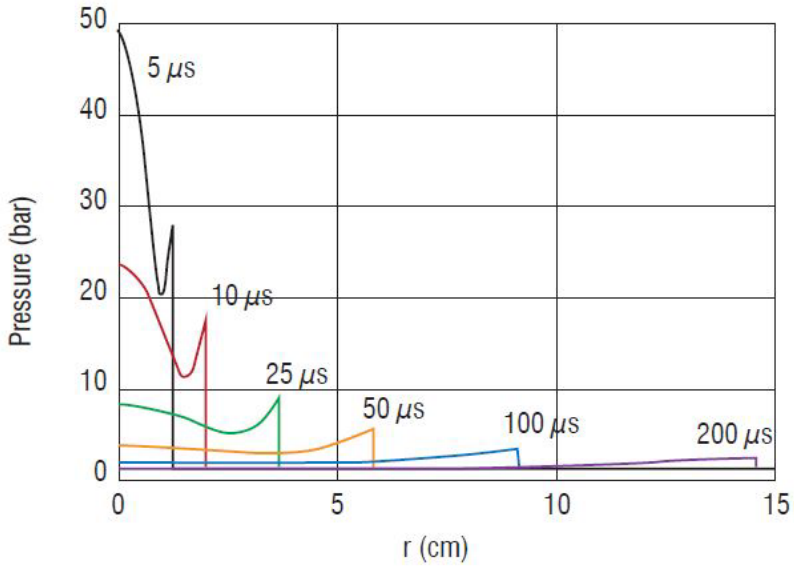

Figure 6. 13: Evolution of pressure within a lightning channel during its initial pulsed lightning discharge (peak current 100 kA, rise time 5 μs).

Source: Chemartin et al. (2012). *AerospaceLab*(5), p-1.

6.5.3.1 FEA Results for Case 1

Finite element analysis is performed using the proposed computational procedure described in Sections 5.3 and 6.4 for case 1. Figure 6. 14 shows that the lightning-induced thermal ablation in the center of the CFRP composite laminate panel (at the origin of the coordinate system; see Figure 6. 17) starts at approximately t=0.000863 s. The depth of thermal ablation shows an approximate linear relationship to time. At the end of the step, t=0.468 s, the ablation front reaches 1.02 mm, which is within layer 8 of the CFRP composite laminate panel. Figure 6. 15 illustrates the thermal ablation profile in the center (plane y=0; see Figure 6. 17) of the CFRP composite laminate at t=0.150 s, t=0.300 s, and t=0.468 s. The maximum thermal ablation depths corresponding to t=0.150 s, t=0.300 s, and t=0.468 s are 0.41 mm, 0.72 mm and 1.02 mm, respectively. As one can see, seven CFRP composite laminate layers are completely consumed. In addition, the

radius of the thermal ablation area on the surface of the CFRP composite laminate panel reaches 13 mm at the end of the step, t=0.468 s. Furthermore, the temperature profiles through the thickness direction in the center of the CFRP composite laminate panel at t=0.150 s, t=0.300 s and t=0.468 s are plotted in Figure 6. 16. It is evident that the temperature dropped rapidly in the through-the-thickness direction. Figure 6. 17 shows the temperature contour and thermal ablation profile at t=0.150 s and t=0.468 s. It is evident that the thermal ablation profile is not symmetric about the y-axis (see Figure 6. 17), which is due to the directional preference of those [45] and [-45] lamina layers.

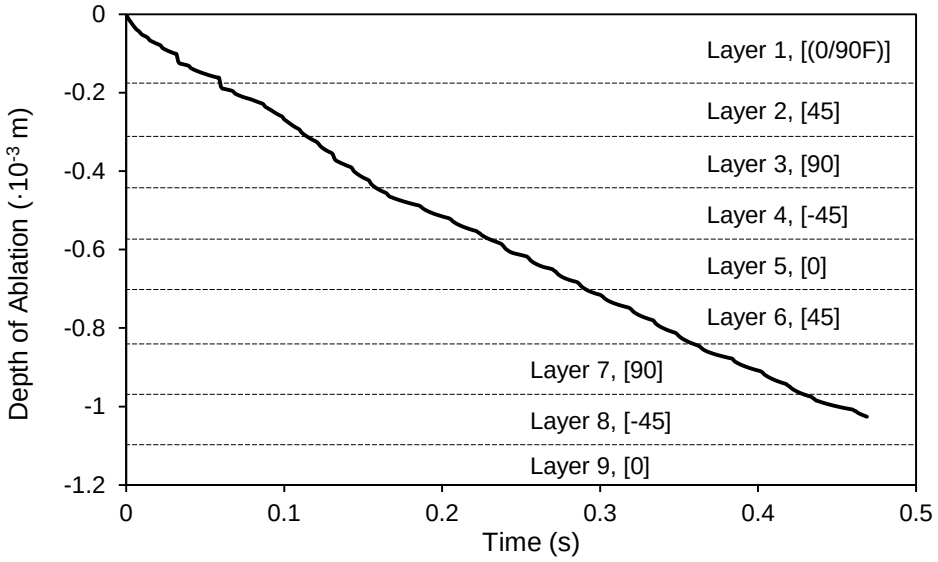

Figure 6. 14: Ablation depth vs. time in the center of the plane (at the origin of the coordinate) due to the continuing lightning current component C using the developed computational procedure for case 1.

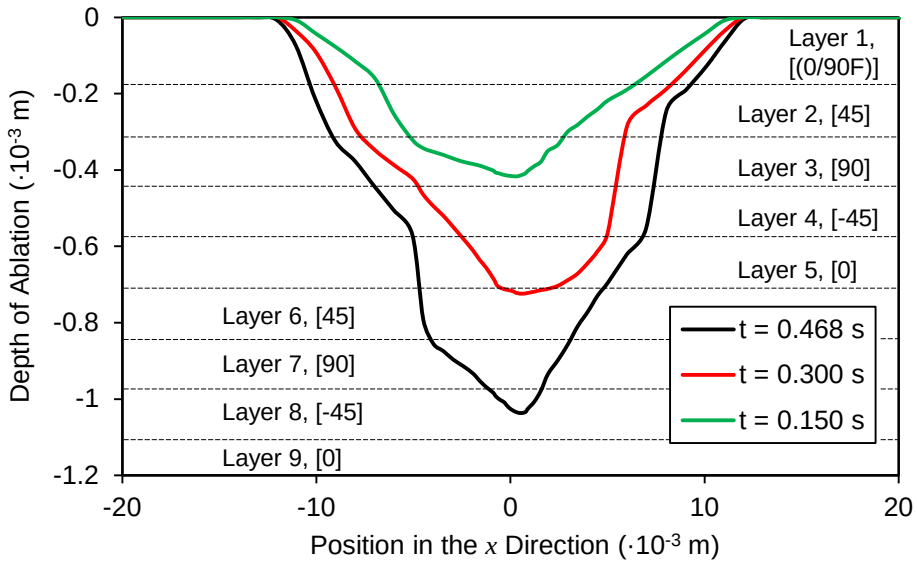

Figure 6. 15: Ablation zone profile in the y=0 plane, at t=0.150 s, t=0.300 s, and t=0.468 s due to continuing lightning current component C using the developed computational procedure for case 1.

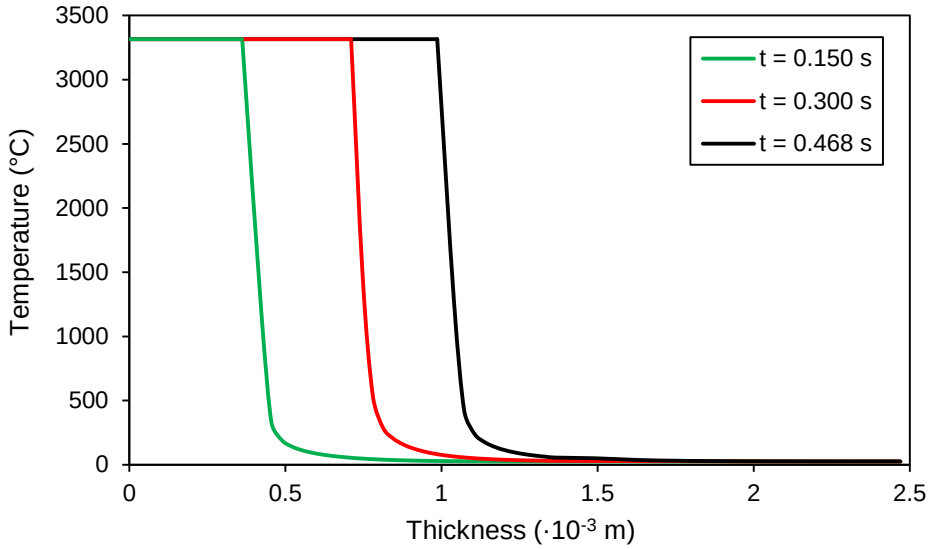

Figure 6. 16: Temperature in through-the-thickness direction in the center of the panel, at t=0.150 s, t=0.300 s, and t=0.468 s due to continuing lightning current component C using the developed computational procedure for case 1.

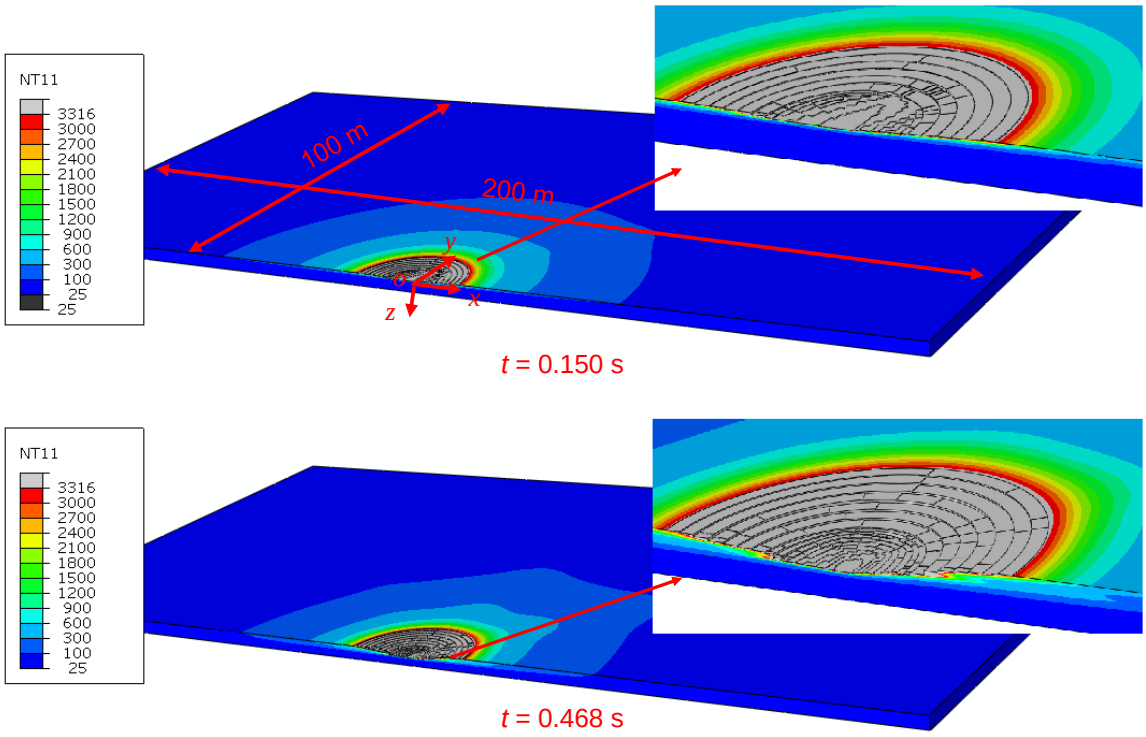

Figure 6. 17: Temperature contour plots and thermal ablation profiles in the CFRP composite laminate panel at t=0.150 s and t=0.468 s due to continuing lightning current component C using the developed computational procedure for case 1.

6.5.3.2 FEA Results for Case 2

It is worth mentioning again that the electrical and thermal conductivities of CFRP composites used in Case 2 are different from those used in Case 1. In Case 2, the thermal conductivity reported by Abdelal & Murphy (2014) (see Table 6. 3) and the "Elec. Cond. obtained using activation energy values by Takahashi & Hahn (2011)" (see Table 6. 7) are used. In addition, the duration of the lightning channel expansion is modified to t_r=220 μs, which therefore also results in a modified lightning channel radius R=40 mm.

Figure 6. 18 shows the depth of ablation versus time in the center of the CFRP composite laminated panel. As one can see, the ablation depth reaches 0.97 mm due to the continuing lightning current strike. Seven laminated layers are completely ablated. Figure 6. 19 illustrates the ablation zone profile in the center (plane y=0; see Figure 6. 17) of the CFRP composite laminated panel. It can be observed in Figure 6. 19 that two laminated layers, four and half laminated layers, and seven laminated layers are ablated at t=0.150 s, t=0.300 s, and t=0.468 s, respectively. The maximum radius of the surface ablation area on the CFRP composite panel is 21 mm as shown in Figure 6. 19 and Figure 6. 21. The temperature distributions in the through-the-thickness direction in the center of the composite panel at t=0.150 s, t=0.300 s, and t=0.468 s are shown in Figure 6. 20. As one can see, the temperature undergoes a rapid temperature drop in the through-the-thickness direction. Figure 6. 21 shows the comparison between the radius of surface ablation obtained from FEA Case 1 and FEA Case 2.

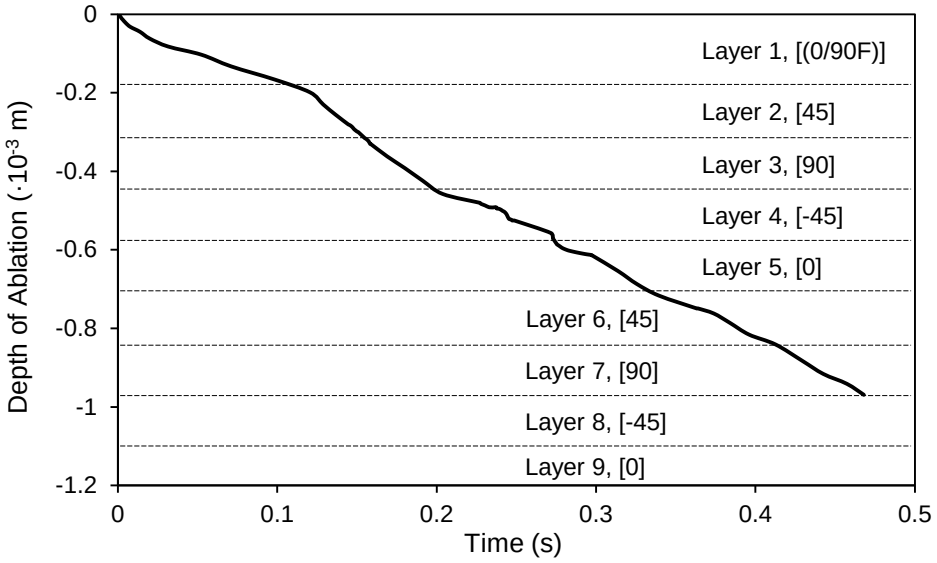

Figure 6. 18: Ablation depth vs. time in the center of the plane (at the origin of the coordinate) due to the continuing lightning current component C using the developed computational procedure for case 2.

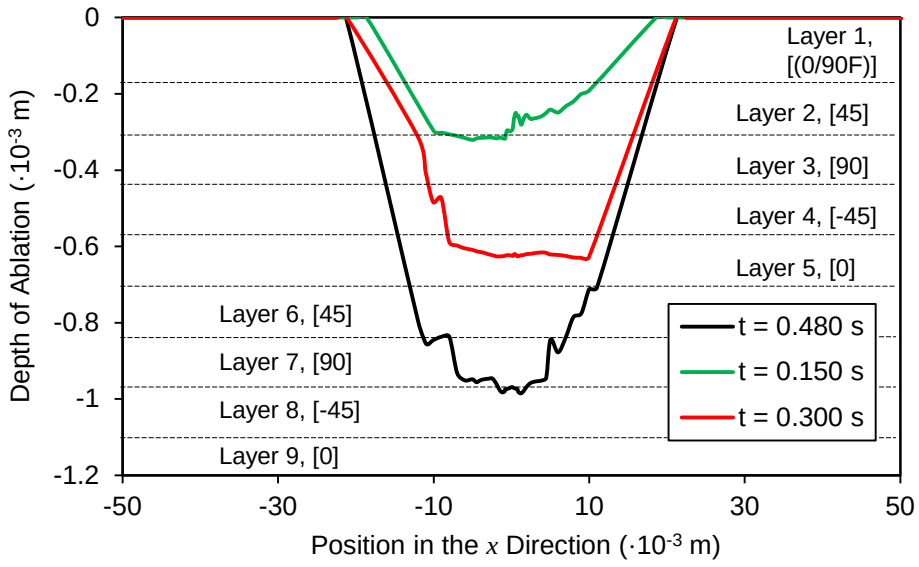

Figure 6. 19: Ablation zone profile in the y=0 plane, at t=0.150 s, t=0.300 s, and t=0.468 s, due to continuing lightning current component C using the developed computational procedure for case 2.

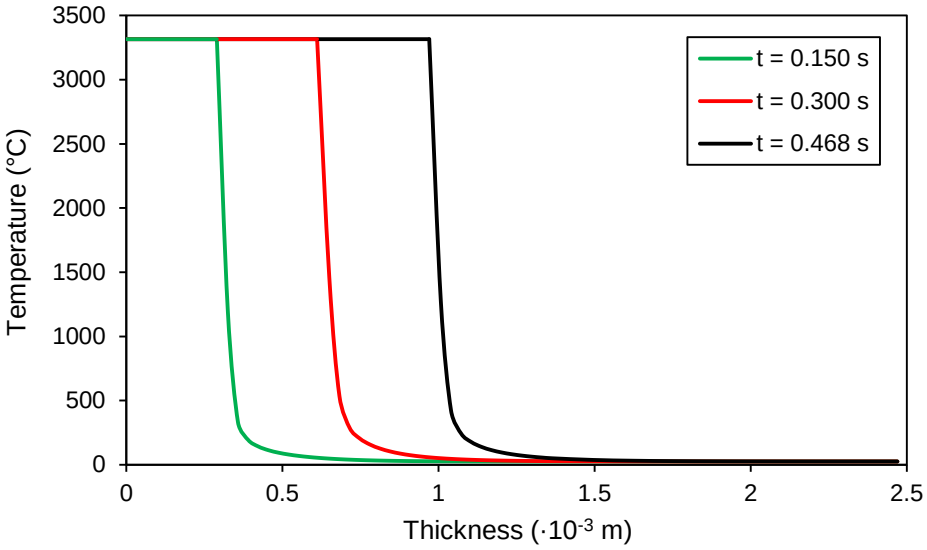

Figure 6. 20: Temperature in through-the-thickness direction in the center of the panel, at t=0.150 s, t=0.300 s, and t=0.468 s, due to continuing lightning current component C using the developed computational procedure for case 2.

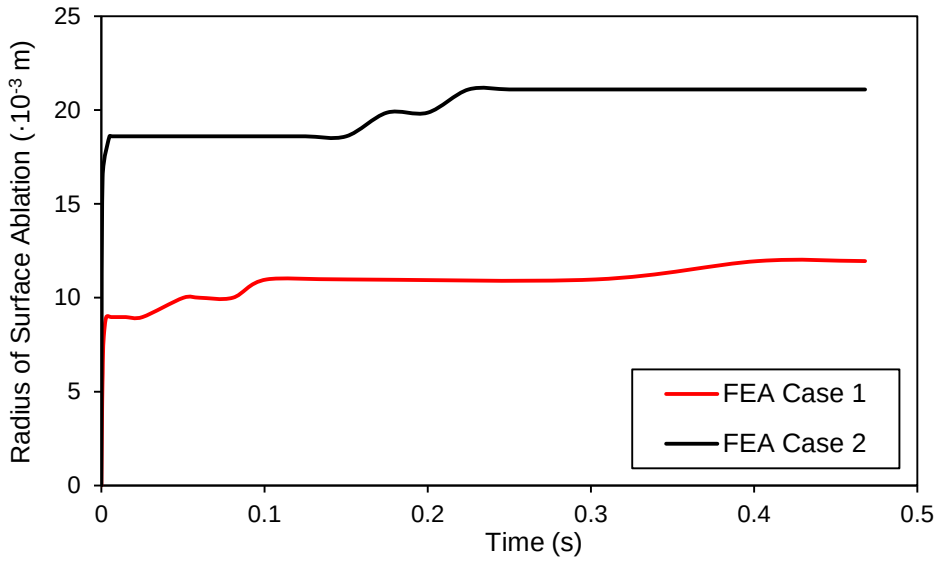

Figure 6. 21: Radius of the surface ablation area of the composite panel: comparison between FEA Case 1 and Case 2.

6.5.3.3 Comparison of FEA Results with Reported Experimental Results

In the reported experimental tests (Salah et al., 2013), the lightning-induced damage area on the surface of the CFRP composite laminate panel was inspected using the Through Transmission Ultrasonic (TTU) C-scan (Salah et al., 2013). The C-scan image (Figure 6. 22) shows a damage area of 2.558 in^2 (1650 mm^2) at the top surface of the composite panel (Salah et al., 2013). The radius of the damaged area is 23 mm (Salah et al., 2013). The predicted ablation zone (temperature > 3316 °C, corresponding elements are deleted), charred zone (temperature > 1800 °C), and resin decomposed zone (temperature > 300 °C) on the surface of the CFRP composite panel from FEA Case 2 are compared with the damaged area from experimental data (Salah et al., 2013), shown in Figure 6. 22. As it can be observed, the predicted damage zones agree well with the reported experimental results.

In addition, the depth of the lightning-induced damage in the CFRP composite laminated panel was inspected using the Pulse Echo Unit test (show in Figure 6. 23) (Salah et al., 2013). It can be observed that the maximum damage depth is 0.04 in (1.016 mm). The predicted depth of ablation in the center of the CFRP composite panel from FEA Case 2 is compared with the experimental data in Figure 6. 23. As one can see, the predicted maximum depth of ablation is 0.97 mm, which is slightly lower than the reported experimental data (1.016 mm). The small difference between the prediction from FEA Case 2 (0.97 mm) and the reported experimental data (1.016 mm) is attributed to the pulsed lightning current, which was applied in the experimental test but was not included in the FEA.

Table 6. 14 tabulates the comparisons of the surface ablation areas and the ablation depths between the predictions from the two FEA cases and the reported experimental results (Salah et al., 2013).

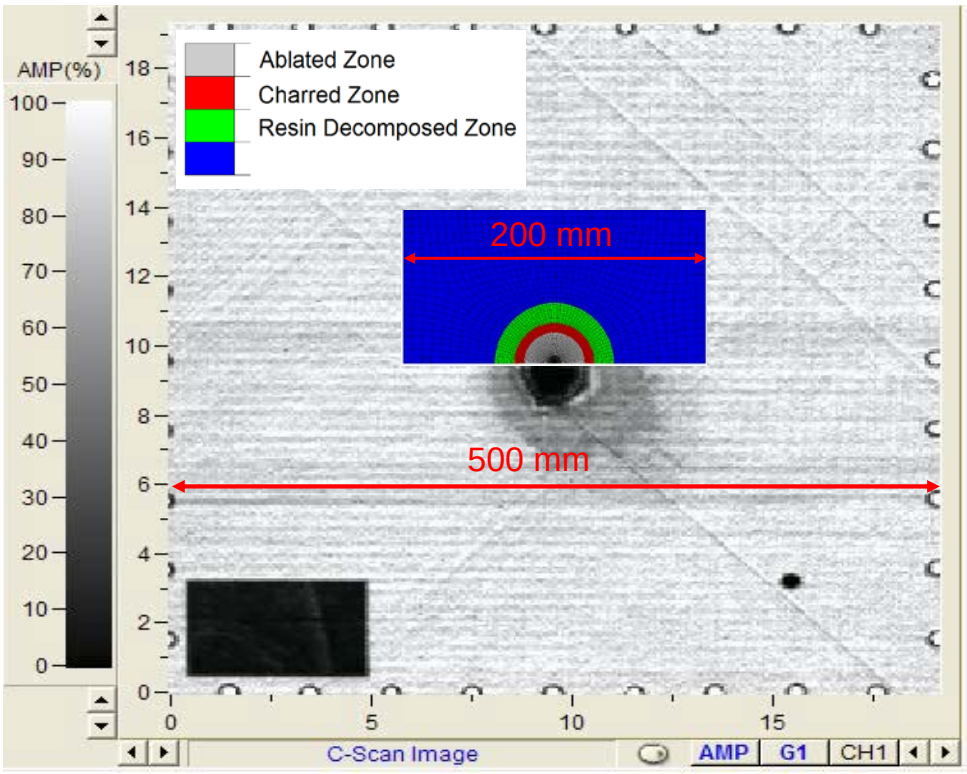

Figure 6. 22: Damage area on the CFRP composite laminate top surface: comparison between experimental data (Through Transmission Ultrasonic (TTU) C-scan) reported in Salah et al., (2013) and predicted surface damage area from FEA Case 2.

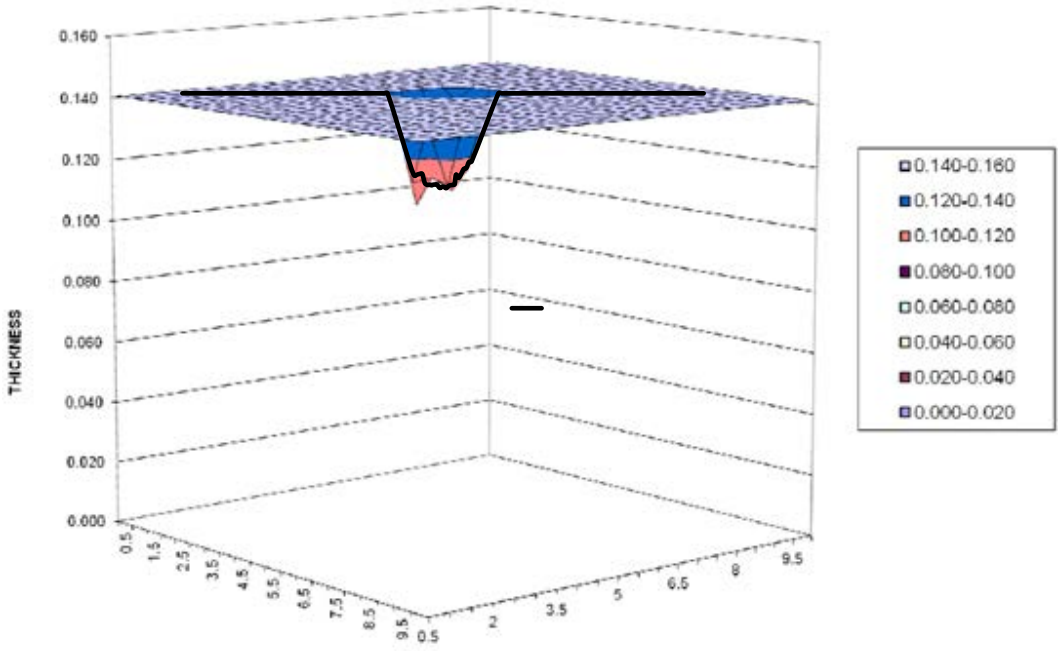

Figure 6. 23: Lightning-induced damage depth in CFRP composite substrate: comparison between experimental results (by Pulse Echo Unit) reported in Salah et al. (2013) and predicted ablation depth from FEA Case 2.

Table 6. 14: Comparison of predicted thermal ablations from the two FEA cases with experimental results (Salah et al., 2013).

Case	FEA Case 1	FEA Case 2	Experimental Results (Salah et al., 2013)
Max. Surface Ablation Radius (mm)	13	21	23
Max. Ablation Depth (mm)	1.02	0.97	1.016

As one can notice from Table 6. 14, the predicted surface ablation area and the depth of thermal ablation from FEA Case 2 show good agreement with the reported experimental results (Salah et al., 2013), whereas the predictions from FEA case 1 underestimated the extending of ablation area on the surface of the CFRP composite laminated panel. The results also adversely suggest that the thermal conductivity of CFRP composites reported by Abdelal & Murphy (2014) (see Table 6. 3) and the "Elec. Cond. obtained using activation energy values by Takahashi & Hahn (2011)" (see Table 6. 7) present better representations of the true material properties of the CFRP composite laminated panel used in the current thesis.

CHAPTER 7
CONCLUSIONS

In this thesis, the thermal interaction between lightning strike and the fiber-reinforced polymer-matrix composite structure is studied. Lightning strike leads to direct heat injection at the attached spot as well as production of Joule heating due to the lightning current conduction through the electrically conductive composite structure. For an electrically non-conductive composite structures (i.e., a wind turbine blade), Joule heating is produced only when the strength of the lightning-induced electric field exceeds the dielectric breakdown strength.

To check whether dielectric breakdown occurs on the non-conductive glass-fiber-reinforced polymer-matrix (GFRP) composite wind turbine blade, finite element analysis with COMSOL has been carried out to calculate the electric field along three GFRP composite SNL100-00 wind turbine blade due to a lightning stepped leader. The non-uniform charge density of the lightning stepped leader and the effects of receptors and down conductors on the wind turbine blade have been taken into consideration. The predicted electric field has been compared to the dielectric breakdown strength of the GFRP composite wind turbine blade. Results show that the tip of the vertical blade (blade *OA* in Figure 3. 9) has the highest risk of experiencing dielectric breakdown with a safety factor (ratio between dielectric breakdown strength and predicted electric field strength) as low as 1.52 due to a lightning protection level (LPL) I lightning stepped leader.

To predict the thermal response and thermal ablation in the composite structure due to lightning strike, a physics-based model has been developed. The model includes: (i) spatial and temporal evolution of the lightning channel as a function of the lightning current; (ii) temporary and spatially non-uniform heat flux generated at the composite structure, where the heat flux is an explicit function of the lightning current and the

instant lightning channel radius; and (iii) a nonlinear transient heat transfer problem formulation for layered anisotropic composites that includes the moving boundary of the expanding lightning channel and the phase transition moving boundary associated with instantaneous material removal due to sublimation.

Two numerical methods have been developed in this work to solve the nonlinear transient heat transfer problem with moving boundary conditions (see Sections 5.3 and 6.4). The first is the Umeshmotion+ALE method, and the second is the element deletion method. The Umeshmotion+ALE method is not able to handle problems with multiple material domains and is not to be used in the case of conductive carbon-fiber-reinforced polymer-matrix (CFRP) composites in which Joule heating is involved. The element deletion method is more complicated but is free from problems with multiple material domains and can be used in the case of CFRP composites; thus, it is more general.

The thermal response and thermal ablation in the tip composite panel of the Sandia 100-meter All-glass baseline wind turbine blade (SNL 100-00) have been predicted due to two different lightning current waveforms: (i) pulsed lightning current (component A), and (ii) continuing current (component C). Joule heating has been excluded from the model, because it was shown in Section 3 that if the effects of humidity on the dielectric properties of the GFRP composite are not considered, a lightning stepped leader up to 200 kA will not lead to immediate dielectric breakdown in the GFRP composite wind turbine blade. The directional temperature-dependent thermal properties of the GFRP composite laminates used for the wind turbine blade have been determined based on existing experimental results and micromechanics considerations. Three different LPLs as suggested by IEC-61400-24 (IEC-61400-24, 2002) have been considered.

Results showed that the thermal ablation due to pulsed lightning current was insignificant. The Umeshmotion+ALE method has proven to be adequate to solve the case with pulsed lightning current for which the ablation depth was smaller than 1/20 of

the layer 1 (see Table 5. 1 and Figure 5. 13) and was still far from the material interface between the woven (layer 1) and the unidirectional layers (layer 2). However, the Umeshmotion+ALE method was found to be inadequate to solve the case with continuing lightning current as the thermal ablation in the CFRP composite produced by the continuing lightning current was sufficiently deep to cross the material inference between layer 1 and layer 2 (see Figure 5. 15). Therefore, the element deletion method (describe in Sections 5.3 and 6.4) has been used instead to solve the LPL cases with continuing lightning current. Results show that the maximum depth of ablation produced by the continuing lightning current reached 5.13 mm for the extreme case LPL I and that two laminate layers have been completely consumed.

In addition, the thermal response and thermal ablation in a conductive CFRP laminated composite panel have been predicted. The CFRP laminated composite panel was chosen as the CFRP composite substrate in the experimental study by NASA (Salah et al., 2013) to enable the model validation with the reported experimental measurements (Salah et al., 2013). An overview of directional electrical conductivity of CFRP composites used in the existing literature has been presented. The directional electrical properties of the CFRP composite laminates from room temperature to the sublimation temperature of carbon fibers have been determined using existing experimental data and micromechanics considerations. The problem formulation and the proposed element deletion method for non-conductive GFRP composite have been modified to take into account the Joule heating effects for conductive CFRP composite. The effects of directional thermal and electrical conductivity on the thermal ablation in the CFRP composites due to continuing lightning current have been investigated. The results showed that the extending of the surface ablation area is very sensitive to σ_3, while the extending of the ablation depth is very sensitive to k_3 (see Section 6.5.1). In addition, the thermal ablation predicted using the proposed element deletion method has been compared to the thermal ablation predicted using traditional numerical techniques

proposed in the existing literature. The results showed that traditional numerical techniques are not capable of modeling progressive thermal ablation and generally under-predict thermal ablations in the CFRP composites (see Section 6.5.2). Finally, the numerical results using the element deletion method have been compared to the reported experimental measurements (Salah et al., 2013). It was found that the predicted thermal ablation (i.e., surface ablation area and ablation depth) agree well with those reported in the experimental study (Salah et al., 2013), which therefore proves the effectiveness of the developed numerical procedure with element deletion method (see Section 6.5.3).

APPENDIX

A.1 DFLUX User-subroutine

The DFLUX user-subroutine is used to describe both the lightning arc channel heat flux time and spatial evolution (see Sections 5.3 and 6.4 for details).

```
      SUBROUTINE DFLUX(FLUX,SOL,KSTEP,KINC,TIME,NOEL,NPT,
     1 COORDS,JLTYP,TEMP,PRESS,SNAME)
C
C
      INCLUDE 'ABA_PARAM.INC'
C
      CHARACTER*8 CMNAME
C
C
      DIMENSION COORDS(3),FLUX(2),TIME(2)
      PARAMETER(PI=3.141593)
C
C     Coordinates Transformation
      x=COORDS(1)
      y=COORDS(2)
      z=COORDS(3)
C     Lightning Arc Channel Origin
      x1=0
      y1=0
C     Flux Type: Surface Flux
      JLTYP=0
C     Initial Radius of lightning channel (_m)
      r0=1.0E-3
C     Peak current of component A (_A)
      Ipeak=20.3E3
C     Radius expansion coefficient
      alpha=0.097
C     Decay Constant
      beta=10900
C     Duration of component A (_s)
      ta=500e-6
C     Linear Rise Time (_s)
      tm=10E-6
C     Duration of radius expansion (_s)
```

```
      tr=150e-6
C     Constant current of component C (_A)
      Ic=368
C     Duration of component C (_s)
      tc=468e-3
C     Current Value of Total Time (_s)
      T=Time(2)
C
C     radius expands during tr
      IF (T<=tr) THEN
      r=r0+alpha*((Ipeak)**(1.0/3))*(T**(1.0/2))
      ELSE
      r=r0+alpha*((Ipeak)**(1.0/3))*(tr**(1.0/2))
      END IF
C
C     Radius in mm
      r=r*1000
      b=-LOG(0.1)/((0.55*r)**2)
C
      IF (T<=tm) THEN
      I=Ipeak*(T/tm)
      J=b*I/(3.14159*(1-EXP(-b*r**2)))
      Qmax=10*J
      shape=exp(-b*(x-x1)**2-b*(y-y1)**2)
      FLUX(1)=Qmax*shape
      ELSE IF (T>tm .AND. T<ta) THEN
      I=Ipeak*EXP(-beta*(T-tm))
      J=b*I/(3.14159*(1-EXP(-b*r**2)))
      Qmax=10*J
      shape=exp(-b*(x-x1)**2-b*(y-y1)**2)
      FLUX(1)=Qmax*shape
      ELSE
      J=b*Ic/(3.14159*(1-EXP(-b*r**2)))
      Qmax=10*J
      shape=exp(-b*(x-x1)**2-b*(y-y1)**2)
      FLUX(1)=Qmax*shape
      END IF

      RETURN
      END
```

A.2 UMESHMOTION User-subroutine

The UMESHMOTION user-subroutine is used to define the motion of the nodes as a function of nodal temperatures (ABAQUS user subroutine reference manual, 2016; Lee, 2008). The motion of the nodes represents the shape change of the structure due to thermal ablation (see Umeshmotion+ALE method in Section 5.3).

```
      SUBROUTINE UMESHMOTION(UREF,ULOCAL,NODE,NNDOF,
           1  LNODETYPE,ALOCAL,NDIM,TIME,DTIME,PNEWDT,KSTEP,
           2  KINC,KMESHSWEEP,JMATYP,JGVBLOCK,LSMOOTH)
      C
            include 'ABA_PARAM.INC'
      C
            CHARACTER*80 PARTNAME
            DIMENSION ARRAY(100)
            DIMENSION ULOCAL(*)
            DIMENSION JGVBLOCK(*),JMATYP(*)
            DIMENSION ALOCAL(NDIM,*)
            PARAMETER (NELEMMAX=300000)
            DIMENSION JELEMLIST(NELEMMAX)
            DIMENSION JELEMTYPE(NELEMMAX)

            LOCNUM = 0
            JRCD = 0
            PARTNAME = ' '
            CHARLENGTH = UREF
            JTYP = 1

            ndt1 = NODE
            ndx1 = NODE
      C number “1057” and “79275” need to be changed
      C corresponding to your own mesh
            ndt2 = ndt1 + 1057
            ndx2 = ndx1 + 1057
            ltrn = 0
      c
            if (ndt2 .lt. 79275) then
            call GETVRN(ndt1,'NT',array,jrcd,JGVBLOCK,ltrn)
            tmp1 = array(1)
          call GETVRN(ndx1,'COORD',array,jrcd,JGVBLOCK,ltrn)
            crd1 = array(2)
            call GETVRN(ndt2,'NT',array,jrcd,JGVBLOCK,ltrn)
```

```
            tmp2 = array(1)
           call GETVRN(ndx2,'COORD',array,jrcd,JGVBLOCK,ltrn)
            crd2 = array(2)
      c number “1100” is the ablation temperature
            if (tmp1 .gt. 1100.0) then
            xxx = (tmp1 + tmp2 - 2*1100)/(tmp1 - tmp2)
            xx1 = (xxx + 1)*(crd1 - crd2)/2
            x1 = 0.0
            x2 = max(0.0,xx1)
            x3 = 0.0
            else
            x1 = 0.0
            x2 = 0.0
            x3 = 0.0
            end if
      c
ULOCAL(1) = ULOCAL(1) - ALOCAL(1,1)*x1 - ALOCAL(2,1)*x2
ULOCAL(2) = ULOCAL(2) - ALOCAL(1,2)*x1 - ALOCAL(2,2)*x2
      c
            LSMOOTH = 1
      c
            end if
            RETURN
            END
```

A.3 URDFIL User-subroutine

The URDFIL user-subroutine is used in the element deletion method (see Section 6.3 for details) to detect the nodal temperatures at each time increment and terminate the FEA analysis once the temperatures of the material exceed a designated ablation temperature.

```
      SUBROUTINE URDFIL(LSTOP,LOVRWRT,KSTEP,KINC,DTIME,TIME)
      C
            INCLUDE 'ABA_PARAM.INC'
      C
            DIMENSION ARRAY(513),JRRAY(NPRECD,513),TIME(2)
            EQUIVALENCE (ARRAY(1),JRRAY(1,1))
```

```
      PARAMETER(TOL=5000)
      REAL::Temp,NodeLabel

   OPEN(unit=16,file='/Dis-1-10.dat',status='unknown')
      LOVEWRT=1
C
C FIND CURRENT INCREMENT.
C
      CALL POSFIL(KSTEP,KINC,ARRAY,JRCD)
      DO K1=1,999999
         CALL DBFILE(0,ARRAY,JRCD)
         IF (JRCD .NE. 0) GO TO 110
            KEY=JRRAY(1,2)
C
C RECORD 201 CONTAINS VALUES FOR NT
C
            IF (KEY.EQ.201) THEN
                NodeLabel=JRRAY(1,3)
                Temp=ARRAY(4)
                WRITE(16,*)NodeLabel,Temp
                IF (Temp.GT.TOL) THEN
                 LSTOP=1
             GO TO 110
         END IF
         END IF
      END DO
 110  CONTINUE
C
      RETURN
      END
```

REFERENCES

ABAQUS user subroutine reference manual, ABAQUS 6.14 documentation

Abdelal, G., & Murphy, A. (2014). Nonlinear numerical modelling of lightning strike effect on composite panels with temperature dependent material properties. *Composite Structures, 109*, 268-278.

Ashwill, T. D., & Paquette, J. A. (2008). *Composite materials for innovative wind turbine blades.* Wind Energy Technology Department, Sandia National Laboratories, Albuquerque, NM 87185.

Bai, Y., & Keller, T. (2007). Modeling of post-fire stiffness of E-glass fiber-reinforced polyester composites. *Composites Part A: Applied Science and Manufacturing, 38*(10), 2142-2153.

Becerra, M. (2008). *On the attachment of lightning flashes to grounded structures.* PhD thesis, Acta Universitatis Upsaliensis.

Borovsky, J. E. (1998). Lightning energetics: Estimates of energy dissipation in channels, channel radii, and channel-heating risetimes. *Journal of Geophysical Research: Atmospheres (1984–2012), 103*(D10), 11537-11553.

Braginskii, S. I. (1958). Theory of the development of a spark channel. *SOVIET PHYSICS JETP-USSR, 7*(6), 1068-1074.

Brøndsted, P., Lilholt, H., & Lystrup, A. (2005). Composite materials for wind power turbine blades. *Annu. Rev. Mater. Res., 35*, 505-538.

Caldwell, J., & Kwan, Y. Y. (2004). Numerical methods for one-dimensional Stefan problems. *Communications in numerical methods in engineering, 20*(7), 535-545.

Cao, S., Zhis, W. U., & Wang, X. (2009). Tensile properties of CFRP and hybrid FRP composites at elevated temperatures. *Journal of composite materials, 43*(4), 315-330.

Chemartin, L., Lalande, P., Delalondre, C., Cheron, B., & Lago, F. (2011). Modelling and simulation of unsteady dc electric arcs and their interactions with electrodes. *Journal of Physics D: Applied Physics, 44*(19), 194003.

Chemartin, L., Lalande, P., Peyrou, B., Chazottes, A., Elias, P. Q., Delalondre, C., . . . Lago, F. (2012). Direct effects of lightning on aircraft structure: analysis of the thermal, electrical and mechanical constraints. *AerospaceLab*(5), p-1.

Cooray, V., & Rahman, M. (2005 19-23 September). *On the relationship between the discharge current, energy dissipation and the NOx production in spark discharges.* Paper presented at the International Conference on Lightning and Static Electricity, Seattle, USA

Cooray, V., Rakov, V., & Theethayi, N. (2007). The lightning striking distance—Revisited. *Journal of Electrostatics, 65*(5), 296-306.

D'Alessandro F, Petrov NI. (2006). *Field study on the interception efficiency of lightning protection systems and comparison with models*. In Proceedings of the Royal Society of London A: Mathematical, Physical and Engineering Sciences, 462(2069), 1365-1386. The Royal Society.

Dubovoy, E. I., Mikhailov, M. S., Ogonkov, A. L., & Pryazhinsky, V. I. (1995). Measurement and numerical modeling of radio sounding reflection from a lightning channel. *Journal of Geophysical Research: Atmospheres (1984–2012), 100*(D1), 1497-1502.

Eriksson AJ. (1979). *The lightning ground flash—an engineering study*. PhD thesis, University of Natal, Pretoria (CSIR Special Report ELEK 189).

Eriksson AJ. (1987). The incidence of lightning strikes to power lines. Power Delivery, *IEEE Transactions on, 2*(3), 859-870.

Fan, H. G., & Kovacevic, R. (2004). A unified model of transport phenomena in gas metal arc welding including electrode, arc plasma and molten pool. *Journal of Physics D: Applied Physics, 37*(18), 2531.

Feih, S., & Mouritz, A. P. (2012). Tensile properties of carbon fibres and carbon fibre–polymer composites in fire. *Composites Part A: Applied Science and Manufacturing, 43*(5), 765-772.

Feraboli, P., & Miller, M. (2009). Damage resistance and tolerance of carbon/epoxy composite coupons subjected to simulated lightning strike. *Composites Part A: Applied Science and Manufacturing, 40*(6), 954-967.

GCube. (n.d.). *Top 5 U.S. wind energy insurance claims*. Retrieved from http://www.gcube-insurance.com/en/press/gcube-top-5-us-wind-energy-insurance-claims-report/.

Golde, R. H. (1945). The frequency of occurrence and the distribution of lightning flashes to transmission lines. *Electrical Engineering, 64*(12), 902-910.

Golde, R. H. (1977). *Lightning* (Vol. 1): Academic Press London.

Gonzalez, J. J., Lago, F., Freton, P., Masquere, M., & Franceries, X. (2005). Numerical modelling of an electric arc and its interaction with the anode: part II. The three-dimensional model—influence of external forces on the arc column. *Journal of Physics D: Applied Physics, 38*(2), 306.

Gou, J., Tang, Y., Liang, F., Zhao, Z., Firsich, D., & Fielding, J. (2010). Carbon nanofiber paper for lightning strike protection of composite materials. *Composites Part B: Engineering, 41*(2), 192-198.

Griffis, C. A., Nemes, J. A., Stonesifer, F. R., & Chang, C. I. (1986). Degradation in Strength of Laminated Composites Subjected to Intense Heating and Mechanical Loading. *Journal of Composite Materials, 20*(3), 216-235.

Griffith, D. T., & Ashwill, T. D. (2011). *The Sandia 100-meter all-glass baseline wind turbine blade: SNL100-00.* Sandia National Laboratories, Albuquerque, SAND2011-3779.

Hill, R. D. (1971). Channel heating in return-stroke lightning. *Journal of Geophysical Research, 76*(3), 637-645.

Hill, R. D. (1977). Energy dissipation in lightning. *Journal of Geophysical Research, 82*(31), 4967-4968.

Hill, R. D. (1990). Lightning channel decay. *Physics of Fluids B: Plasma Physics (1989-1993), 2*(12), 3209-3211.

Hirano, Y., Katsumata, S., Iwahori, Y., & Todoroki, A. (2010). Artificial lightning testing on graphite/epoxy composite laminate. *Composites Part A: Applied Science and Manufacturing, 41*(10), 1461-1470.

Hong, T. P., Lesaint, O., & Gonon, P. (2009). Water absorption in a glass-mica-epoxy composite-[I: Influence on Electrical Properties]. *Dielectrics and Electrical Insulation, IEEE Transactions on, 16*(1), 1-10.

IEC-60060-1. (2010). High-Voltage Test Techniques Part 1: General Definitions and Test Requirements.

IEC-61400-24. (2002). Wind turbine generator systems–Part 24: Lightning protection.

IEC-62305-1. (2010). Protection against lightning – Part 1: General principles.

Inoue, K., Korematsu, Y., Nakamura, N., Matsushita, T., Murata, N., Kuroiwa, T., . . . Suguro, Y. (2004). *Study on Damage-Mechanism of Wind Turbine Blades by Lightning Strike.* Paper presented at the International Conference on Lightning Protection, Avignon, France.

Kawakami, H. (2011). *Lightning Strike Induced Damage Mechanisms of Carbon Fiber Composites*. PhD thesis, University of Washington.

Lago, F., Gonzalez, J. J., Freton, P., & Gleizes, A. (2004). A numerical modelling of an electric arc and its interaction with the anode: Part I. The two-dimensional model. *Journal of Physics D: Applied Physics, 37*(6), 883.

Lago, F., Gonzalez, J. J., Freton, P., Uhlig, F., Lucius, N., & Piau, G. P. (2006). A numerical modelling of an electric arc and its interaction with the anode: part III. Application to the interaction of a lightning strike and an aircraft in flight. *Journal of Physics D: Applied Physics, 39*(10), 2294.

Landel, R. F., & Nielsen, L. E. (1993). Mechanical properties of polymers and composites.

Larigaldie S, Labaune G, Moreau, JP. (1981). Lightning leader laboratory simulation by means of rectilinear surface discharges. *Journal of Applied Physics, 52*(12), 7114-7120.

Larigaldie S. (1987). Spark propagation mechanisms in ambient air at the surface of a charged dielectric. I. Experimental: The main stages of the discharge. *Journal of Applied Physics, 61*(1), 90-101.

Larigaldie S, Roussaud A, Jecko B. (1992). Mechanisms of high-current pulses in lightning and long-spark stepped leaders. *Journal of Applied Physics, 72*(5), 1729-1739.

Lee, D. (2008). *Feasibility study on laser microwelding and laser shock peening using femtosecond laser pulses.* PhD thesis, University of Michigan.

Lewke, B., Hernández, Y. M., & Kindersberger, J. (2007, 9 May). *A Simulation Method for the Wind Turbine's Electric Field Distribution Caused by the Stepped Lightning Leader.* Paper presented at the European Wind Energy Conference.

Li, Y., Li, R., Lu, L., & Huang, X. (2015). Experimental study of damage characteristics of carbon woven fabric/epoxy laminates subjected to lightning strike. *Composites Part A: Applied Science and Manufacturing, 79*, 164-175.

Lowke, J. J., & Tanaka, M. (2006). 'LTE-diffusion approximation'for arc calculations. *Journal of Physics D: Applied Physics, 39*(16), 3634.

Lua, J., O'Brien, J., Key, C. T., Wu, Y., & Lattimer, B. Y. (2006). A temperature and mass dependent thermal model for fire response prediction of marine composites. *Composites Part A: Applied Science and Manufacturing, 37*(7), 1024-1039.

Madsen, S. F., Holbøll, J., Henriksen, M., & Sørensen, T. (2006). *Interaction between electrical discharges and materials for wind turbine blades-particularly related to lightning protection.* PhD thesis, Technical University of Denmark.

Mall, S., Ouper, B. L., & Fielding, J. C. (2009). Compression strength degradation of nanocomposites after lightning strike. *Journal of composite materials*.

McCoy, T., Rhoads, H., Lisman, T., McNiff, B., & Smith, B. (2000). *Lightning Activities in the DOE-EPRI Turbine Verification Program*: National Renewable Energy Laboratory.

MIL-464-A. (1997). Electromagnetic Environmental Effects Requirements for systems: US Department of Defense.

Morgan, B., Madhukar, M., Walsh, J., Hooker, M., & Grandlienard, S. (2009). Moisture degradation of cyanate ester/S2 glass composite insulation systems. *Journal of composite materials*.

Muñoz, R., Delgado, S., González, C., López-Romano, B., Wang, D.-Y., & Llorca, J. (2014). Modeling Lightning Impact Thermo-Mechanical Damage on Composite Materials. *Applied Composite Materials, 21*(1), 149-164.

Naghipour, P., Pineda, E. J., & Arnold, S. M. (2016). Simulation of Lightning-Induced Delamination in Unprotected CFRP Laminates. *Applied Composite Materials,* 1-13.

Nestor, O. H. (1962). Heat intensity and current density distributions at the anode of high current, inert gas arcs. *Journal of applied physics, 33*(5), 1638-1648.

Ogasawara, T., Hirano, Y., & Yoshimura, A. (2010). Coupled thermal–electrical analysis for carbon fiber/epoxy composites exposed to simulated lightning current. *Composites Part A: Applied Science and Manufacturing, 41*(8), 973-981.

Paxton, A. H., Baker, L., & Gardner, R. L. (1987). Reply to comments of Hill. *Physics of Fluids (1958-1988), 30*(8), 2586-2587.

Paxton, A. H., Gardner, R. L., & Baker, L. (1986). Lightning return stroke. A numerical calculation of the optical radiation. *Physics of Fluids (1958-1988), 29*(8), 2736-2741.

Perera, C., Rahman, M., Fernando, M., Liyanage, P., & Cooray, V. (2012). The relationship between current and channel diameter of 30 cm long laboratory sparks. *Journal of electrostatics, 70*(6), 512-516.

Plooster, M. N. (1971a). Numerical model of the return stroke of the lightning discharge. *Physics of Fluids (1958-1988), 14*(10), 2124-2133.

Plooster, M. N. (1971b). Numerical simulation of spark discharges in air. *Physics of Fluids (1958-1988), 14*(10), 2111-2123.

"Product Data. HexPly® 8552 Epoxy matrix (180°C/356°F curing matrix)," URL: http://www.hexcel.com/Resources/DataSheets/Prepreg-Data-Sheets/8552_us.pdf

"Product Data. HexTow AS4," URL: http://www.hexcel.com/resources/datasheets/carbon-fiber-data-sheets/as4.pdf

Rakov, V. A., & Uman, M. A. (1998). Review and evaluation of lightning return stroke models including some aspects of their application. *Electromagnetic Compatibility, IEEE Transactions on, 40*(4), 403-426.

Rakov, V. A., & Uman, M. A. (2003). *Lightning: physics and effects*: Cambridge University Press.

Rupke, E. (2002). *Lightning direct effects handbook.* Lightning Technologies Inc. Report No. AGATE-WP3, 1-031027.

SAE-ARP-5412A. (2005). Aircraft lightning environment and related test waveforms: February.

Salah, L., Kuruppuarachchige, C., and Salagame, R. (2013). NASA LSP Composite Substrate Destructive Evaluation Test, Report, National Institute for Aviation Research, Wichita State University, June 2013.

Sauder, C., Lamon, J., and Pailler, R. (2002). Thermomechanical Properties of Carbon Fibres at High Temperatures (Up to 2000 °C), *Composites Science and Technology, 62(*4), 499-504.

Solacity Inc. (n.d.). *Lightning protection*. Retrieved from http://www.solacity.com/lightning.htm.

Tanaka, M., Terasaki, H., & Ushio, M. (2002). Effect of Anode Heat Transfer on Melted Penetration in Welding Process by Free-burning Argon Arc. *ISIJ international, 42*(9), 1005-1009.

Tanaka, M., Terasaki, H., Ushio, M., & Lowke, J. J. (2003). Numerical study of a free-burning argon arc with anode melting. *Plasma Chemistry and Plasma Processing, 23*(3), 585-606.

Tanaka, M., Yamamoto, K., Tashiro, S., Nakata, K., Yamamoto, E., Yamazaki, K., . . . Lowke, J. J. (2010). Time-dependent calculations of molten pool formation and thermal plasma with metal vapour in gas tungsten arc welding. *Journal of Physics D: Applied Physics, 43*(43), 434009.

Takahashi, K., & Hahn, H. T. (2011). Investigation of temperature dependency of electrical resistance changes for structural management of graphite/polymer composite. *Journal of Composite Materials*, 0021998311416683.

Tipler, P. A., & Mosca, G. (2007). *Physics for scientists and engineers*: Macmillan.

Tsai, N. S., & Eagar, T. W. (1985). Distribution of the heat and current fluxes in gas tungsten arcs. *Metallurgical Transactions B, 16*(4), 841-846.

Uman, M. A. (2001). *The lightning discharge*: Courier Corporation.

US Department of Energy. (n.d.). WINDExchange. Retrieved from http://apps2.eere.energy.gov/wind/windexchange/wind_installed_capacity.asp.

Wallenberger, F., & Bingham, P. (2010). *Fiberglass and Glass Technology: energy-friendly compositions and applications*: New York, NY: Springer Science.

Wang, F. S., Ding, N., Liu, Z. Q., Ji, Y. Y., & Yue, Z. F. (2014). Ablation damage characteristic and residual strength prediction of carbon fiber/epoxy composite suffered from lightning strike. *Composite Structures, 117*, 222-233.

Wang, Y., & Zhupanska, O. I. (2015). Lightning strike thermal damage model for glass fiber reinforced polymer matrix composites and its application to wind turbine blades. *Composite Structures, 132*, 1182-1191.

Yin, T., Zhang, Z., Li, X., Feng, X., Feng, Z., Wang, Y., . . . Gong, X. (2014). Modeling ablative behavior and thermal response of carbon/carbon composites. *Computational Materials Science, 95*, 35-40.

Zhou H, Diendorfer G, Thottappillil R, Pichler H, Mair M. (2012). Characteristics of upward positive lightning flashes initiated from the Gaisberg Tower. *Journal of Geophysical Research: Atmospheres*, 117: D6.